



저작자표시-비영리-변경금지 2.0 대한민국

이용자는 아래의 조건을 따르는 경우에 한하여 자유롭게

- 이 저작물을 복제, 배포, 전송, 전시, 공연 및 방송할 수 있습니다.

다음과 같은 조건을 따라야 합니다:



저작자표시. 귀하는 원저작자를 표시하여야 합니다.



비영리. 귀하는 이 저작물을 영리 목적으로 이용할 수 없습니다.



변경금지. 귀하는 이 저작물을 개작, 변형 또는 가공할 수 없습니다.

- 귀하는, 이 저작물의 재이용이나 배포의 경우, 이 저작물에 적용된 이용허락조건을 명확하게 나타내어야 합니다.
- 저작권자로부터 별도의 허가를 받으면 이러한 조건들은 적용되지 않습니다.

저작권법에 따른 이용자의 권리는 위의 내용에 의하여 영향을 받지 않습니다.

이것은 [이용허락규약\(Legal Code\)](#)을 이해하기 쉽게 요약한 것입니다.

[Disclaimer](#)

Ph. D. DISSERTATION

**OLED PIXEL STRUCTURE
FABRICATED WITH SIMPLIFIED
PATTERNING AND IMPROVED OUT-
COUPLING**

단순화된 패터닝을 통한 유기발광다이오드 픽셀 구조와
광추출 향상에 대한 연구

BY

Jongseok Han

August 2018

DEPARTMENT OF
ELECTRICAL AND COMPUTER ENGINEERING
COLLEGE OF ENGINEERING
SEOUL NATIONAL UNIVERSITY

OLED PIXEL STRUCTURE FABRICATED WITH
SIMPLIFIED PATTERNING AND IMPROVED OUT-
COUPLING

단순화된 패터닝을 통한 유기발광다이오드 픽셀
구조와 광추출 향상에 대한 연구

지도교수 이 창 희

이 논문을 공학박사 학위논문으로 제출함

2018 년 8 월

서울대학교 대학원

전기컴퓨터공학부

한 중 석

한중석의 공학박사 학위논문을 인준함

2018 년 8 월

위 원 장 : _____ (인)
부위원장 : _____ (인)
위 원 : _____ (인)
위 원 : _____ (인)
위 원 : _____ (인)

Abstract

OLED PIXEL STRUCTURE FABRICATED WITH SIMPLIFIED PATTERNING AND IMPROVED OUT-COUPLING

Jongseok Han

DEPARTMENT OF ELECTRICAL AND
COMPUTER ENGINEERING
COLLEGE OF ENGINEERING
SEOUL NATIONAL UNIVERSITY

There have been great interests and advances in organic light emitting diodes (OLEDs) for few decades, enabling OLEDs to serve as commercial available solid-state lighting sources and flat-panel display. In the display industry, low-cost OLED fabrication and high performance are prerequisite for expansion of OLED market. For that purpose, various OLED pixel architectures and techniques enhancing OLED out-coupling are introduced for cost reduction and improved performance. For example, pentile pixel structure and white OLED with color filters are demonstrated or external macro-extractor, micro-lens array, surface scattering layers, low-index grid, high-

index substrates, and internal extraction layers are shown to simplify manufacture process or increase efficiency. However, the price of OLED panel and low performance of OLED is still hurdles to expand OLED display market.

In this thesis, introductions of new OLED design in terms of pixel design and device design for reducing full-color OLED manufacturing cost and improving device performance are mainly studied. By using a yellow common layer (YCL), we implement full-color OLED through single EML patterning, and by inserting thermally-assisted, self-aggregated silver nanoparticles (TSA-Ag NPs), we enhance out-coupling efficiency of the device. These introductions of new OLED design to expand OLED display market needs to be investigated.

First of all, to achieve single FMM step, we report a simple and effective pixel structure for full-color OLED displays using a YCL. Simple fabrication of OLEDs by a low-cost process is an ongoing issue because conventional fine metal mask (FMM) steps are complicated and time-consuming processes. Recently, yellow and blue OLEDs (Y/B OLEDs) with color filters (CFs), which can reduce one FMM step, have been introduced, and they can achieve long lifetimes and high resolutions. By depositing the yellow layer with an open mask as a common layer, we can eliminate the yellow patterning step. Because the dopant in the YCL acts as a hole trap path, controlling the trap depth or density in the YCL is essential. By selecting different hole transport layer (HTL) host materials, we investigate which HTL is most appropriate for the YCL and determine the effect of the YCL compared to the conventional Y/B OLEDs. With the advantages of Y/B OLEDs such as long lifetimes and high resolutions, OLEDs employing the YCL can finally achieve low-cost OLED fabrication.

Next, we demonstrate a production-ready alternative to enhance the out-coupling efficiency of OLEDs by implementing thermal-assisted self-aggregated

metallic nanoparticles (NPs). Metallic nano-structures in micro-cavity organic light emitting diode (OLED) can significantly enhance light out-coupling efficiency. Nevertheless, they are not widely accepted in conventional devices due to its complicated process and increased manufacturing cost. In this chapter, silver NPs are fabricated by thermal annealing of vacuum deposited thin silver layer without any complicated process, which is easily scalable in large area without cost increase. Theoretical simulation and dark field microscopy image show that these stochastic Ag NPs provide plasmonic effect in broad range. By incorporating Ag NPs to OLED with micro-cavity structure, 11% improvement in the external quantum efficiency was obtained without deteriorating viewing angle.

In conclusion, this thesis proposes the innovative and useful approaches to accomplish full-color OLED display with simple and low-cost process and improve the device performance. In the current display manufacture, these techniques can be production-ready alternatives because fabrication process is compatible with current OLED fabrication process such as thermal evaporation and annealing process. We believe that these investigations on adoption of the common layer and insertion of thermal Ag NPs will offer a beneficial platform for further research toward low-cost and highly efficient OLED display fabrication in the display industry.

Keywords: Organic Light-Emitting Diodes, Yellow Common Layer, EML Patterning, Thermally-Assisted, Self-Aggregated Silver Nano Particles, Out-Coupling Efficiency

Student Number: 2013-20905

Contents

Abstract	i
Contents	v
List of Figures	ix
List of Tables	xv
Chapter 1	1
1.1 Organic Light-Emitting Diodes	1
1.2 Remained Issues for OLEDs.....	6
1.3 OLED Patterning with Simplified Pixel	8

1.4	Enhancement of OLED Out-Coupling.....	11
1.5	Outline of Thesis	15
Chapter 2		17
2.1	Materials.....	17
2.1.1	Preparation of Organic Materials	17
2.1.2	Chemical Structures of Organic Materials	17
2.2	Device Fabrication and Characterization Methods	21
2.2.1	Device Fabrication Methods.....	21
2.2.2	Current-Voltage-Luminance Measurement	23
2.2.3	Efficiency Calculation Methods	27
2.2.4	Angular Dependent Electroluminescence Measurement.....	28
2.2.5	Other Characterization Methods	29
2.3	Theory.....	31
2.3.1	Space-Charge-Limited Measurement	31
2.3.2	Plasmonic Effect	32
Chapter 3		35
3.1	Device Configuration of Yellow/Blue OLED with A Yellow Common Layer.....	37

3.2	Characteristics of A Yellow Common Layer and An Electron Blocking Layer.....	40
3.2.1	Negligible Optical Effect of Yellow Doped Common Layer...	40
3.2.2	Insertion of Electron Blocking Layer for Suppressing Energy Transfer Between Blue and Yellow Emission Layer	42
3.3	Characteristics of Device Performance of Yellow/Blue OLED with A Yellow Common Layer.....	45
3.4	Dopant Trap Effect Caused by Hole Trap Depth.....	51
3.5	Dopant Trap Effect Caused by Hole Trap Density	56
3.6	Improvement of Color Gamut Using A Red and Green Common Layer	60
3.7	Stability of The Blue Devices with The YCL	62
3.8	Summary	65
Chapter 4		67
4.1	Fabrication of OLED of D/M/D Transparent Electrode with TSA-Ag NPs.....	70
4.2	Generation and Surface Morphology TSA-Ag NPs	72
4.3	Optical Properties of TSA-Ag NPs.....	76

4.4	Optical Simulation of OLED with TSA-Ag NPs.....	80
4.5	Device Performance of OLEDs with TSA-Ag NPs.....	85
4.6	Mitigation of Wavelength Dependence of OLED with D/M/D Structure by Using TSA-Ag NPs	91
4.7	Uniformity of OLED with D/M/D Structure by Using TSA-Ag NPs	94
4.8	Summary	96
	Chapter 5	97
	Bibliography	101
	Publication	109
	한글 초록	113

List of Figures

Figure 1.1 Various application products of OLEDs. Samsung mobile display and Apple mobile display, LG TV display, Samsung foldable display (concept model), LG Display rollable display (clockwise).	2
Figure 1.2 The history of OLED pixel structures.	8
Figure 1.3 AMOLED pixel structures (RGB side-by-side and white OLED with CFs).	10
Figure 1.4 Pixel and device design for improving OLED performance.....	14
Figure 2.1 Chemical structures of di-[4-(N,N-ditolyl-amino)-phenyl]cyclohexane (TAPC), 4,4',4''-tris(carbazol-9-yl)triphenylamine (TCTA), 4,4'-Bis(N-carbazolyl)-1,1'-biphenyl (CBP) and 1,3-bis(carbazol-9-yl)benzene (mCP) as hole transporting materials and host materials. ...	18

Figure 2.2 Chemical structures of 1,3,5-tri[(3-pyridyl)-phen-3-yl]benzene (TmPyPB) and 2,2',2''-(1,3,5-Benzinetriyl)-tris(1-phenyl-1-H-benzimidazole) (TPBi) as electron transporting materials and host materials.	19
Figure 2.3 Chemical structures of iridium(III) bis(4-(4-t-butylphenyl)thieno[3,2-c]pyridinato-N,C20)acetylacetonate (Ir(tppy) ₂ (acac)) as yellow emitter [30], Bis[2-(4,6-difluorophenyl)pyridinato-C2,N](picolinate)iridium(III) (Firpic) as blue emitter, Tris[2-phenylpyridinato-C2,N]iridium(III) (Ir(ppy) ₃) as green emitter, and 4,4'-bis(9-ethyl-3-carbazovinylene)-1,10-biphenyl (BCzVBi) as blue emitter.	20
Figure 2.4 Schematic diagrams for the measurement of (a) I-V-L characteristics and (b) EL spectra.	24
Figure 2.5 (a) The CIE standard observer color-matching functions and (b) the CIE 1931 color space chromaticity diagram. The outer boundary is the spectral locus, with wavelengths shown in nanometers.	26
Figure 2.6 A schematic diagram of the angular dependent EL measurement set up.	28
Figure 2.7 Electric field patterns of Rayleigh and Mie scattering.	33
Figure 2.8 Schematic of the plasmon effect of NPs.	34
Figure 3.1 (a) Schematic diagrams of full-color OLEDs with a YCL structure, (b) pixelation of red, green, yellow, and blue sub-pixels, (c) the energy level diagram of the blue device using the YCL with different HTLs.	37
Figure 3.2 Absorption spectra of films with pristine and of Ir(tppy) ₂ (acac)-doped (a) TAPC, (b) TCTA and (c) CBP.	41
Figure 3.3 (a) Device structure of blue sub-pixel with EBL and without EBL and (b) schematic energy diagram of insertion of EBL between the YCL and blue EML.	43

Figure 3.4 (a), (b), (c) Normalized EL intensity of blue with EBL and without EBL of TAPC, TCTA, and CBP and (d), (e), (f) E.Q.E–current density characteristics of blue with EBL and without EBL of TAPC, TCTA, and CBP.....	44
Figure 3.5 Current density–voltage and luminance–voltage characteristics for the (a), (b) B1, B2 and (c), (d) Y1 devices with different HTL materials.....	46
Figure 3.6 EL spectra and external quantum efficiency (EQE) of the devices (a), (b) B1, B2 and (c), (d) Y1 with different HTL materials.....	48
Figure 3.7 Schematic energy levels of Ir(tptpy) ₂ (acac)-doped TAPC, TCTA and CBP with the hole trap depth (ΔE_{HOMO}) calculated from the difference of the HOMO energy levels between the host and dopant materials, (b) driving voltage changes with and without the YCL with increasing ΔE_{HOMO} ..	51
Figure 3.8 Current density–voltage characteristics of hole-only devices of different HTLs with and without Ir(tptpy) ₂ (acac) measured at various temperatures.....	53
Figure 3.9 Temperature dependence of m from Equation (1) and its linear fitting curve of the hole-only devices of different HTL materials with and without the yellow dopant in order to extract trap energy.....	55
Figure 3.10 Current density–voltage characteristics of hole-only devices with pristine and different doping concentration of Ir(tptpy) ₂ (acac)-doped (a) TAPC, (b) TCTA and (c) CBP.....	57
Figure 3.11 (a) Impedance versus voltage and (b) phase versus voltage characteristics of the hole-only devices with pristine and different doping concentrations of Ir(tptpy) ₂ (acac)-doped (a), (b) TAPC, (c), (d) TCTA and (e), (f) CBP.....	59
Figure 3.12 The device structures of the blue OLED with RG-CL.....	61

Figure 3.13 EL spectra and of the yellow device with (a) the YCL and (c) RG-CL, and (b), (d) their CIE color coordinates.....	61
Figure 3.14 Luminance-time characteristics of the blue sub-pixel with YCL and without YCL of (a) TAPC, (b) TCTA and (c) CBP.	63
Figure 3.15 (a) Luminance-time and (b) voltage—time characteristics of the blue sub-pixel with EBL and without EBL of TCTA.....	64
Figure 4.1 Process schematic diagram for OLED with TSA-Ag NPs. Here, the NPs were generated by thermal annealing of vacuum deposited silver layer (1 nm) without using any solution or complicated photo lithography process. In the device, the TSA-Ag NPs were located under transparent D/M/D electrode.....	71
Figure 4.2 SEM images of Ag layer (1 nm) depending on the annealing process temperature: (a) as-deposited, (b) annealed 250 °C and (c) annealed 450 °C. As substrate was heated, Ag aggregated each other and eventually changed its phase to large sized clusters (50-100 nm) (d) Transmittance spectra of glass/silver layers/low index polymer before and after annealing.	73
Figure 4.3 Size distribution of TSA-Ag NPs (74 ± 19 nm) derived from the SEM image. The size distribution was determined by software (Image J) in $5 \times 5 \mu\text{m}^2$ area.	74
Figure 4.4 Atomic force microscopy (AFM) image of Ag layer on cleaned glass. ...	75
Figure 4.5 (a) Dark field microscopy image of TSA-Ag NPs incorporated LIP on the SiO ₂ /Si wafer. The variety of color in dark field microscopy image represented that stochastic TSA-Ag NPs provided plasmonic effect in broad range of visible light. (b) That of low index polymer (LIP) (200 nm)	

deposited on SiO₂ (100nm)/Si wafer. (c) Calculated plasmonic effect intensity of different sized Ag NPs (50-120 nm) in LIP based on FDTD simulation. 78

Figure 4.6 Calculated E-field distribution at the OLED employing D/M/D electrode (a) with and (b) without TSA-Ag NPs under 500 and 550 nm light, respectively. The plasmonic effect induced by NPs themselves as well as the interaction between thin Ag in D/M/D and TSA-Ag NPs were exhibited. In contrast, no light enhancement was observed in the case of without them. These figures clearly points out that the installment of TSA-Ag NPs to device enables to scatter light at the device structure. 82

Figure 4.7 The empirical and simulated enhancement ratio of out-coupled light intensity of OLED with NPs, compared to the case without them. Here, the empirical and theoretical enhancement ratio was derived by dividing the result of OLED with TSA-Ag NPs by one without them at each wavelength. 84

Figure 4.8 Performance of OLEDs employing D/M/D electrode with and without TSA-Ag NPs:(a) Current density-voltage-luminance (J-V-L), (b) External quantum efficiency (EQE)-luminance considering angular dependence and (c) luminance-current efficiency characteristics. For the comparison, optoelectronic properties of device with ITO electrode were also included each graph. The graphs directly show that the implementation of TSA-Ag NPs to micro-cavity based OLED leads to additional improvement in the efficiency of device. (d) EL spectra of the OLEDs, reflecting that TSA-Ag NPs provide the enhancement in out-coupling efficiency in broad range. 86

Figure 4.9 The angular dependence of EL intensity of OLEDs with various structures at 5 mA/cm². Differ from results of periodic nano structure, the EL intensity of OLED with TSA-Ag NPs is broadly enhanced compared to the case without them. The EQE of device, shown in Fig 4(b), was calculated considering the angular dependence of device..... 88

Figure 4.10 (a) Current efficiency (C.E)-luminance and (b) external quantum efficiency (EQE)-luminance characteristics, (c) the transmittance, and (d) EL intensity of OLEDs employing D/M/D electrode with TSA-Ag NPs. 90

Figure 4.11 EL spectra of micro cavity OLED (a) without and (b) with TSA-Ag NPs and their corresponding CIE 1931 color space chromaticity diagram at different angles. Here, the $\Delta_{x,y}$ is the change of color coordination of emissive light at normal and 80° degree. 92

Figure 4.12 (a) J-V characteristics of OLED with (Red line) and without (Blue line) TSA-Ag NPs. (b), (c) Driving voltage of each device at 5mA/cm²..... 95

List of Tables

Table 1.1 The status of emitting materials for OLEDs.....	5
Table 1.2 Comparison of the device performance of the previously reported out-coupling technologies.	13
Table 3.1 Device structures of blue and yellow OLEDs.	38
Table 3.2 Performances of devices with different YCLs.....	50
Table 4.1 Device performance of OLEDs with D/M/D including TSA-Ag NPs.....	87

Chapter 1

Introduction

1.1 Organic Light-Emitting Diodes

Organic light-emitting diodes (OLEDs) have attracted great interests for few decades, enabling OLEDs to serve as commercial available solid-state lighting sources and flat-panel display. The OLEDs have a lot of advantages such as thin, light, vivid color, and availability for flexible, stretchable, and foldable device, and potential for low-cost process.

Recently, full-color OLEDs display have commercialized on mobile and TV applications. Samsung mass-produced high resolution flexible OLED mobile display for their premium smartphone galaxy S9 series and Apple adopted flexible OLED display for brand new Iphone X model instead of LCD display. LG display produced flagship smart TVs using white OLEDs combined with color filters. In addition, rollable and foldable displays are coming into existence very soon. LG display exhibited prototype of rollable OLED TV at CES 2018. Samsung launched concept

video of fully flexible and foldable OLED display, which will be able to expand to tablet size and shrink to the size of a mobile phone. Figure 1.1 shows the representative OLED based products.

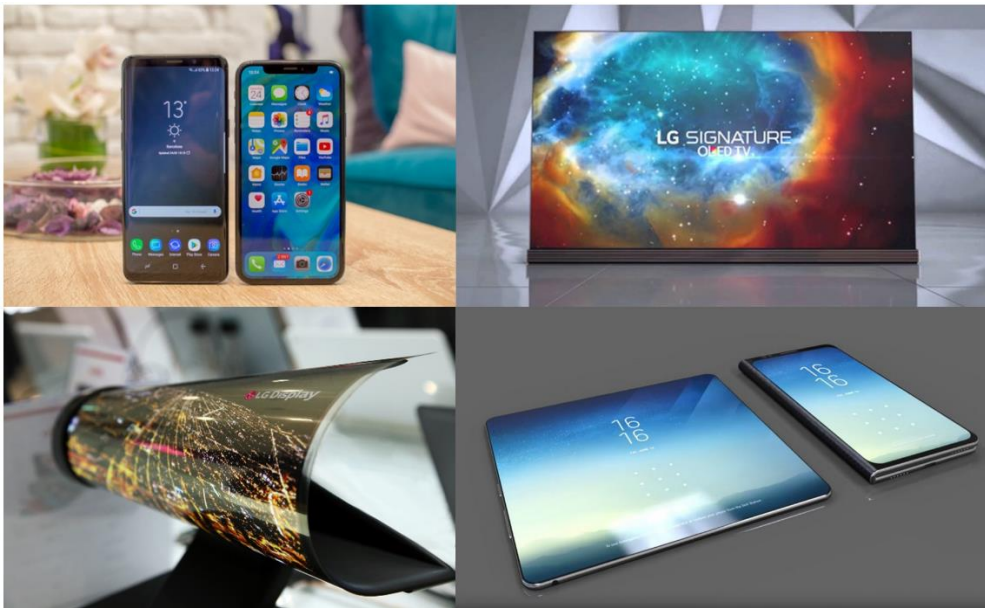


Figure 1.1 Various application products of OLEDs. Samsung mobile display and Apple mobile display, LG TV display, Samsung foldable display (concept model), LG Display rollable display (clockwise).

The first report of electroluminescence (EL) in organic materials was examined by Pope, Kallmann, and Magnate in 1963 [1]. However, they are difficult to use them as a practical product because they used 10 μm to 20 μm thick single crystal anthracene and could observe emitted light from anthracene above about 400 V. Vityuk and Mikho established that vapor-deposited thin films of anthracene also exhibit EL [2]. Subsequently, Vincett *et al.* reported clearly visible EL from an organic material at voltages which are significantly less than 100 V using vacuum-deposited

anthracene, still external quantum efficiency (EQE) of the device is about 0.03% ~ 0.06% [3]. Partridge reported first EL generation using organic polymer films [4].

In 1987, Tang and VanSlyke invented practically available and highly improved OLEDs, which have a double-layer structure of organic thin films, prepared by vacuum deposition [5]. The aromatic diamine as a hole transporting layer (HTL) and 8-hydroxyquinoline aluminum (Alq_3) as an emitting and electron transporting layer (ETL) were used. Total thickness of the device was approximately 135 nm, which is much thinner than previous reported organic EL devices. The device emitted green color with relatively high EQE (1%) and high brightness ($> 1000 \text{ cd/m}^2$) at a driving voltage below 10 V. After that, Tang *et al.* increases the efficiency of OLEDs twice times than the undoped device by introducing molecular doping system in 1989 [6]. Moreover, the EL colors can be readily tuned by not only a suitable choice of dopants but also by changing the concentration of the dopant. Aforementioned researches were achieved by using small molecular weight organic materials and the vacuum thermal evaporation technique. Meanwhile, in 1990, Burroughes *et al.* reported the first conjugated polymer light-emitting diodes (PLEDs) by spin-coating poly(p-phenylene vinylene) (PPV) on the indium-tin-oxide (ITO) coated glass substrate and the maximum quantum efficiency of the device is about 0.05% [7]. These solution processible characteristics of PLEDs exhibited a potential of low-cost fabrication for large-size device compared with vacuum thermal evaporation. Kido *et al.* demonstrated first white OLEDs by using polymer doped with blue, green, and orange fluorescent dyes [8]. Though the efficiency of the device is low, this result suggests that OLEDs can be utilized for solid-state lightings. After that, there are many developments such as synthesizing efficient materials and introducing novel device structures to improve the efficiency of OLEDs. However, the efficiency of the device was still low because they used only fluorescence. When the electrically injected

electrons and holes are recombined, the singlet and triplet excited states are generated with the ratio of 1:3, statistically. Fluorescence utilizes only singlet excitons so the internal quantum efficiency (IQE) of OLEDs with the fluorescent emitter is theoretically limited to 25%.

M. A. Baldo *et al.* dramatically improved the efficiency of OLEDs by the introduction of the phosphorescent dye 2,3,7,8,12,13,17,18-octaethyl-21H,23H-porphine platinum(II) (PtOEP) [9]. By using phosphorescent material, the IQE of OLEDs can be theoretically 100% because phosphorescence utilizes triplet excitons and singlet excitations. In addition, the performance of OLEDs is intensely improved by adopting tandem structure using charge generation unit and p-i-n structure using electrical doping. [10, 11]. Today, the performances of OLEDs are surprisingly enhanced and organic materials with high efficiency and stability are being developed from several companies. The recent status of commercially available OLED emitter materials is summarized in Table 1.1.

Table 1.1 The status of emitting materials for OLEDs.

	Color	CIE (x, y)	Efficiency (cd/A)	LT50 (hrs)	Company	Ref.
Fluorescence	Red	(0.67, 0.33)	11	160000	Idemitsu Kosan (CIE, Efficiency: at 10mA/cm ² , LT50: at 1000 cd/m ²)	[12]
	Green	(0.29, 0.64)	37	200000		
	Blue	(0.14, 0.12)	9.9	11000		
Phosphorescence	Deep Red	(0.69, 0.31)	17	250000	Universal Display Corporation (at 1000 cd/m ²)	[13]
	Red	(0.64, 0.36)	30	900000		
	Yellow	(0.44, 0.54)	81	1450000		
	Green	(0.31, 0.63)	85	400000		
	Light Blue	(0.18, 0.42)	50	20000		

1.2 Remained Issues for OLEDs

Though the performance of OLEDs is improved, there are still many problems to resolve. First, to expand OLEDs market and compete with LCDs, mass production of OLEDs panels and reduction of fabrication cost are absolutely required. However, current OLED fabrication method is too complicated, which is the thermal evaporation with the fine metal mask (FMM) process. The FMM is utilized to form red (R), green (G), and blue (B) colors of RGB sub-pixels. When the each color is patterned, different FMM process is needed, which means 3 FMM process are used for patterning RGB colors. This FMM technique for RGB EML patterning leads to increased TAKT time and color mixing due to mask sagging and misalignment of FMM when applied to large-size OLEDs displays [14-16]. A number of companies and groups are trying to resolve these problems for commercialized OLEDs panels.

Second, with the development of the display size and quality, high resolution is also an important issue in the display industry. As aforementioned, current thermal evaporation fabrication with FMM patterning has hurdles to achieve high resolution due to mask sagging and difficulty of alignment. To resolve this problems, some companies suggest pentile pixel structure or small mask scanning (SMS) method [17, 18]. However, customers still need higher resolution than current FHD, QHD resolution.

Third, lifetime is an on-going issue to use the OLEDs in the display panel for many years. Over the recent years, there has been a huge increase in device lifetime and researchers have analyzed OLED degradation mechanism, which is related with charge accumulation, electro-, photochemical reactions, insufficient encapsulation, interfacial effect and so on [19, 20]. However, the OLED panel shows short lifetime

with burn-in phenomenon and exact and complex reason of OLED degradation is still unknown.

Fourth, although the efficiency has been improved a lot, it is still necessary to increase the efficiency. Despite the internal quantum efficiency (IQE) of 100% of recent phosphorescent materials but EQE is generally limited to 20% due to an optical loss by total internal reflection, waveguide mode and surface plasmon. To reduce these optical losses, we need to improve out-coupling efficiency because EQE is a product of the IQE and the out-coupling efficiency. To enhance out-coupling efficiency, many researchers have studied by using various methods such as external macro-extractor, micro-lens array, surface scattering layers, low-index grid, high-index substrates, and internal extraction layers [21-25]. However, in spite of a lot of researches, there is not a final decision for technology enhancing out-coupling, which is suitable for large-area display.

1.3 OLED Patterning with Simplified Pixel

The traditional RGB pixel structure for display panel is stripe RGB type, where RGB sub-pixels are placed in regular sequence [14, 16, 26]. This method can achieve good image quality. However, as the display market demands high-resolution panels, this traditional RGB type was unsuitable for them due to the limitation of reducing sub-pixel size by using shadow mask [14, 16, 27]. To increase the resolution, Pentile type pixel structure (RG-BG) was introduced. Pentile structure could accomplish almost same value of pixel per inch (ppi) by using less sub-pixels compared to traditional RGB type, so it could increase the resolution of the mobile display such as Samsung mobile phone. After that, some way of Pentile type was also suggested for other application such as tablet display (e.g. Pentile RGBW). In recent years, Diamond type pixel structure significantly increased the resolution over 500 ppi [17]. Figure 1.2 shows the history of OLED pixel structures.

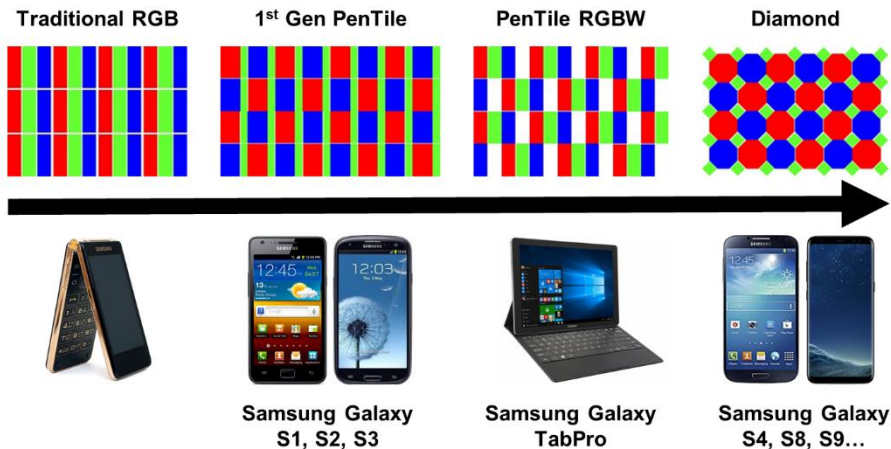


Figure 1.2 The history of OLED pixel structures.

Meanwhile, the high cost of OLED displays caused by complicated manufacturing processes is one of the main hurdles to creating a larger market of OLED TVs and mobile phones. To extend the display market, it is important to reduce the price by simplifying the OLED fabrication process [28, 29]. Conventional full-color OLEDs are produced by the RGB side-by-side method, which uses different fine metal shadow mask (FMM) steps to pattern red, green, and blue (RGB) emission layers (EMLs), respectively [14, 27]. This conventional method has some advantages such as high efficiency, pure color gamut and no color filter (CF) cost, whereas there are also disadvantages such as low yield, high cost, differential aging of each colors. Among them, one of the biggest issues is especially scalability due to mask sagging phenomenon in the large area display [14, 28]. Therefore, this technique is using for small-medium display such as mobile phone. Therefore, some innovative methods exist to reduce the FMM steps and increase the resolution while maintaining a performance comparable to conventional OLEDs, such as white OLEDs (WOLEDs) with color filters (CFs), blue common layer (BCL) and yellow/blue (Y/B) OLEDs with CFs. First, a company suggest new OLED pixel structure using white OLED with RGB CFs [16] . By using a common mask for white tandem OLED, there is no mask changing for EML patterning, so it can produce OLED panels in large size. Despite the simple process using a common mask, the color gamut and power consumption present problems due to the light absorption of the CFs. Another problem is the increased TAKT time, which is defined as the average production time resulting from a thick white tandem structure of WOLEDs. Figure 1.3 shows the conventional RGB side-by-side and white OLED with CFs method.

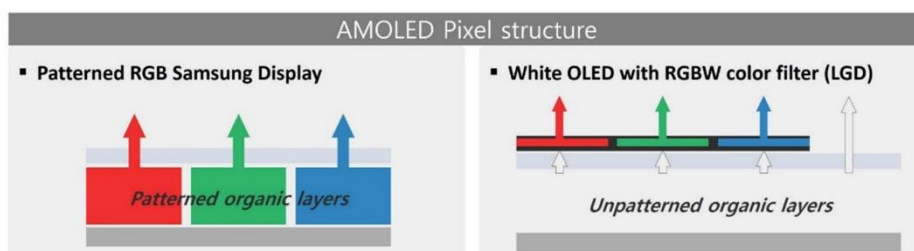


Figure 1.3 AMOLED pixel structures (RGB side-by-side and white OLED with CFs).

Second, a BCL was demonstrated to reduce one patterning step with pixelated red and green colors [14, 27, 29]. Still, the efficiency of blue sub-pixels was quite low because of the thin BCL needed to curb its blue emission in the red and green sub-pixels. Furthermore, the highest occupied molecular orbital (HOMO) and lowest unoccupied molecular orbital (LUMO) energy levels of blue host materials easily increase the driving voltage in the red and green sub-pixels, which results in poor charge injection and transportation [26, 27]. Finally, Universal Display Corporation (UDC) introduced a novel architecture that uses Y/B OLEDs with red and green CFs for full-color OLED displays [30]. Red and green sub-pixels are formed by yellow emission of an OLED after transmitting red and a green CFs, respectively. By controlling the pixel size and sequence, this structure can exhibit an increased lifetime and resolution. Although these remarkable results achieve reducing fabrication cost, it still requires simplified FMM EML patterning steps due to higher cost than LCD display.

1.4 Enhancement of OLED Out-Coupling

One of the approaches to enhance OLED performance is improving light extraction of the device. After the IQE reached almost 100% with the development of the materials and the device structures, studies about improving out-coupling efficiency have been introduced. Due to the total internal reflection induced by the refractive index mismatching between ITO ($n=1.8$) and glass substrate ($n=1.5$), emitted light is entrapped within a specific layer and then the out-coupling efficiency is only about 20% [31]. To increase out-coupling efficiency, a dielectric/metal/dielectric (D/M/D) structure has been widely used to OLEDs employing the micro-cavity effect as shown in Table 1.2 [32]. Moreover, the application of D/M/D electrode mitigates the total internal reflection induced by the refractive mismatching between ITO ($n= 1.8$) and glass substrate. It thus provides the improvement in the EQE of OLED at its resonant wavelength. However, the micro-cavity effect in D/M/D electrode embedded OLED does not contribute to the extraction of all wave guided light [33-35]. Particularly, the total internal reflection between glass ($n=1.5$) and air ($n=1$) is still remained even in a bottom emission structure implementing D/M/D electrode. Another detrimental effect is strong wavelength dependence of out-coupling efficiency in OLEDs incorporating D/M/D structure, which triggers additional mask and steps for fabrication process [33].

Moreover, the incorporation of nano-sized structures to OLEDs has been introduced using scattering effect of them such as gratings, metallic nanoparticles (NPs), buckled structures and so on [34, 36-51]. When the waveguided light reaches them, they changed its penetration direction, resulting in escaping entrapped photons [34, 41]. Moreover, randomly sized and distributed structures without any periodicity allows us to compensate strong wavelength dependence of micro-cavity based devices

[36, 37, 40, 41]. Especially, the size and shape control of silver NPs provides customized light extraction at the emission peak of OLED [52-54]. Despite excellent optical properties of nano structures, their application to OLEDs is still limited due to their complicated process and/or non-uniformity. In the case of widely using photo-lithography, the combination of precise mask and high energy light source with multiple process steps are required, which is bottleneck toward low-cost upscaling. Additionally, the periodicity from the mask pattern during a photo-lithography provokes the strong wavelength and angular dependence of devices. Although solution processed NPs or nano imprinting method fits for demonstrating randomly distributed films with low cost [52-56], its size limitation impedes the incorporation of them to real devices, arising from the inherent disadvantage of wet process. Furthermore, dry process for NPs even needs high power light sources and is difficult to utilize in large-sized substrates owing to limited size of light sources [40, 41]. However, with aforementioned problems for adopting these out-coupling structure, easy and simple method, suitable for large area, are needed to achieve practical application of them to optoelectronic devices with D/M/D electrode, leading to enhanced EQE of OLEDs.

Table 1.2 Comparison of the device performance of the previously reported out-coupling technologies.

	Structure	Max. efficiency	Enhancement ratio
[33]	D/M/D	21.1%	1.52
[57]	D/M/D	8.0 cd/A	1.82
[32]	D/M/D	~63.0%	2.5
[49]	Nanopatterned structure	-	1.5
[51]	Grid structure	19%	1.58
[45]	Nano scattering layer	36.7%	1.66
[50]	Nano size structure	40.0 cd/A	2

In this thesis, introductions of new OLED in terms of pixel design and device design for simplifying the fabrication process and enhancing the device performance are mainly studied. By using a yellow common layer (YCL), we implement full-color OLED through single EML patterning, and by inserting thermally-assisted, self-aggregated silver nanoparticles (TSA-Ag NPs), we enhance out-coupling efficiency of the device.

OLED design for improving the performance of OLEDs

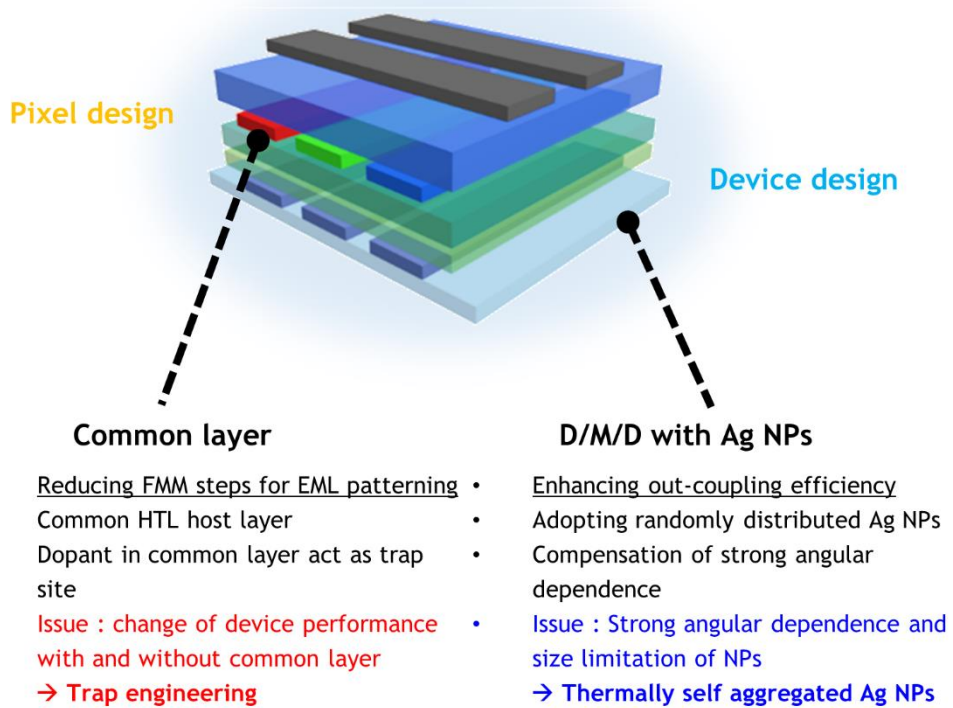


Figure 1.4 Pixel and device design for improving OLED performance.

1.5 Outline of Thesis

This thesis consists of five chapters including **Introduction** and **Conclusion**. As an introduction, **Chapter 1** describes brief history research trend and remained issues of OLEDs. In addition, it also includes the previous research on OLED pixel and OLED techniques of out-coupling enhancement. In **Chapter 2**, the fabrication and characterization methods for the OLED devices are summarized. Moreover, the chemical structures of all used organic materials used in this thesis are demonstrated. In **Chapter 3**, the simple and effective OLED pixel structure for full-color OLED displays is demonstrated. By using a yellow common layer, yellow/blue (Y/B) OLED can be fabricated with a single FMM step for EML patterning. With trap engineering in the common layer such as trap depth or trap density, the design strategy of Y/B OLED using the yellow common layer is introduced. In **Chapter 4**, OLED device structure for the out-coupling efficiency improvement, adopting thermally self-aggregated Ag NPs with D/M/D architecture, is described. We not only enhance out-coupling efficiency but also reduce the dependence of strong wavelength, which is the weakness of D/M/D architecture. We also investigate the plasmonic effect of thermally self-aggregated Ag NPs by employing dark field microscopy and simulation of electrical field distribution. In **Chapter 5**, we summarized our work and some concluding remarks.

Chapter 2

Experimental Methods and Theory

2.1 Materials

2.1.1 Preparation of Organic Materials

The all organic materials used in the thesis are commercially available and purchased and used without further sublimation. The molybdenum trioxide (MoO_3), lithium fluoride (LiF), and aluminum (Al) were purchased from commercial company (CERAC). Most organic materials were purchased from commercial company (Organic Semiconductor Materials).

2.1.2 Chemical Structures of Organic Materials

Below figures are chemical structures of organic materials used in this thesis.

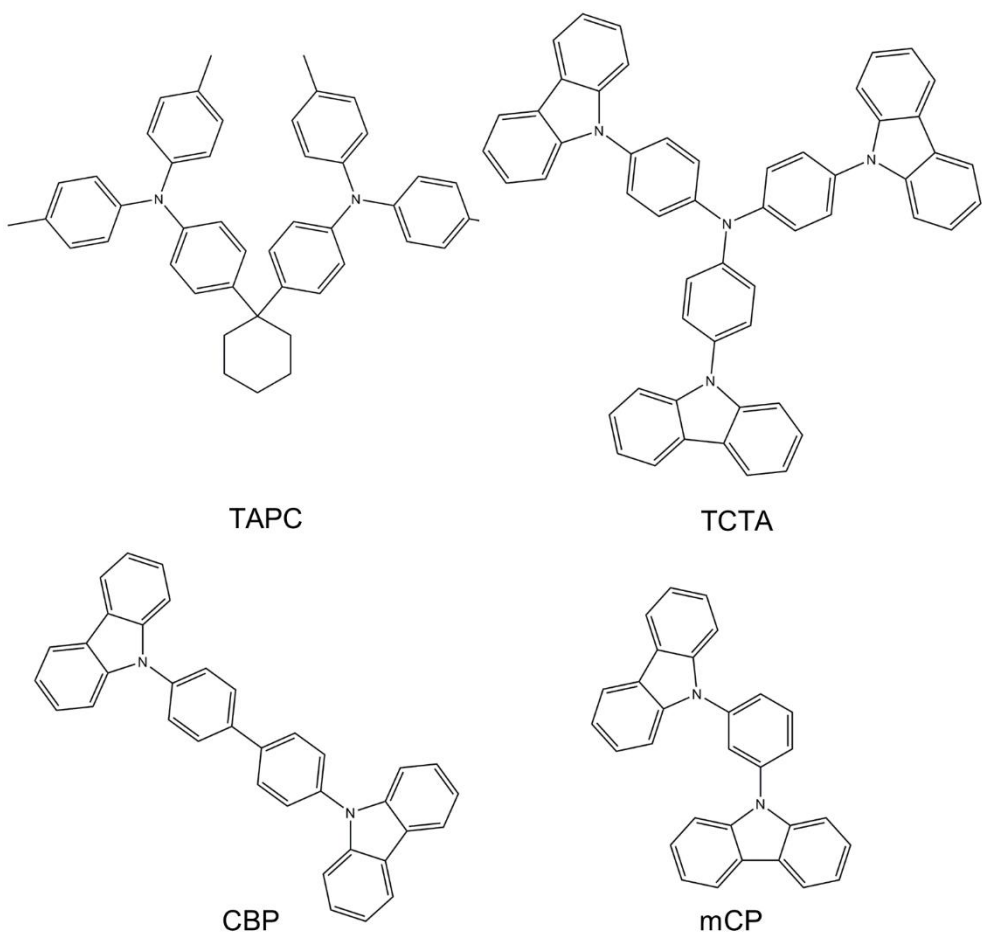


Figure 2.1 Chemical structures of di-[4-(N,N-ditolyl-amino)-phenyl]cyclohexane (TAPC), 4,4',4''-tris(carbazol-9-yl)triphenylamine (TCTA), 4,4'-Bis(N-carbazolyl)-1,1'-biphenyl (CBP) and 1,3-bis(carbazol-9-yl)benzene (mCP) as hole transporting materials and host materials [58-60].

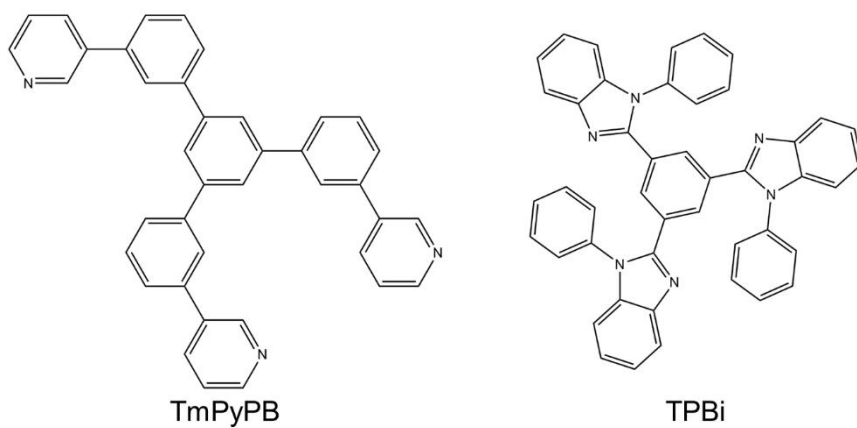
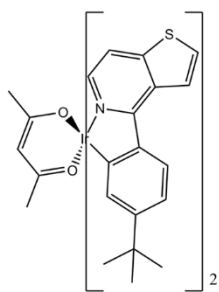
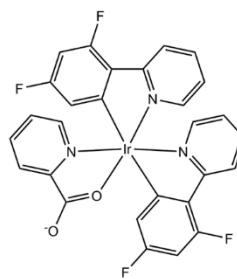


Figure 2.2 Chemical structures of 1,3,5-tri[(3-pyridyl)-phen-3-yl]benzene (TmPyPB) and 2,2',2''-(1,3,5-Benzinetriyl)-tris(1-phenyl-1-H-benzimidazole) (TPBi) as electron transporting materials and host materials [61].



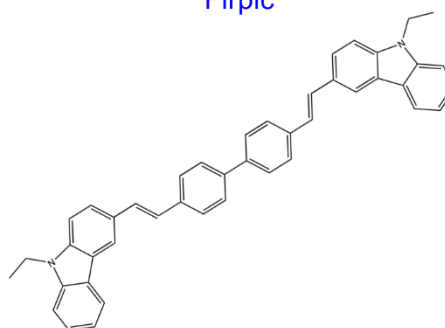
$\text{Ir}(\text{tptpy})_2(\text{acac})$



Firpic



$\text{Ir}(\text{ppy})_3$



BCzVBi

Figure 2.3 Chemical structures of iridium(III) bis(4-(4-*t*-butylphenyl)thieno[3,2-*c*]pyridinato-*N,C20*)acetylacetonate ($\text{Ir}(\text{tptpy})_2(\text{acac})$) as yellow emitter [62], Bis[2-(4,6-difluorophenyl)pyridinato-*C2,N*](picolato)iridium(III) (Firpic) as blue emitter, Tris[2-phenylpyridinato-*C2,N*]iridium(III) ($\text{Ir}(\text{ppy})_3$) as green emitter, and 4,4'-bis(9-ethyl-3-carbazovinylene)-1,10-biphenyl (BCzVBi) as blue emitter.

2.2 Device Fabrication and Characterization Methods

2.2.1 Device Fabrication Methods

All devices used in this thesis have slightly different structures in each chapter to obtain optimized performances. Typical device fabrication methods are as follows: The patterned ITO coated glass substrates were cleaned in ultrasonic bath (Branson 5510) with acetone, isopropyl alcohol, and deionized water. The cleaned substrates were dried in ambient oven at 120 °C for more than 1 hour. For the standard structure, ITO coated glass substrates were treated with ultraviolet-ozone cleaner (UVO-42) to remove the surface hydrocarbon contamination and increase the work function of the ITO. The vacuum deposition of thin films was performed by thermal evaporation under a base pressure of $1-5 \times 10^{-6}$ Torr at a rate of 0.2-2 Å/s for organic semiconducting materials, 0.1–0.2 Å/s for LiF (electron injection material), 0.2–0.5 Å/s for MoO₃ (hole injection material) and 3–5 Å/s for Al (metal cathode or anode), respectively. The evaporation speed was monitored with a quartz-oscillator thickness monitor. The doping concentration was adjusted by varying the relative evaporation speeds of the host and dopant materials. For the fabrication of transparent electrode using D/M/D structure with stochastic thermally self-aggregated Ag NPs, the thin Ag layer was deposited on the UV-ozone cleaned glass at a rate of 0.5-0.8 Å/s. Afterwards, the layer was heated at 450 °C in a furnace for 20 minutes. Then, the glass with TSA-Ag NPs was fully covered by 200 nm of commercialized LIP, Ormoclear, (Micro resist technology GmbH) by spin-coating to prevent the device from exciton quenching induced by non-encapsulated metallic NPs. We carefully choose the polymer as a dielectric of D/M/D electrode, because of its transparency at visible wavelength and refractive index (1.5), close to that of glass. After the LIP was irradiated under UV

and annealed at 150 ° C, a firm and flat dielectric film was obtained. After that, organic layers and metal electrode was deposited.

2.2.2 Current-Voltage-Luminance Measurement

Fabricated device was mounted onto the cryostat for the current-voltage-luminance (I-V-L) measurement. The emitting area is $1.4 \times 1.4 \text{ mm}^2$ which is defined by the crossing overlap of patterned ITO and Al electrodes. Most of the devices were measured at room temperature.

The current-voltage (I-V) characteristics were measured with a Keithley 236 source measurement unit, while the electroluminescence was measured with a calibrated Si photodiode (Hamamatsu, S5227-1010BQ) with a size of $10 \text{ mm} \times 10 \text{ mm}$ placed at an angle normal to the device surface, assuming that the device was a Lambertian source. To detect a turn-on voltage of light-emitting diodes, we use an ARC PD438 photomultiplier tube (PMT) with the Keithley 236 source measurement unit. The electroluminescence (EL) spectra and the Commission Internationale de L'Eclairage (CIE) color coordinates were measured with a Konica-Minolta CS-1000A spectroradiometer. The luminance and efficiency were calculated from the photocurrent signal of photodiode with a Keithley 2000 multimeter, and corrected precisely with the luminance from CS-2000 (see Figure 2.4).

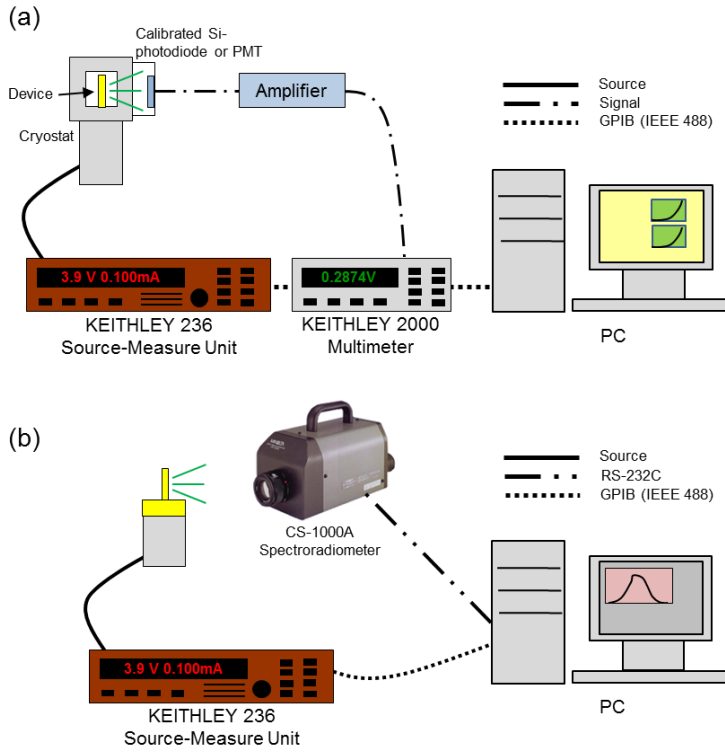


Figure 2.4 Schematic diagrams for the measurement of (a) I-V-L characteristics and (b) EL spectra.

The chromatic characteristics were calculated from EL spectra measured by the CS-1000A spectrometer using the CIE 1931 color expression system. The tristimulus values XYZ can be calculated by following equations,

$$X = K_m \int_0^{\infty} \bar{x}(\lambda)P(\lambda)d\lambda \quad (2.1)$$

$$Y = K_m \int_0^{\infty} \bar{y}(\lambda)P(\lambda)d\lambda \quad (2.2)$$

$$Z = K_m \int_0^{\infty} \bar{z}(\lambda)P(\lambda)d\lambda \quad (2.3)$$

where, $P(\lambda)$ is a given spectral power distribution of emissive source, \bar{x} , \bar{y} and \bar{z} are the CIE standard color matching functions (see Figure 2.5) and K_m is the weighing

constant (683 lm W^{-1}). From the tristimulus values, the CIE color coordinates calculated by following equations,

$$x = \frac{X}{X+Y+Z} \quad (2.4)$$

$$y = \frac{Y}{X+Y+Z} \quad (2.5)$$

$$z = \frac{Z}{X+Y+Z} \quad (2.6)$$

Any color can be plotted on the CIE chromaticity diagram.

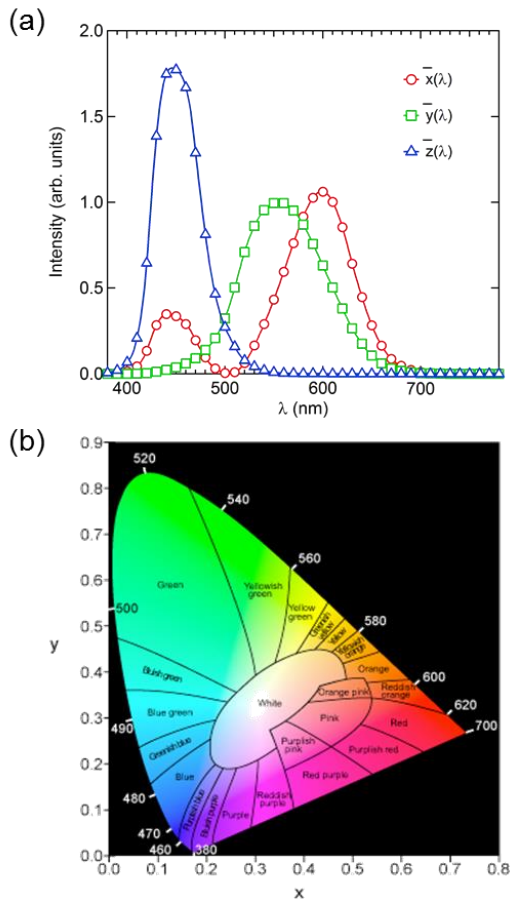


Figure 2.5 (a) The CIE standard observer color-matching functions and (b) the CIE 1931 color space chromaticity diagram. The outer boundary is the spectral locus, with wavelengths shown in nanometers.

2.2.3 Efficiency Calculation Methods

To evaluate the emission properties of light-emitting diodes, the commonly employed efficiencies are the external quantum efficiency (EQE), the luminous efficiency (LE) and the power efficiency (PE).

The external quantum efficiency can be defined by the following equation.

$$\text{EQE} = \frac{\text{number of emitted photons}}{\text{number of injected electrons}} (\%)$$

Typically, QLEDs or OLEDs emit light into the half plane due to the metal contact. Without any modification for increasing out-coupling efficiency, over 80% of the emission can be lost to internal absorption and wave-guiding in a simple planar light-emitting device.

Since human eye has different spectral sensitivity in visible area, the response of the eye is standardized by the CIE in 1924 (see \bar{y} in Figure 2.5). The luminous efficiency weighs all emitted photons according to the photopic response of human eye. The difference is that EQE weighs all emitted photons equally. LE can be expressed by the following equation.

$$\text{LE} = \frac{\text{luminance}}{\text{current density}} (\text{cd A}^{-1})$$

The luminance value (cd m^{-2}) can be easily measured by the commercial luminance meter (CS-1000A in this thesis).

The power efficiency is the ratio of the lumen output to the input electrical power as follows,

$$\text{PE} = \frac{\text{luminous flux}}{\text{electrical power}} (\text{lm W}^{-1})$$

The EQEs can be useful to understand the fundamental physics for light emission mechanism, while the PEs can be useful to interpret the power dissipated in a light-emitting device when used in a display application.

2.2.4 Angular Dependent Electroluminescence Measurement

Angular dependent EL intensity and spectra were measured from 0° to 90° by using an optical fiber and an Acton Spectro-275 monochromator combined with an ARC PD438 PMT on a rotation stage. A schematic diagram of this measurement system is depicted in Figure 2.6.

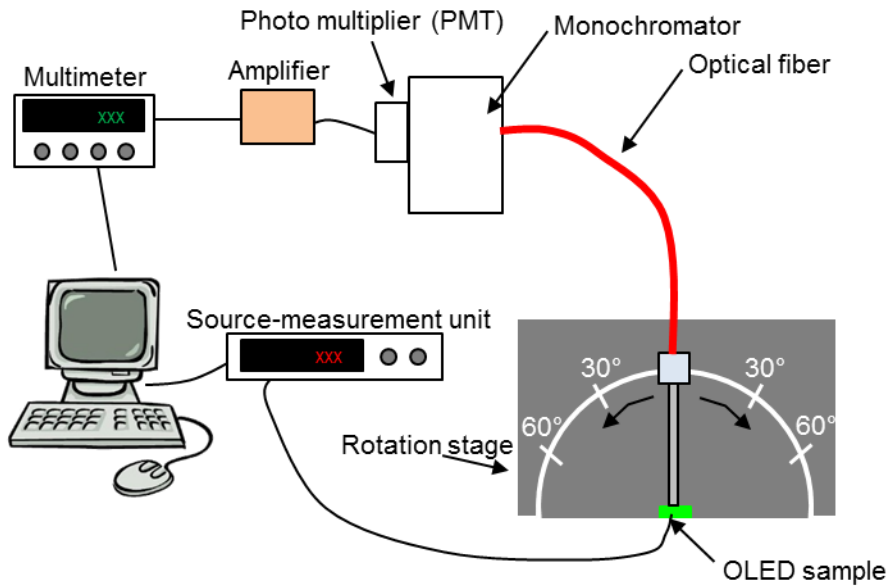


Figure 2.6 A schematic diagram of the angular dependent EL measurement set up.

2.2.5 Other Characterization Methods

UV-Visible Spectroscopy: The transmission and absorption spectra were measured with DU-70 UV/Vis Scanning Spectrophotometer (Beckman Coulter, Inc.) or Agilent 8454 UV-Vis. diode array spectrometer. In case of solution, materials were dissolved in toluene or chlorobenzene. For the film measurement, materials were spin-coated or evaporated thermally in the thickness of ~50 nm on quartz substrate. The reflectance spectra were measured by a Varian Cary 5000 spectrophotometer. The average transmittance (T_{avg}) was calculated by the following equation.

$$T_{\text{avg}} = \frac{\int_{\lambda_1}^{\lambda_2} T(\lambda) d\lambda}{\lambda_2 - \lambda_1} \quad (2.7)$$

Where $T(\lambda)$ is the transmittance as a function of the wavelength, T_{avg} was usually calculated by integrating $T(\lambda)$ from 400 nm (λ_1) to 800 nm (λ_2).

Atomic Force Microscopy (AFM): Topography of each film was measured by XE-100 (Park Systems) AFM System. Most of the films were measured in non-contact mode with NCHR probe tip (320 kHz, 42 N m⁻¹) followed by image processing in XEI v.1.7.1.

Scanning electron microscopy (SEM): SEM is a technique to observe topography and composition of samples' surface with a resolution of a few nanometers. It scans a focused electron beam over the sample to produce images. To gain images of thermally self-aggregated Ag NPs in **Chapter 4**, SEM (JEOL JSM-6701F) was employed.

Film Thickness Measurement: Ellipsometers (L2W15S830 with 632.8-nm He-Ne laser light, Gaertner Scientific Corp. and M2000D, Woollam) and an AFM (XE-100, Park Systems) were used for measuring the thicknesses of films

Impedance spectroscopy: Impedance spectroscopy is an useful tool to obtain more information about electrodynamic processes such as interface and bulk characteristics of the devices in OLEDs [63-65]. In this thesis, the impedance and phase measurements for OLED devices were performed by an impedance analyzer (Wayne Kerr Electronics, 6550B) with increasing voltage bias at 1kHz. The impedance spectroscopy was fitted using ZView software.

2.3 Theory

2.3.1 Space-Charge-Limited Measurement

Space-charge-limited current (SCLC) measurement is one of the most widely used techniques for determining charge carrier mobility in organic devices. To measure the SCLC, the typical device structure is sandwiched organic semiconductor layer between two metal electrodes that make ohmic contact on one side, so that, only single carrier (hole-only or electron-only) can transport.

In the low voltage region, current varies linearly with the voltage, which shows free carrier conduction following Ohm's law. However, at higher voltage above V_{SCLC} , current presents a quadratic dependence on the voltage ($J \propto V^2$). Considering the field-dependent mobility, the J-V characteristics thus can be modeled as follows [66, 67]:

$$J = \frac{9}{8} \varepsilon_0 \varepsilon_r \mu_0 \exp(\beta \sqrt{F}) \frac{V^2}{d^3} \quad (2.1)$$

where ε_0 and ε_r represent the permittivity of free space and relative dielectric constant, respectively, μ_0 is the zero-field mobility, β is the Pool-Frenkel (PF) coefficient, F is the applied electric field, and d is the thickness of active layer. Using the Equation (2.1), charge carrier mobility can be extracted from this space-charge-limited region. On the other hand, when traps are involved, current can follow a power law behavior on the voltage ($J \propto V^{m+1}$), where the exponent l is given by trap energy $E_t = kmT$ depending on the temperature. The J-V characteristics of trap-charge-limited current (TCLC) conduction model are given as [68, 69]:

$$J = q^{l+1} \mu N_v \left(\frac{2l+1}{l+1} \right)^{l+1} \left(\frac{\varepsilon_0 \varepsilon_r}{N_t} \frac{l}{l+1} \right)^l \frac{V^{l+1}}{d^{2l+1}} \quad (2.2)$$

where N_t is the trap density and N_v is the effective density of states.

2.3.2 Plasmonic Effect

Plasmonic effect, the interaction between metallic film and nanoparticles (NPs), is a practical technique to control the local electric field density. When the incident light irradiates the metallic structure, the electric polarization of free carrier, hole and electron, occurs. This polarization causes the change of local E field at the resonance wavelength. According to the H.A. Atwater and A. Poleman, three methods to increase light intensity inside organic electronics using plasmonic effects have been suggested [70]. The plasmonic effects can be categorized as three ways: scattering, localized surface plasmons resonance (LSPR), and surface plasmon polaritons (SPP).

The scattering is a general physical process when the light collides with other particles, which change the path of straight direction to random direction in the medium. The scattering between light and NPs can be categorized into three sections, depending on the size of NPs as shown in Figure 2.7. First one is geometric scattering (size of NP \gg wavelength of incident light) when the light interacts with micro scale particles. The other major forms of elastic light scattering are Rayleigh scattering (size of NP $<$ wavelength of incident light) and Mie scattering (size of NP \approx wavelength of incident light), which occur when the size of NPs are comparable to the wavelength of light. The Mie and Rayleigh scattering are generally occurred when sub hundred nanometer sized NPs are incorporated in dielectric materials. And this scattering effect change the directionality of incident light, which elongated light paths outside the substrate. This increased beam path allows OLED to enhance out-coupling efficiency. Therefore, the scattering effect from NPs is one of ways to improve light extraction in OLEDs

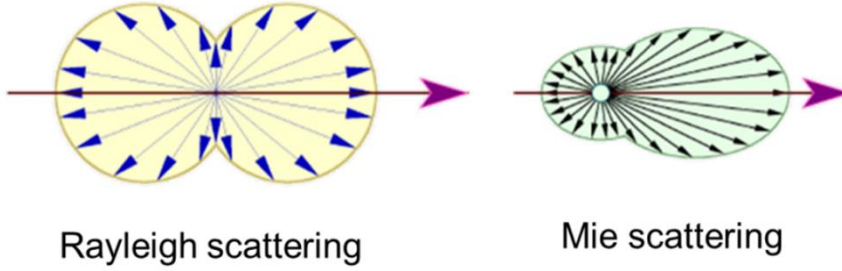


Figure 2.7 Electric field patterns of Rayleigh and Mie scattering.

When the oscillation of the free electrons in NPs is matched with an incident light, the intensity of local electric field can be enhanced. This is called as a LSPR. Figure 2.8 illustrates the origin of LSPR in the media with NPs. Aforementioned the resonance peak of LSPR can be solved by the Mie theory, when the NP size is shorter than the wavelength of incident light [71]. This is a model consists of the rigorous resolution of Maxwell's equation by taking both the electromagnetic field diminished in NPs and the field scattered by the NPs into account. The extinction coefficient $\sigma(\omega)$, “absorption-scattering cross-section”, is calculated by following equation [72]

$$\sigma(\omega) = \frac{9N\omega V \varepsilon_s^{\frac{3}{2}}}{c} \left(\frac{\varepsilon_2(\omega)}{[\varepsilon_1(\omega) + 2\varepsilon_s(\omega)]^2 + \varepsilon_2^2(\omega)} \right) \quad (2.3)$$

where $\omega=2\pi/\lambda$ is the pulsation of the incident electromagnetic field, c the speed of light, V the volume of single NP, N the density of NPs. And the ε_s , ε_1 , ε_2 and ε_m , are the dielectric constant of the surrounding medium, the real part of metal, the imaginary part of metal, and combination of two components ($\varepsilon_m=\varepsilon_1+i\varepsilon_2$), respectively. According to Eq. (2.3), scattering intensity is maximized, when $[(\varepsilon_1(\omega)+2\varepsilon_s(\omega))^2+\varepsilon_2^2(\omega)]$ is zero. This condition is called the localized surface plasmon resonance. Generally, ε_1^2 is much higher than ε_2^2 in Ag, the localized plasmon resonance wavelength of a layer integrating NPs occurs $\varepsilon_1(\omega)=-2\varepsilon_s(\omega)$. From this

method, the resonance wavelength of NPs can be easily derived. Therefore, the peak of localized surface plasmon resonance can be tuned by changing the material of NPs and surrounding media.

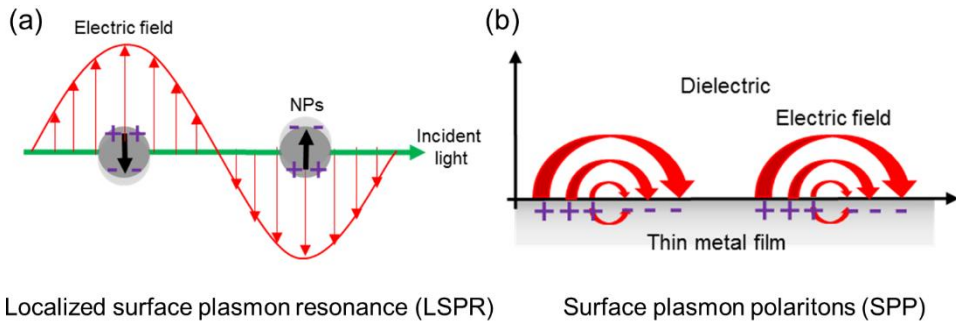


Figure 2.8 Schematic of the plasmon effect of NPs.

It has been already explored that the peak of resonance from NPs surrounded by high ϵ_s is longer than that enclosed by low ϵ_s . Additionally, the LSPR frequency depends on the size and shape of the NP, and the NP material.

Chapter 3

OLED PIXEL STRUCTURE WITH SIMPLIFIED PATTERNING USING THE YELLOW COMMON LAYER

To extend the OLED display market, it is important to reduce the price by simplifying the OLED fabrication process [73]. Conventional full-color OLEDs are produced by the RGB side-by-side method, which uses different fine metal shadow mask (FMM) steps to pattern red, green, and blue (RGB) emission layers (EMLs), respectively [14, 16, 27]. These complicated and time-consuming processes are the factors that prevent OLED displays from being price-competitive compared to liquid crystal displays (LCDs). Additionally, these steps cannot easily achieve a high

resolution because of the mask sagging phenomenon in the large area display [16, 28, 74].

Therefore, some innovative methods exist to reduce the FMM steps and increase the resolution while maintaining a performance comparable to conventional OLEDs, such as white OLEDs (WOLEDs) with color filters (CFs), blue common layer (BCL) and yellow/blue (Y/B) OLEDs with CFs. Despite these remarkable results, it still requires simplified FMM EML patterning steps.

Here, we demonstrated further simple and effective pixel architectures for full-color OLED displays employing a yellow common layer (YCL) in Y/B OLEDs. By using a YCL, we implemented a single EML patterning step for full-color pixels to develop conventional Y/B OLEDs. In addition, from this structure, we utilized all the advantages of UDC's pixel architecture, preserving the overall performance compared to the architecture without the YCL. Therefore, it is possible to achieve a simplified process and low-cost of OLED manufacturing with a long lifetime and high resolution in large area displays. Because the YCL acts as an emission layer (EML) in the yellow device and a hole transport layer (HTL) in the blue device, we investigated the effect of the YCL on the yellow and blue device by adopting various HTL host materials. To achieve an equivalent device performance after employing the YCL, we introduced a way to select the HTL material and control the YCL. Moreover, by employing red and green double layer instead of yellow layer, we could enhance the color gamut of the device.

3.1 Device Configuration of Yellow/Blue OLED with A Yellow Common Layer

Figure 3.1 (a) illustrates the YCL-OLED structure where only blue sub-pixels are formed by applying just one FMM step, and the red and green sub-pixels are established with the red and green CFs on the yellow OLEDs. The YCL acts as a yellow EML on the red, green and yellow sub-pixels and as a HTL on the blue sub-pixels. YCL-OLEDs can achieve full-color displays (RGYB) with CFs using a single FMM step, as shown in Figure 3.1 (b). Table 3.1 shows device structures of a blue sub-pixel with a YCL (B1), a blue sub-pixel without a YCL (B2) and a yellow sub-pixel (Y1).

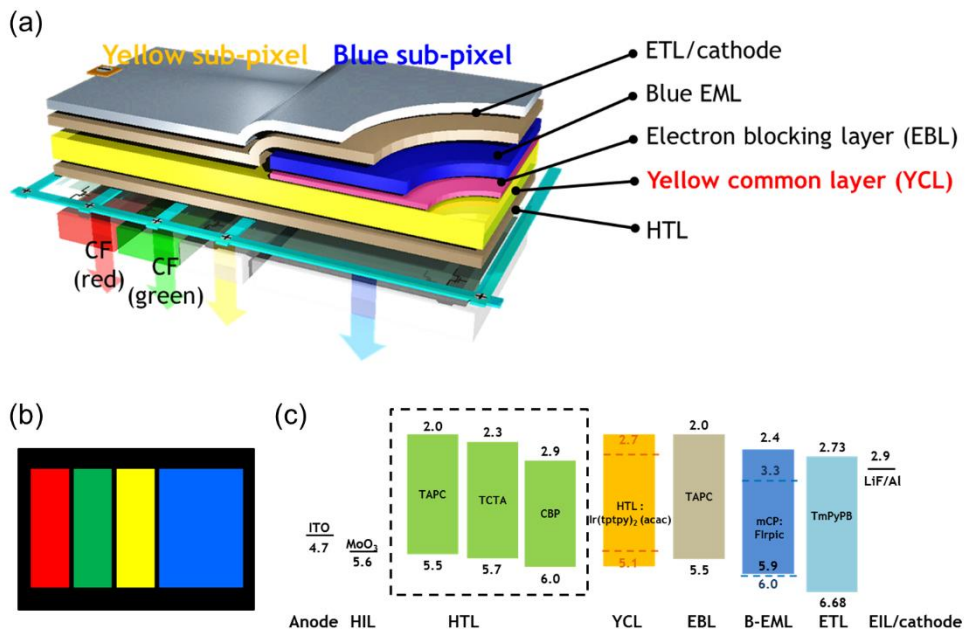


Figure 3.1 (a) Schematic diagrams of full-color OLEDs with a YCL structure, (b) pixelation of red, green, yellow, and blue sub-pixels, (c) the energy level diagram of the blue device using the YCL with different HTLs.

Table 3.1 Device structures of blue and yellow OLEDs

Device layer structures	
B1	ITO/MoO ₃ (10 nm)/HTL (50 nm)/TAPC (10 nm)/Firpic:mCP (8 wt%, 15 nm)/TmPyPB (40 nm)/LiF (0.8 nm)/Al (100 nm)
B2	ITO/MoO ₃ (10 nm)/HTL (35 nm)/YCL (15 nm)/TAPC (10 nm)/Firpic:mCP (8 wt%, 15 nm)/TmPyPB (40 nm)/LiF (0.8 nm)/Al (100 nm)
Y1	ITO/MoO ₃ (10 nm)/HTL (35 nm)/YCL (15 nm)/TmPyPB (40 nm)/LiF (0.8 nm)/Al (100 nm)

All OLED devices and hole-only devices (HODs) were fabricated on patterned indium tin oxide (ITO) glass substrates. The substrates were first cleaned with acetone, isopropyl alcohol and deionized water and then dried in an ambient oven at 120 °C. After exposing the substrates to UV-ozone for 10 minutes, organic layer and cathode were deposited by thermal evaporation under high vacuum ($<1 \times 10^{-6}$).

ITO as an anode and 10 nm of molybdenum trioxide (MoO₃) as a hole injection layer (HIL) were used for all three devices. For different HOMO energy levels of the hole transport materials, we adopted TAPC, TCTA, and CBP as HTLs with 5.5, 5.7, and 6.0 eV as the HOMO energy levels, as shown in Figure 3.1 (c) [58-60]. These HTL materials were used only as HTLs at B2, whereas these were used as the host of the YCL at Y1. We employed Ir(tp₂py)₂(acac) as an efficient yellow dopant with different HTL host materials in a YCL [62]. To suppress exciton transfer from the blue emitting layer (EML), we used 10 nm of a TAPC layer as an electron blocking layer (EBL) at B1 and B2 [29]. For the efficient blue EML, we used Firpic and mCP as a blue dopant and a blue EML host, respectively. As an electron transport layer (ETL), an electron injection layer (EIL) and a cathode, we employed 40 nm of TmPyPB, 0.8 nm of lithium fluoride (LiF), and 100 nm of aluminum (Al). In addition, the structure

of HOD is ITO/MoO₃ (10 nm)/HTL or HTL:Ir(tp₂py)₂(acac) (100 nm)/MoO₃ (10 nm)/Al (100 nm) with the same HTLs (i.e., TAPC, TCTA and CBP).

3.2 Characteristics of A Yellow Common Layer and An Electron Blocking Layer

3.2.1 Negligible Optical Effect of Yellow Doped Common Layer

Before fabricating devices, to confirm whether there are unexpected optical effects by inserting the YCL, we measured the absorption spectra of pristine TAPC, TCTA and CBP films (30 nm) and of those films doped with the yellow dopant (8 wt%, 30 nm). From Figure 3.2, no significant absorption peak was shown over the entire visible color range before and after the yellow dye doping, showing that the optical effect from YCL is almost negligible for the blue device B2.

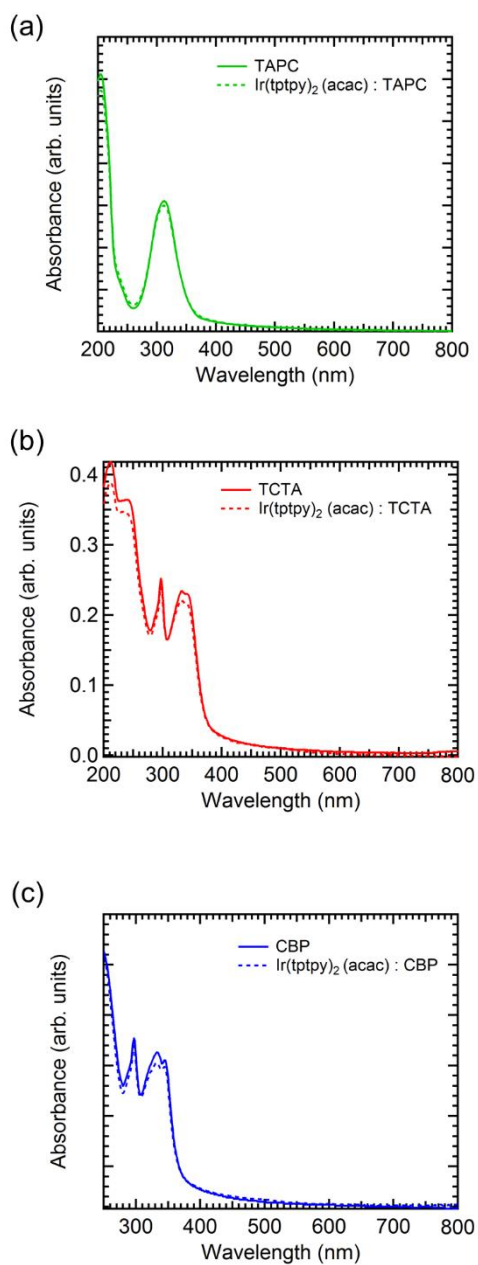


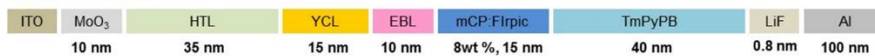
Figure 3.2 Absorption spectra of films with pristine and of Ir(tppy)₂(acac)-doped (a) TAPC, (b) TCTA and (c) CBP.

3.2.2 Insertion of Electron Blocking Layer for Suppressing Energy Transfer between Blue and Yellow Emission Layer

To suppress the exciton transfer from blue EML to the YCL, we fabricated the blue device with EBL and without EBL as shown in Figure 3.3 (a). We inserted an electron blocking layer (EBL) of TAPC, which has high LUMO level and high hole mobility to block the electron and confine exciton in the EML as shown in Figure 3.3 (b). To block the exciton transfer completely, we used proper thickness of TAPC (10 nm) [29]. Figure 3.4 shows the importance of insertion of EBL. The EL spectra of the blue devices without EBL of TAPC layer clearly show the yellow peak from Ir(tp₂py)₂(acac) irrespective of HTLs, which is different from the EL spectra of the blue devices with EBL. Moreover, the efficiencies of the blue devices without EBL were very low compared to the blue device with EBL. This results from the exciton quenching process between the YCL and blue EML. Therefore, the role of EBL is very important for the full-color OLEDs using YCLs without color distortion.

(a)

Blue sub-pixel with EBL



Blue sub-pixel without EBL



(b)

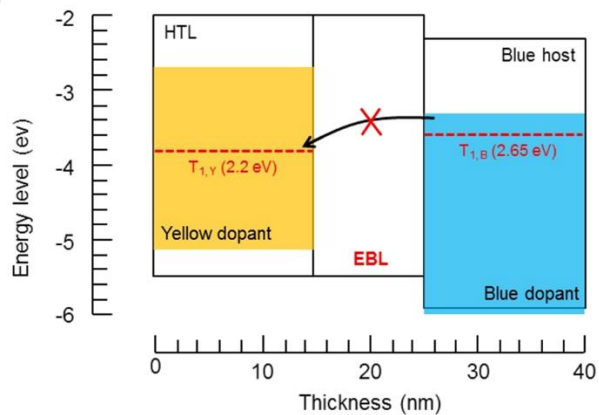


Figure 3.3 (a) Device structure of blue sub-pixel with EBL and without EBL and (b) schematic energy diagram of insertion of EBL between the YCL and blue EML.

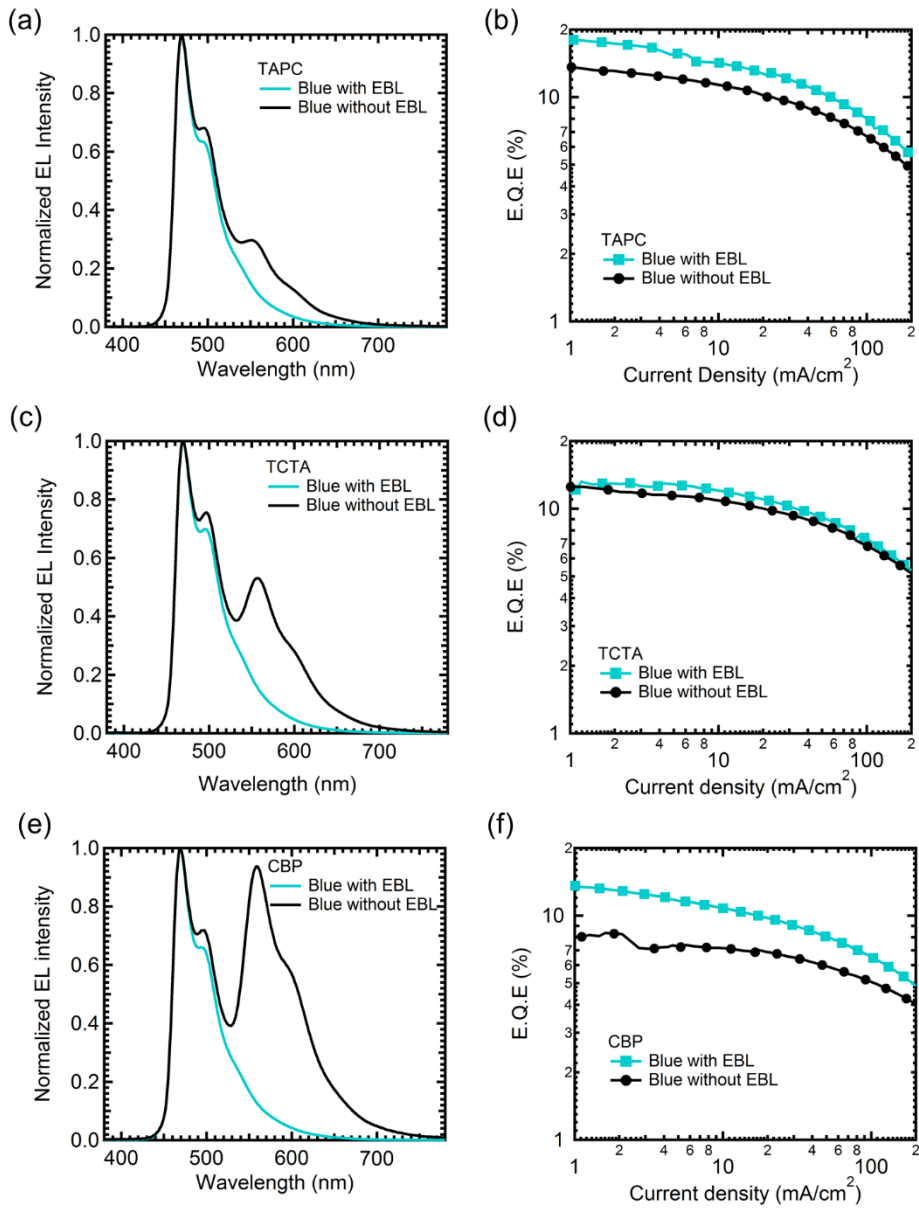


Figure 3.4 (a), (b), (c) Normalized EL intensity of blue with EBL and without EBL of TAPC, TCTA, and CBP and (d), (e), (f) E.Q.E–current density characteristics of blue with EBL and without EBL of TAPC, TCTA, and CBP.

3.3 Characteristics of Device Performance of Yellow/Blue OLED with A Yellow Common Layer

Because adopting YCL could have a negative effect on the blue device performance, we examined the device performance by employing some commonly used HTL materials (TAPC, TCTA and CBP). Figure 3.5 shows the current density–voltage (J–V) and L–V characteristics of devices B1, B2 and Y1 with TAPC, TCTA and CBP. In the blue devices without YCL (B1) and with YCL (B2), as shown in Figure 3.5 (a) and (b), the current densities of the devices decreased with the application of the YCL. For example, the current densities of devices B1 and B2 with all HTL host materials at 8 V are 17.7 mA/cm² (B1-TAPC), 13.3 mA/cm² (B2-TAPC), 39.1 mA/cm² (B1-TCTA), 18.0 mA/cm² (B2-TCTA), 14.1 mA/cm² (B1-CBP) and 1.5 mA/cm² (B2-CBP). Likewise, the turn-on voltage and driving voltage of the devices increased when the YCL was inserted. For instance, the turn-on voltages of device B1 with TAPC, TCTA and CBP are 3.4 V, 3.8 V and 3.8 V, and those of device B2 are 3.5 V, 3.9 V and 4.2 V, respectively. Additionally, the driving voltages of device B1 with TAPC, TCTA and CBP are 6.6 V, 6.4 V and 7.1 V, whereas those of the device B2 are 6.8 V, 6.8 V and 9.4 V, respectively. This indicates that the yellow dopant in the YCL in the blue devices acts as trapping sites, which disturb hole transport in the YCL. Thus, the yellow dopant lowers the hole mobility of the YCL in the blue devices and increases the driving voltage of device B2 compared to device B1.

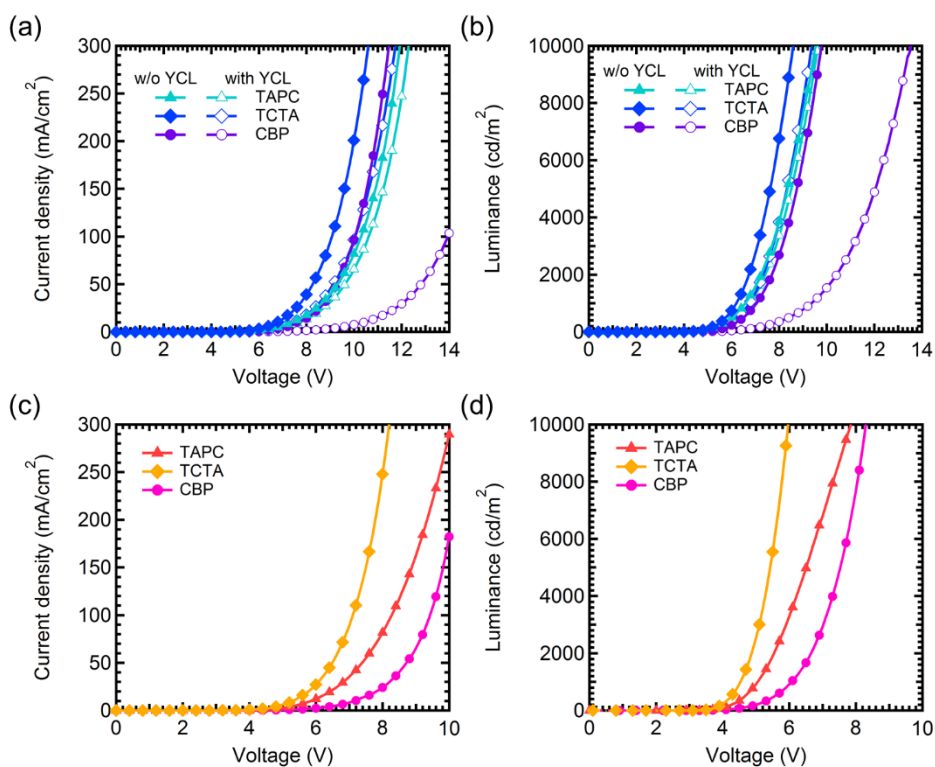


Figure 3.5 Current density–voltage and luminance–voltage characteristics for the (a), (b) B1, B2 and (c), (d) Y1 devices with different HTL materials.

To examine the performance of HTLs as hosts, we fabricated the yellow device Y1 with TAPC, TCTA and CBP. In Y1, as displayed in Figure 3.5 (c) and (d), the current density of the device with TCTA is higher than those of the other HTLs and hosts. At the same voltage (10 V), the current densities of the devices with TAPC, TCTA and CBP are 81.7 mA/cm², 247.6 mA/cm² and 24.1 mA/cm², respectively. Moreover, the turn-on voltage of the devices is 3.2 V (Y1-TAPC), 3.2 V (Y1-TCTA) and 3.5 V (Y1-CBP), respectively. Although a high mobility and low HOMO energy level difference of the yellow dopant and HTL of TAPC exist, the driving voltage of the device with TAPC is 5.1 V, which is higher than that of the device with TCTA (4.6 V). This means that TAPC is not an efficient yellow host despite its faster hole transport property than

the others. Additionally, the luminance of the Y1-TAPC is higher than that of the device with CBP at a low driving voltage, but it has a low luminance at a high driving voltage. Despite the high hole mobility of TAPC, the low electron mobility of TAPC causes accumulation of holes at the interface between the EML and ETL. As a result, triplet-polaron and triplet-triplet annihilation occur at a high driving voltage, which causes a rapid decrease in luminance [20, 75, 76]. Meanwhile, the devices with TCTA and CBP show high maximum luminance because of their bipolar transport properties, but the device with CBP shows a higher driving voltage than that with TCTA at the same luminance. As an illustration, the driving voltage was 4.6 V and 6.1 V for the devices with TCTA and CBP, respectively. A high HOMO-level difference between the HTL and the yellow dopant may increase the driving voltage because the main emission process of CBP host may be direct charge trapping at the dopant [77].

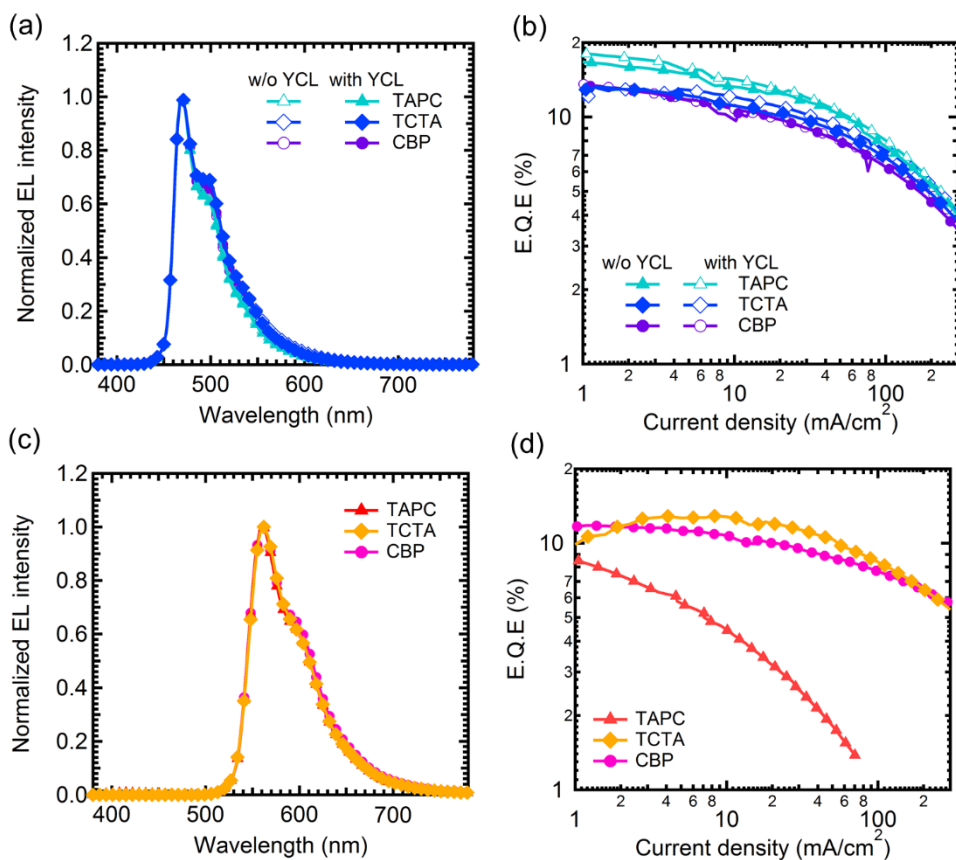


Figure 3.6 EL spectra and external quantum efficiency (EQE) of the devices (a), (b) B1, B2 and (c), (d) Y1 with different HTL materials.

Furthermore, to figure out which HTL is the best for the YCL, we compared the device performance of each HTL. Figure 3.6 (a) and (c) displays normalized EL spectra of devices B1, B2 and Y1 using TAPC, TCTA and CBP. Almost similar shapes of the spectra of the devices with different HTL host materials are observed without any other emission peaks. Likewise, changes in the CIE coordinates of the blue devices with and without YCL were negligible (Table 3.2). For instance, the CIE coordinates change (Δx , Δy) between devices B1 and B2 with TAPC, TCTA and CBP are (0.005, 0.006), (0.005, 0.003), and (0.004, 0.001), respectively. Furthermore, the

EBL successfully blocks energy transfer between the blue EML and the YCL in the B2 devices [58, 61]. This indicates that the YCL performs only a hole transport role in the blue devices without acting as an emission host in the yellow devices [14, 29]. Figure 3.6 (b) shows the EQE–J characteristics of devices B1 and B2. Owing to a high hole mobility of TAPC, the devices with TAPC exhibit slightly higher efficiencies than the other two cases. For example, the EQEs of devices B1 and B2 with TAPC, TCTA and CBP are (15.4%, 15.6%), (12.2%, 12.6%), and (12.0%, 11.8%), respectively, at 1000 cd/m². Overall, there are no significant differences in the EQEs of the devices with YCL and without YCL in all HTL cases. This suggests that the YCL does not notably affect the efficiency of the blue device. In the yellow devices, device Y1 with TAPC, TCTA and CBP shows similar EQEs at a low current density, but the device with TAPC shows rapid efficiency roll-off with increasing current density compared to the other two cases. For example, the EQEs of the Y1 device with TAPC, TCTA and CBP are 10.2%, 11.6% and 11.6%, respectively, at 1000 cd/m², whereas those are 4.0%, 11.5% and 9.3%, respectively, at 10000 cd/m². These results correspond to the low luminance of TAPC at high voltage from the aforementioned luminance characterization, and we could understand the influence of hole-dominant transport in the EML on the electron-hole imbalance and drastic roll-off [20]. Therefore, the HTL host materials for the YCL require not only high hole mobility for high efficiency in the blue device but also bipolar transport to achieve a low efficiency roll-off in the yellow device.

Table 3.2 Performances of devices with different YCLs.

YCL host	Device	J ^{a)} [mA/cm ²]	Voltage ^{b)} [V]	EQE ^{c)} [%]	LCE ^{d)} [cd/A]	LPE ^{e)} [lm/W]	CIE color coordinates ^{f)} [x,y]
TAPC	B1	17.7	6.6	15.4	26.7	12.7	[0.150, 0.289]
	B2	13.3	6.8	15.6	29.6	13.7	[0.155, 0.295]
	Y1	81.7	5.1	10.2	33.4	20.6	[0.490, 0.504]
TCTA	B1	39.1	6.4	12.2	23.0	11.5	[0.159, 0.318]
	B2	18.0	6.8	12.6	24.7	11.4	[0.164, 0.321]
	Y1	247.6	4.6	11.6	41.5	28.3	[0.492, 0.505]
CBP	B1	14.1	7.1	12.0	21.5	9.5	[0.157, 0.307]
	B2	1.5	9.4	11.8	21.5	7.2	[0.160, 0.306]
	Y1	24.1	6.1	11.6	37.6	19.4	[0.494, 0.503]

^{a)} Current density at 10 V, ^{b)} Driving voltage for 1000 cd/m², ^{c)} EQE at 1000 cd/m², ^{d)} Current efficiency at 1000 cd/m², ^{e)} Power efficiency at 1000 cd/m², ^{f)} measured at 5.1 mA/cm²

3.4 Dopant Trap Effect Caused by Hole Trap Depth

Furthermore, the changes in the device performance of devices B1 and B2 depend on the HTL host materials. To examine the correlation between the properties of the HTL host materials and the device performance, we inspected the effect of the hole trap depth, which is the HOMO-level difference between the HTL and the yellow dopant. The hole trap depths of the YCL with TAPC, TCTA and CBP are 0.4 eV, 0.6 eV and 0.9 eV, respectively (Figure 3.6 (a)). While little difference in the driving voltage between devices B1 and B2 was observed in the TAPC and TCTA cases, a significant difference was observed in the CBP cases, as shown in Figure 3.6 (b). For example, the driving voltage changes between B1 and B2 with TAPC, TCTA and CBP are 0.2 V, 0.4 V and 2.3 V, respectively. The driving voltage change from the B1 device to the B2 device increases with increasing hole trap depth. At the YCL in the blue device, the yellow dopant function as hole trap path, which decrease the hole mobility. As a result, as the hole trap depth deepens, the driving voltage of the blue device increases.

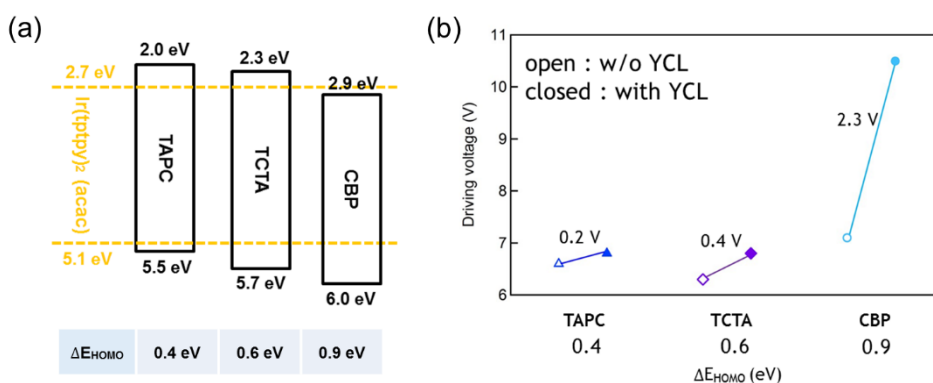


Figure 3.7 Schematic energy levels of Ir(tptpy)₂(acac)-doped TAPC, TCTA and CBP with the hole trap depth (ΔE_{HOMO}) calculated from the difference of the HOMO energy levels between the host and dopant materials, (b) driving voltage changes with and without the YCL with increasing ΔE_{HOMO} .

To further investigate the effect of the hole trap depth on the charge transport properties, we measured temperature dependent J–V measurements of the HODs with different HTLs. Figure 5 (a)-(f) shows the J–V characteristics for the HODs of the pristine HTLs and the yellow dopant-doped HTLs from 125 K to 300 K. As a result, the current densities of the HODs decreased at the same voltage as that when the hole trap depth increases. In addition, those of all the HODs decrease with the insertion of the yellow dopant in the HTLs. For instance, at 300 K, the current densities of the HODs using pristine HTLs at 4 V are 112.4 mA/cm² (TAPC), 70.8 mA/cm² (TCTA) and 52.9 mA/cm² (CBP). Those of the HODs using doped HTLs at the same voltage are 37.3 mA/cm² (TAPC), 4.5 mA/cm² (TCTA) and 0.004 mA/cm² (CBP).

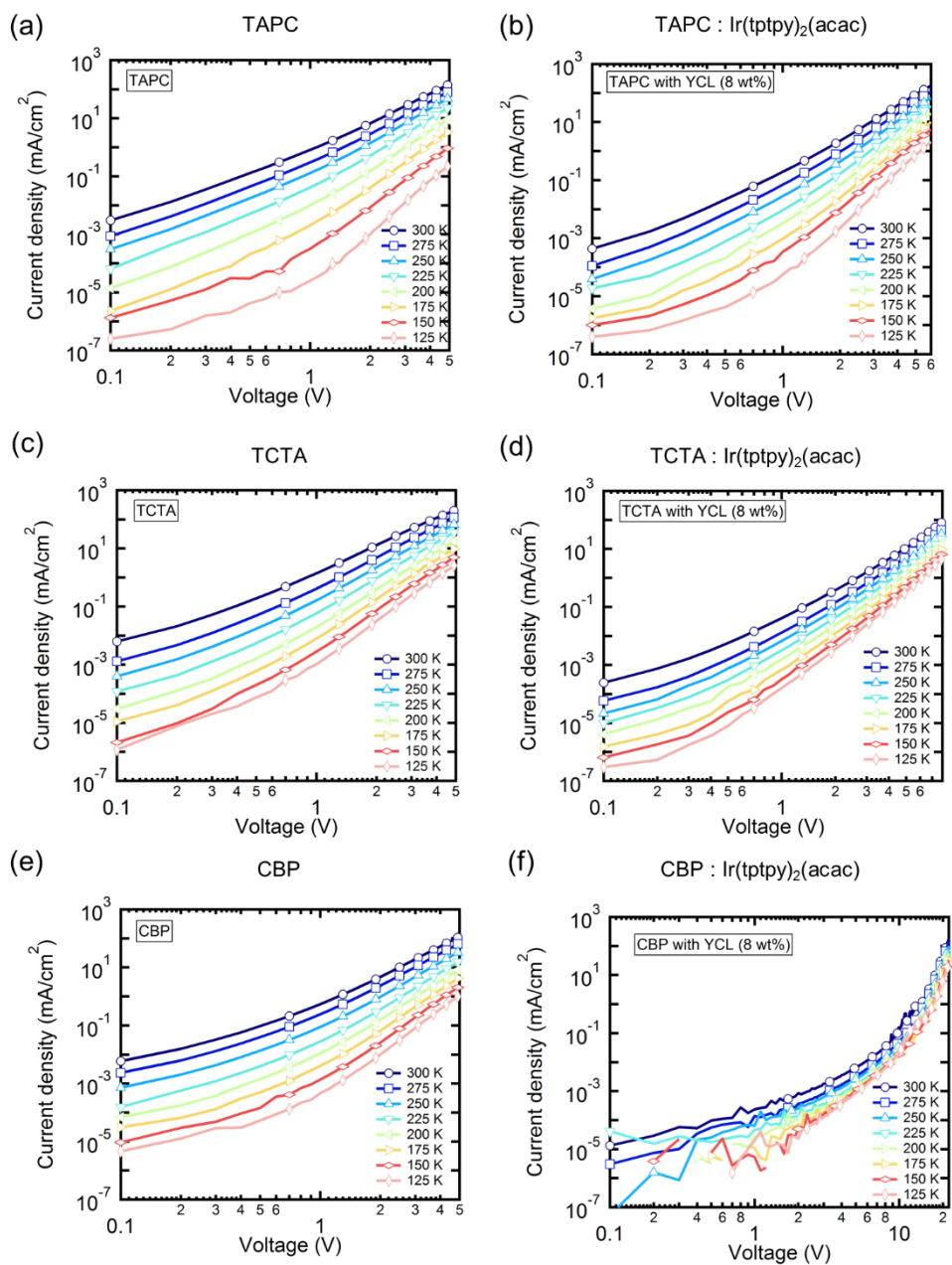


Figure 3.8 Current density–voltage characteristics of hole-only devices of different HTLs with and without Ir(tptpy)₂(acac) measured at various temperatures.

For further detail, in the low-voltage region, the current density varies linearly with the voltage, indicating the ohmic contact region due to free carrier conduction. On the other hand, in the high-voltage region, the current density follows a power law on the voltage ($J \propto V^{(m+1)}$) called the trap-charge-limited current (TCLC) conduction model given as Equation (1):

$$J \cong \frac{N_v e \mu_h}{N_t^m} \left(\frac{\epsilon_r \epsilon_0}{e} \frac{m}{m+1} \right) m \left(\frac{2m+1}{m+1} \right)^{(m+1)} \frac{V^{m+1}}{d^{2m+1}} \quad (1)$$

where N_t is the trap density, N_v is the effective density of states, ϵ_0 and ϵ_r are the permittivity of free space and relative dielectric constant, respectively. This conduction model occurs when traps are involved in charge transport. The exponent m provides trap energy $E_t = kmT$ depending on temperature [68, 69]. From the slope of m versus $1/T$ curve shown in Figure 3.8, the trap energy can be obtained. The pristine HTL HOD trap energies are almost similar. With the incorporation of the yellow dopant, trap energies increase in all the HTLs. Moreover, as hole trap depths are deeper, the changes of the trap energies are larger. For example, the trap energies of pristine HTLs and $\text{Ir}(\text{tptpy})_2(\text{acac})$ -doped HTLs with TAPC, TCTA and CBP are 34.7 meV (pristine TAPC), 35.1 meV (pristine TCTA), 36.4 meV (pristine CBP), 37.1 meV (doped TAPC), 42.8 meV (doped TCTA) and 55.5 meV (doped CBP), respectively. These results from the temperature dependent J - V characteristics correspond to the tendency between the driving voltage and trap depth from the blue device performance, and we could realize the influence of the trap energy in the YCL on the driving voltage of the blue device [78, 79]. Thus, it is suggested that TAPC and TCTA, which have smaller hole trap depths and trap energies than CBP, are appropriate for the YCL in blue devices. However, TCTA is a more suitable HTL material considering the simultaneous role in both yellow and blue devices due to the low efficiency of the yellow device with TAPC from its hole-dominant property.

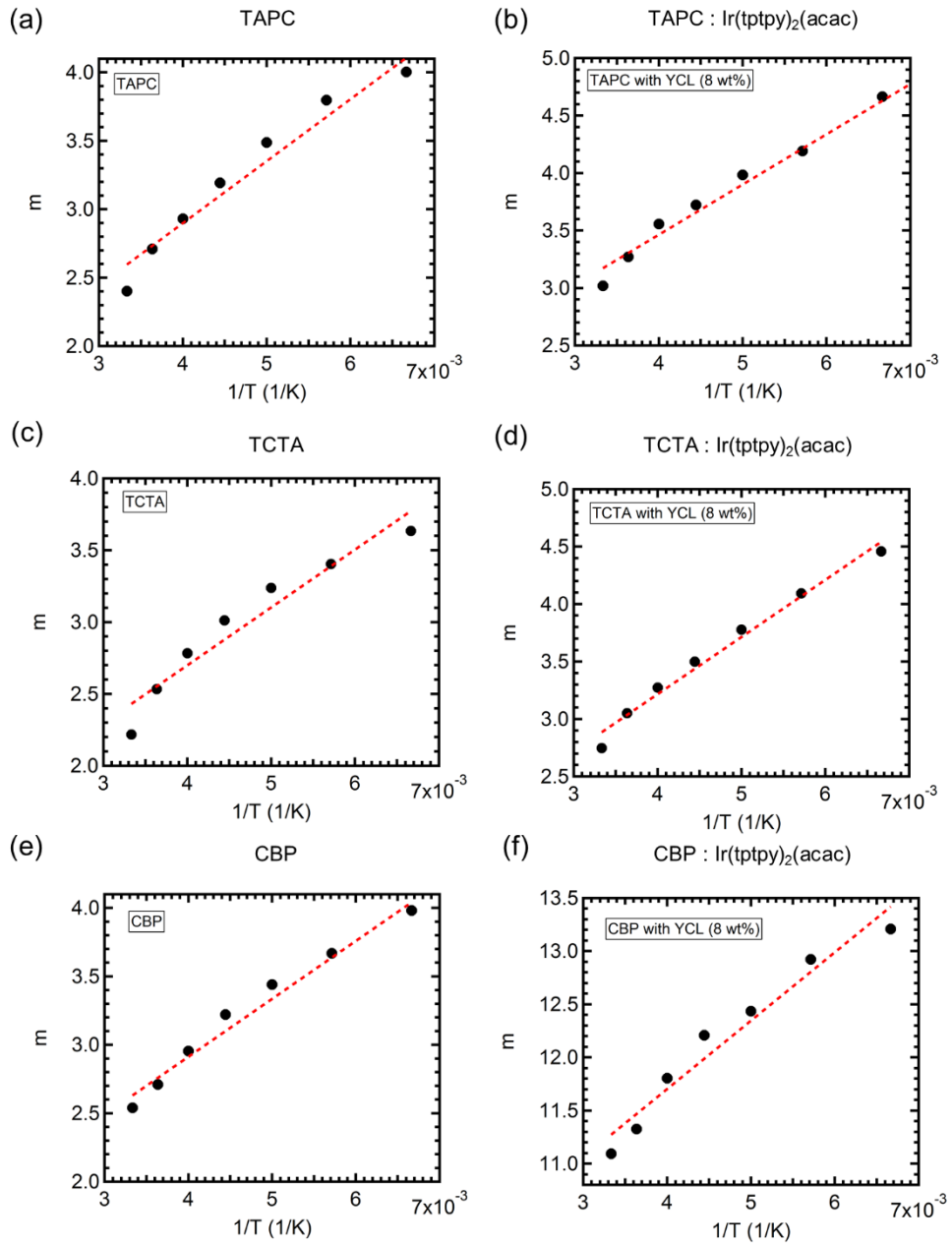


Figure 3.9 Temperature dependence of m from Equation (1) and its linear fitting curve of the hole-only devices of different HTL materials with and without the yellow dopant in order to extract trap energy.

3.5 Dopant Trap Effect Caused by Hole Trap Density

For the efficient yellow device, it is important to control the doping concentration of the yellow EML. Nevertheless, the doping concentration of the yellow dopant in the YCL, defined as the trap density, could affect hole transportation in the blue device. To understand the relationship, we fabricated HODs by varying the doping concentration of the yellow dopant in HTLs. J–V characteristics are shown in Figure 3.9 by varying the doping concentration of the yellow dopant, which was controlled from 0 wt% to 8 wt%. As the doping concentration increases, a gradual decrease in the current density at the same voltage is observed in all the HTLs. Despite a low doping concentration and as an exception, at high voltage (> 4 V), the HOD with TAPC (3 wt%) had a lower current density than that with TAPC (8 wt%). This may be due to the many shallow traps between TAPC and $\text{Ir}(\text{tptpy})_2(\text{acac})$ (< 0.4 eV) acting as hole hopping sites and improving hole transportation [80]. Even so, the amount of decrease in the current density steadily increases with increasing trap depth overall. These data imply that the many trap sites of the yellow dopant suppress efficient hole transport in the HTL. Based on these results, we speculate that the trap density, which is relative to the doping concentration of $\text{Ir}(\text{tptpy})_2(\text{acac})$, is one of the key elements for controlling the change in the driving voltage in the device.

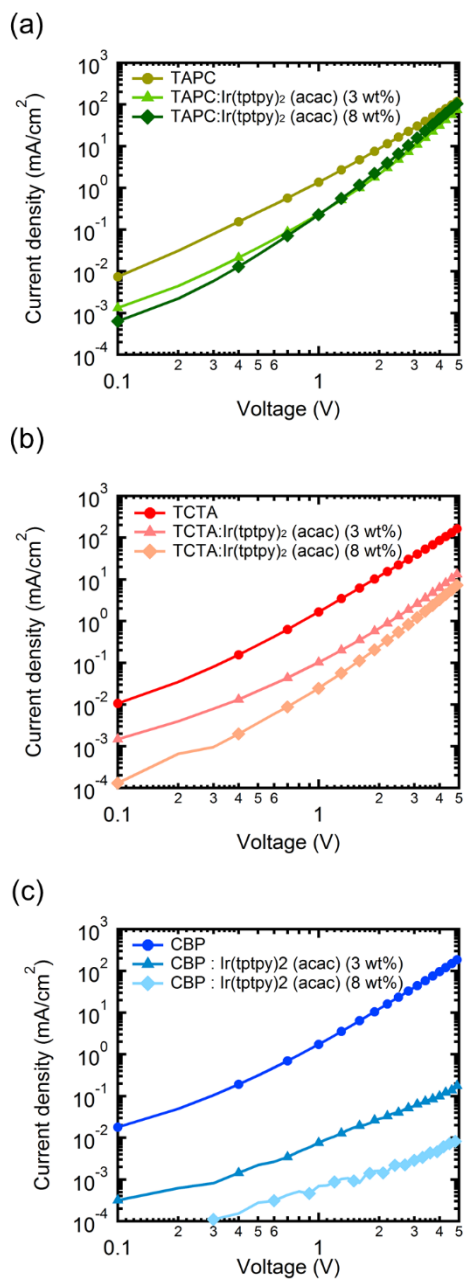


Figure 3.10 Current density–voltage characteristics of hole-only devices with pristine and different doping concentration of Ir(tppy)₂(acac)-doped (a) TAPC, (b) TCTA and (c) CBP.

To examine the influence of the trap density on the HOD electrical properties, we conducted measurements with impedance spectroscopy, which is a practical technique to analyze carrier injection and transportation [65]. Figure 3.10 shows the impedance versus voltage ($Z-V$) and phase versus voltage ($\phi-V$) characteristics of the HODs. At low voltage (<1 V), all the HODs exhibited a high impedance and an approximate phase of -90° , which indicates a purely capacitive response and an insulating state. With increasing voltage, the impedance of the HODs began to decrease, and the phase began to approach 0° . Finally, impedance of all the HTLs reached almost 0, and the phase also changed to approximately 0° , which means a purely conducting state [63, 64, 81]. This phenomenon has been observed in all the HODs, but the speed of transition from an insulating state to a conducting state is different depending on the trap depth and trap density. The pristine HTLs (TAPC, TCTA and CBP) are almost changed to a conducting state at the same voltage (approximately 2 V). However, the doped HTLs had different changes, which were attributed to the trap effect of the yellow dopant. As the hole trap depth and trap density increased, slow transitions were observed, which agree with the result from the $J-V$ characteristics of HODs, indicating that the yellow dopant in the HTLs impedes the transition from an insulating state to a conducting state. Specifically, the influence of this interference could be affected by the hole trap depth and trap density. In the end, this difference of transition contributes to an increased driving voltage of the device by insertion of the yellow dopant.

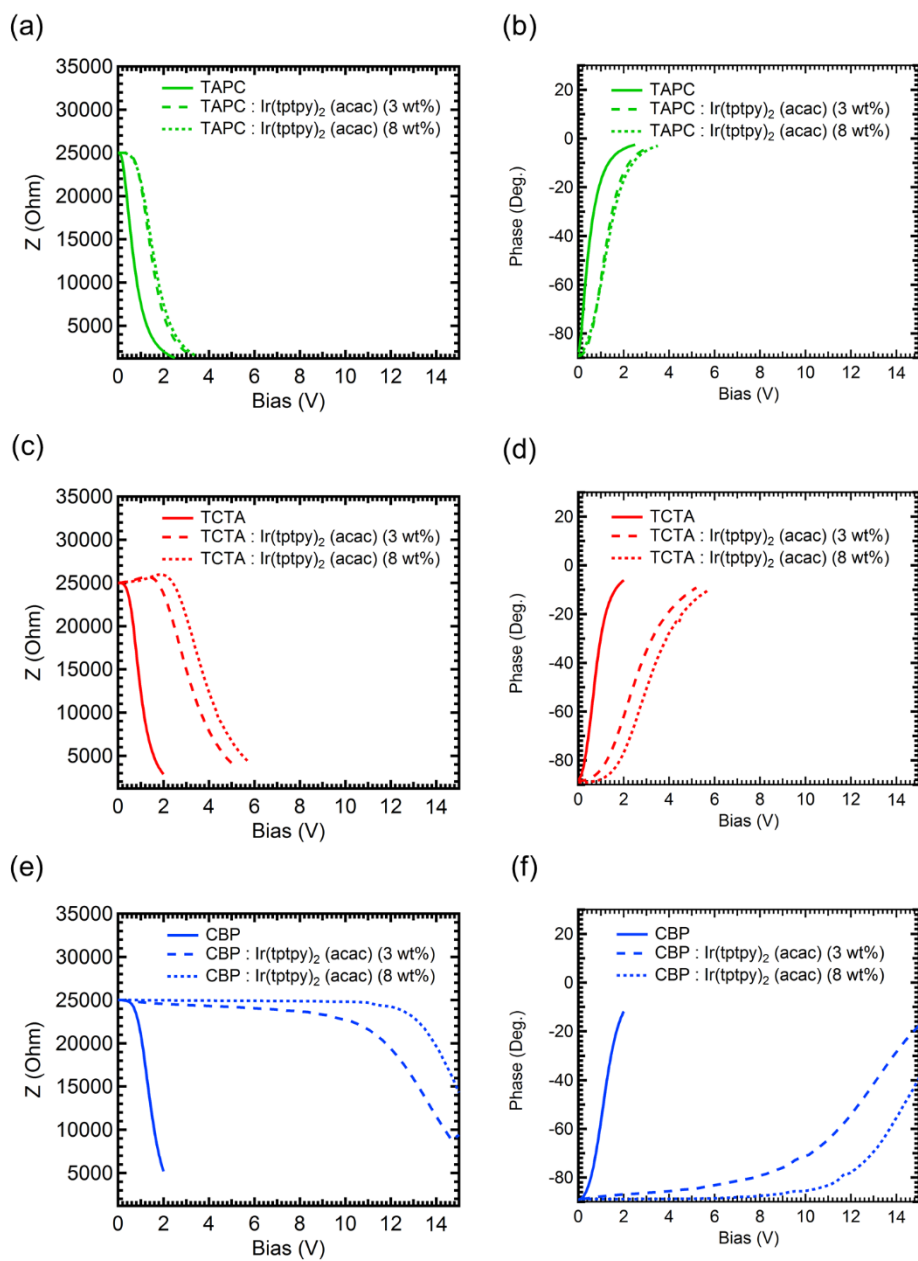


Figure 3.11 (a) Impedance versus voltage and (b) phase versus voltage characteristics of the hole-only devices with pristine and different doping concentrations of $\text{Ir}(\text{tptpy})_2(\text{acac})$ -doped (a), (b) TAPC, (c), (d) TCTA and (e), (f) CBP.

3.6 Improvement of Color Gamut Using A Red and Green Common Layer

As discussed in detail above, the structure using the YCL can reduce the EML patterning step efficiently when an appropriate HTL host material has been chosen. However, its drawback is a poor color gamut from the yellow sub-pixel because the yellow emission spectrum of the OLED dopant is narrower than that of inorganic materials. To achieve a broad CIE region and enhance the color gamut, we adopted a red and green double layer as a red and green-common layer (RG-CL) instead of a yellow common layer (Figure 3.11). Moreover, for the deep blue color coordinate, we selected 4,4'-bis(9-ethyl-3-carbazovinylyene)-1,1'-biphenyl (BCzVBi) as a deeper blue dopant than Firpic. As a result, in Figure 3.12 ©, 2 peaks of the red and green emissions can be achieved, and deeper green and red light after transmitted CFs was obtained compared to the single peak of the yellow emission displayed in Figure 3.12 (a). In addition, the CIE region of the device with the RG-CL becomes broader than that with the YCL (Figure 3.12 (b) and (d)). The CIE coordinates of the RGB sub-pixel of the device with the YCL are (0.658, 0.3417), (0.3988, 0.5964) and (0.1572, 0.128), respectively. For comparison, those of the device with the RG-CL are (0.655, 0.3447), (0.2669, 0.6629) and (0.1571, 0.1281), respectively. Without deteriorating blue emission, the device using the RG-CL can obtain purer red and green light than the YCL and improve the color gamut of the display.

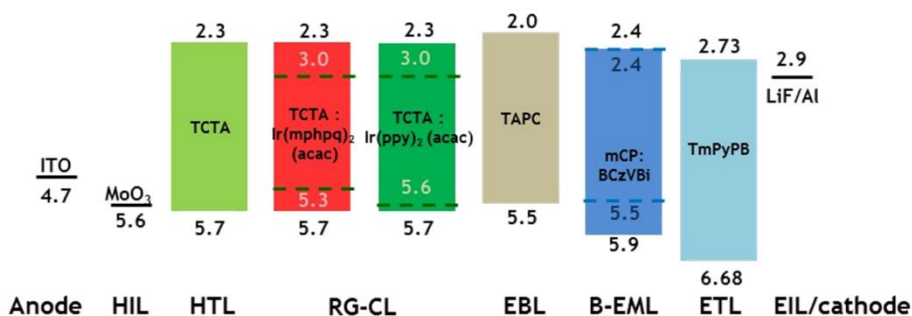


Figure 3.12 The device structures of the blue OLED with RG-CL.

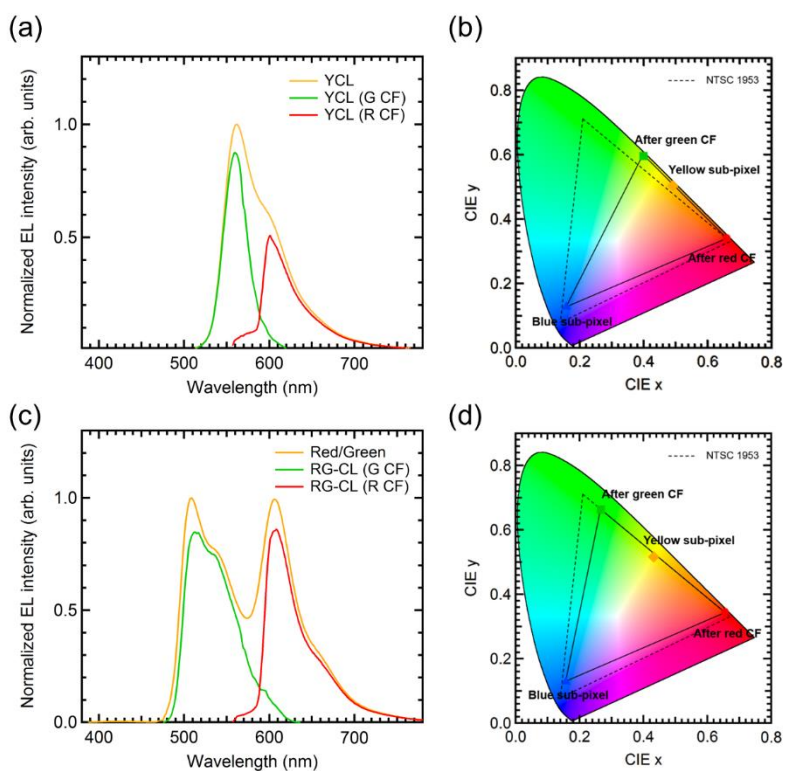


Figure 3.13 EL spectra and of the yellow device with (a) the YCL and (c) RG-CL, and (b), (d) their CIE color coordinates.

3.7 Stability of The Blue Devices with The YCL

To commercialize the Y/B OLED structures using the YCL, the stability of the devices should be investigated. By changing HTL materials, we observed the lifetime characteristics of the blue devices with the YCL (3 wt%, 8 wt%) and without the YCL at initial luminance 500 cd/m^2 as shown in Figure 3.14. As a result, in the devices using TAPC and TCTA, the blue devices without the YCL shows longer lifetime than the devices with YCL (3 wt%, 8 wt%). In both HTL materials, the devices using 3 wt% YCL has longer lifetime than the devices using 8 wt% YCL. In spite of shorter lifetime, the device with low doping ratio of the yellow dopant shows almost similar lifetime compared to the device without the YCL in TCTA. This indicates that the trap effect of the yellow dopant could affect to the device stability. However, the devices using CBP exhibits different trend of lifetime characteristics. The device with 8 wt% YCL has longer lifetime than the device without the YCL, indicating that further study is necessary for unveiling the YCL effect in the stability.

Moreover, we examined the influence of the EBL on the stability of the blue sub-pixels with TCTA. The Figure 3.15 displayed the device lifetime characteristics and the measurement carried out at initial luminance 500 cd/m^2 . As a result, the device with EBL has slightly shorter lifetime than that without EBL. T_{70} (The lifetime at 70% of initial luminance) of the device with EBL was 0.78 hours, whereas that of the device without EBL was 0.96 hours. The change of the driving voltage of the device with EBL was larger than that without EBL. This speculate that the accumulated charges at the interface of EBL could act as quenching sites or generate non-radiative excitons, resulting in the degradation of the interface of the device with EBL.

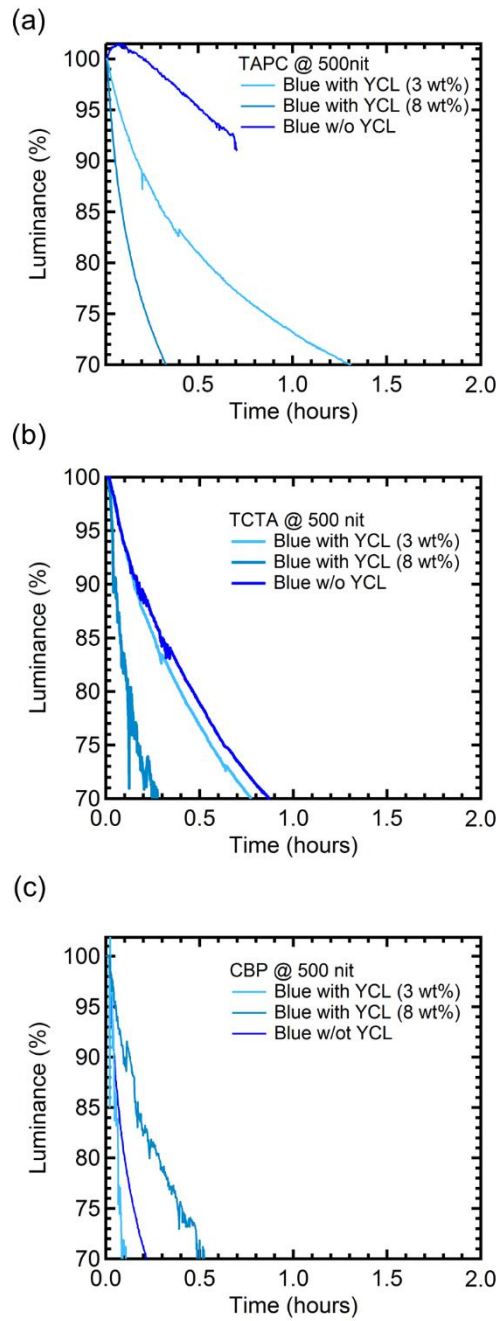


Figure 3.14 Luminance-time characteristics of the blue sub-pixel with YCL and without YCL of (a) TAPC, (b) TCTA and (c) CBP.

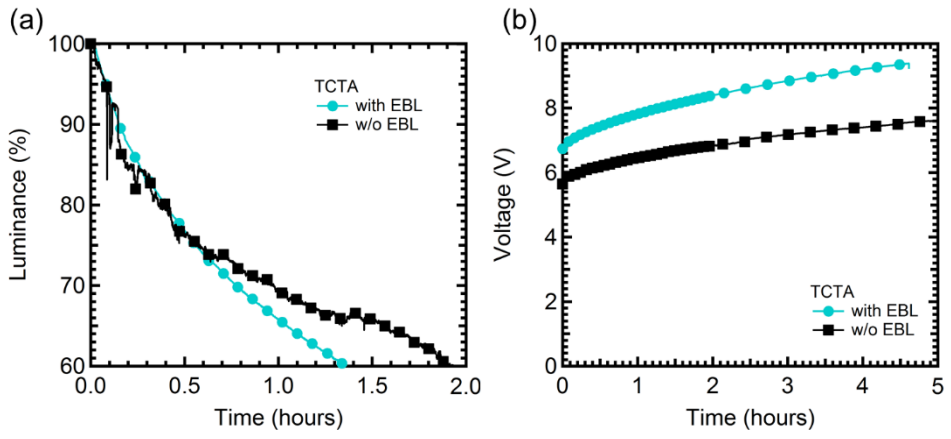


Figure 3.15 (a) Luminance-time and (b) voltage—time characteristics of the blue sub-pixel with EBL and without EBL of TCTA

3.8 Summary

In summary, we demonstrated a new OLED pixel structure using the YCL, and the device could be fabricated with a single FMM step for EML patterning without considerable degradation of the device performance. This pixel structure can achieve not only the advantages of a Y/B OLED such as a long lifetime and high resolution but also low-cost fabrication with a reduction in the number of FMM patterning steps. To maintain device performance, it is important to select an HTL material with a shallow difference between the HTL and yellow dopant HOMO energy levels and a small doping concentration of the yellow dopant. Furthermore, the HTL material must have a bipolar transport property to be an efficient host in a yellow device. Therefore, in this work, TCTA is the most appropriate HTL host material for use as the YCL. We therefore believe that this study can offer a new way to reduce fabrication costs and improve manufacturing yields in the display industry.

Chapter 4

Improved Out-Coupling Efficiency of OLED with D/M/D Electrode Using Thermally-Assisted, Self-Aggregated Silver Nanoparticles

Recently, the internal quantum efficiency of state of art OLEDs has reached almost 100 % by introducing new device structure and materials, such as energy level alignment of hole/electron transporting layer, utilizing singlet and triplet excitons simultaneously, ordering light emitting molecules and so on [82-85]. However, the waveguide mode in OLEDs hinders the extraction of light, thereby resulting in the low external quantum efficiency (EQE) [86-89]. Normally, the waveguide, entrapping

emitted light within a specific layer, is originated from total internal reflection at interfaces induced by the difference of refractive index (n) among a glass substrate ($n = \sim 1.5$), organic layers ($n = \sim 1.8$), and transparent electrodes [90].

To increase out-coupling efficiency of OLEDs, a semi-transparent electrode, such as dielectric/metal/dielectric (D/M/D), has been widely introduced to OLEDs. Replacing indium tin oxide (ITO) electrode to D/M/D structure, the out-coupling efficiency can be significantly enhanced as a result of the micro-cavity effect arose from the combination of semi-transparent and thick reflective metal electrodes [34, 91-93]. In addition, the incorporation of nano sized structures to OLEDs with D/M/D electrode has been introduced. The scattering effect of them, involving gratings [34], metallic nanoparticles (NPs) [38-41], buckled substrates [36-38] and so on, have led to escape entrapped light in glass or specific interfacial layer. When the waveguided light reaches them, they changed its penetration direction, resulting in escaping entrapped photons [34, 41]. Moreover, randomly sized and distributed structures without any periodicity allows us to compensate strong wavelength dependence of micro-cavity based devices [36, 37, 40, 41]. Especially, the size and shape control of silver NPs provides customized light extraction at the emission peak of OLED [52-54]. Despite excellent optical properties of nano structures, their application to OLEDs is still limited due to their complicated process and/or non-uniformity. In the case of widely using photo-lithography, the combination of precise mask and high energy light source with multiple process steps are required, which is bottleneck toward low-cost upscaling. Additionally, the periodicity from the mask pattern during a photo-lithography provokes the strong wavelength and angular dependence of devices. Although solution processed NPs or nano imprinting method fits for demonstrating randomly distributed films with low cost [52-56], its size limitation impedes the incorporation of them to real devices, arising from the inherent disadvantage of wet

process. Considering aforementioned concerns for utilizing out-coupling structure, NPs fabricated by easy and simple method, suitable for large area, are much beneficial for practical application of them to optoelectronic devices with D/M/D electrode, leading to enhanced EQE of OLEDs.

Herein, we address a new simple yet effective method of fabricating NPs and embedding them to OLEDs with D/M/D electrode, which is compatible with conventional process. The key feature of this strategy is to insert thermal assisted, self-aggregated Ag nanoparticles (TSA-Ag NPs), which does not require costly patterning and complicated molding process, into dielectric layer of D/M/D structure. Especially, these NPs were fabricated by the thermal annealing of vacuum deposited thin Ag film (450 °C/ 20 minutes) in ambient air without any photo-lithography processes, so that randomly sized NPs distributed in large area substrate can be simply obtained. The empirical and calculated results showed that TSA-Ag NPs provide the plasmonic effect of light at broad range, which enables to extract entrapped light in the substrate and thin film.

4.1 Fabrication of OLED of D/M/D Transparent Electrode with TSA-Ag NPs

Figure 4.1 represents the fabricating procedure of OLED with stochastic TSA-Ag NPs covered by low index polymer (LIP). For the generation of randomly distributed Ag NPs, the thin Ag layer (1 nm) was deposited on the UV-ozone cleaned glass by thermal evaporation method in high vacuum chamber ($< 5 \times 10^{-6}$ Torr). Afterwards, the layer was heated at 450 °C in a furnace for 20 minutes. Since the surface energy between Ag and glass is higher than interaction among neighboring Ag atoms, they aggregated each other as the assistance of given thermal energy and eventually changed their status from thin film to NPs (60-120 nm) [94, 95]. Then, the glass with TSA-Ag NPs was fully covered by 200 nm of commercialized LIP, Ormoclear, (Micro resist technology GmbH) by spin-coating to prevent the device from exciton quenching induced by non-encapsulated metallic NPs [96, 97]. We carefully choose the polymer as a dielectric of D/M/D electrode, because of its transparency at visible wavelength and refractive index (1.5), close to that of glass. After the LIP was irradiated under UV and annealed at 150 °C, a firm and flat dielectric film was obtained. On the top of LIP, thin Ag (15 nm) and 30 nm of MoOx doped TAPC (1:0.2 volume ratio) were sequentially deposited. The combination of commercialized LIP/thin silver/MoOx doped TAPC (D/M/D) worked as a semi-transparent electrode. After then, 20 nm of TAPC working as a hole transporting layer (HTL) and 30 nm of emissive layer, comprised of 8 wt% Ir(ppy)₃ doped with CBP, were casted on the electrode. The device was finalized with 40 nm of TPBi and 100 nm of Al cathode for electron transporting (ETL) and injection, respectively. All process was done under high vacuum chamber ($< 5 \times 10^{-6}$ Torr.). Here, all materials were used as purchased without

any further purification. The active area of the devices was 1.4×1.4 mm. For investigating the effect of TSA-Ag NPs, a device without them also fabricated.

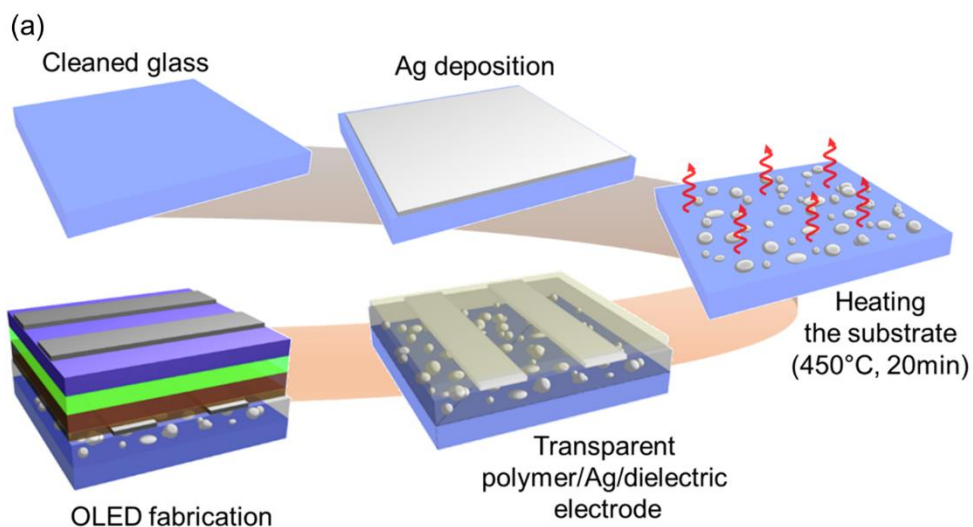


Figure 4.1 Process schematic diagram for OLED with TSA-Ag NPs. Here, the NPs were generated by thermal annealing of vacuum deposited silver layer (1 nm) without using any solution or complicated photo lithography process. In the device, the TSA-Ag NPs were located under transparent D/M/D electrode.

4.2 Generation and Surface Morphology TSA-Ag NPs

Figure 4.2 illustrates the morphology of silver layers depending on annealing temperature, measured by scanning electron microscopy (SEM, MERLIN compact, Carl zeiss AG). In as-deposited 1 nm of silver layer, the surface of glass was evenly covered by it. An atomic force microscopy (AFM) image also indicates that this film was very flat with small variation (Figure 4.4). On the other hand, the silver in film tended to aggregate each other, as the temperature of substrate was sufficiently high to overcome the interfacial energy between Ag and glass [94, 95, 98]. When the substrate temperature had been elevated to 250 °C for 20 minutes, the status of Ag layer turned into a mixture of two different phases: i) large sized metallic clusters (50 - 100 nm) by assemble neighboring silver layer and ii) maintaining thin film status attached to the glass. At the higher temperature annealing (450 °C for 20 minutes), the silver layer totally changed into randomly distributed NPs with the diameter of 74 ± 19 nm (Please see Figure 4.3). We carefully choose 450 °C as an annealing temperature, because it is lower than that of widely using process of driving circuit of commercial OLEDs [99, 100]. Thus, TSA-Ag NPs can be generated during the annealing process of silicon or oxide materials for transistor.

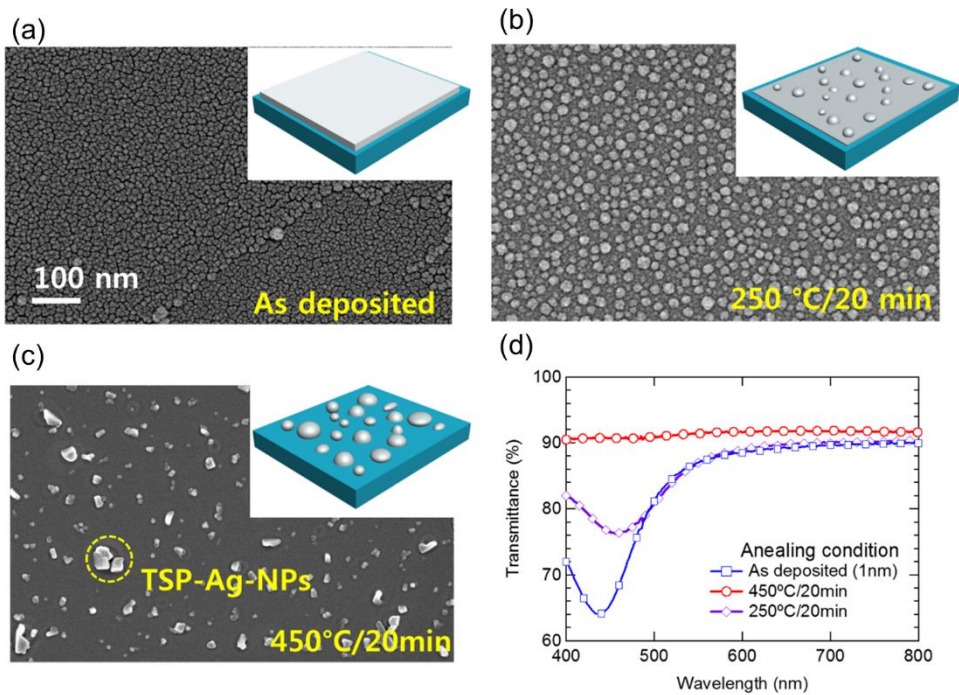


Figure 4.2 SEM images of Ag layer (1 nm) depending on the annealing process temperature: (a) as-deposited, (b) annealed 250 °C and (c) annealed 450 °C. As substrate was heated, Ag aggregated each other and eventually changed its phase to large sized clusters (50-100 nm) (d) Transmittance spectra of glass/silver layers/low index polymer before and after annealing.

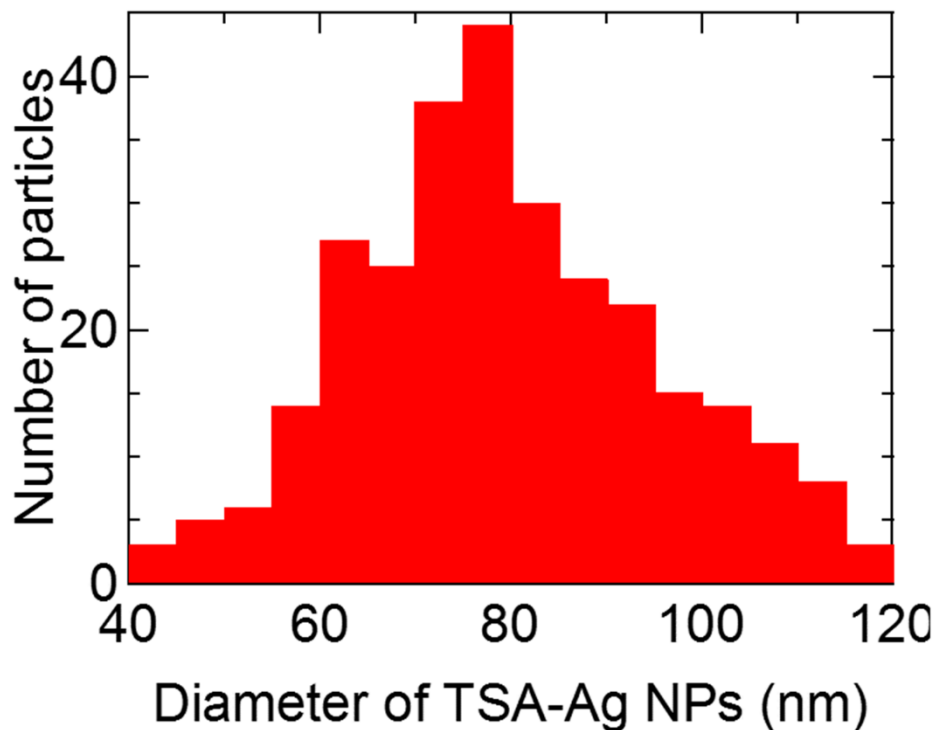


Figure 4.3 Size distribution of TSA-Ag NPs (74 ± 19 nm) derived from the SEM image. The size distribution was determined by software (Image J) in $5 \times 5 \mu\text{m}^2$ area.

The surface of an as-deposited silver film (1 nm), shown in Figure 4.4 (a), was flat with small variation. The root mean square of height (δRMS) was less than 1 nm. Consistent to the SEM image, any large sized NPs were not observed in the as-deposited case. On the other hand, as the film was annealed at high temperature (450°C for 20 nm), silver began to aggregate and transformed its phase to nano particles, as illustrated in Figure 4.4 (b) Nano clusters of Ag, remarked as white dots in image, were exhibited in AFM image. The height of this aggregation of Ag was 60 nm, similar to the average size of TSA-Ag NPs obtained by SEM image (74 ± 19 nm).

Therefore, AFM images of silver layers also clearly remark that the substrate heating led to transformation of silver layer's phase without any complicated process.

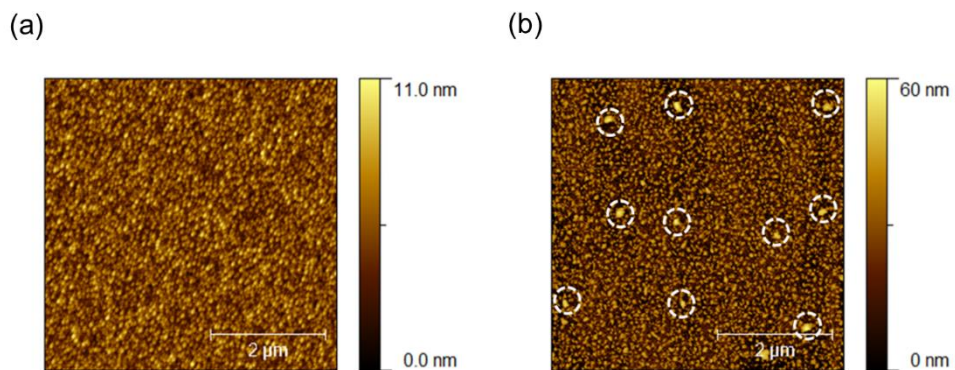


Figure 4.4 Atomic force microscopy (AFM) image of Ag layer on cleaned glass.

4.3 Optical Properties of TSA-Ag NPs

In this film, the strong absorption of light at 420 nm was observed in the glass/As-deposited Ag/LIP, consistent to previous results of ultrathin silver film on dielectric layer [101, 102]. Most of photons (blue and green light) are vanished rather scattered in this film, so that it would not be inappropriate for full color OLEDs. As a result of changed surface morphology, the absorption at 420 nm decreased and the absorption peak was shifted to the longer wavelength, indicating a formation of enlarged NPs. However, remaining silver film still absorbed light in the range of 400 - 550 nm, which could decrease the performance of OLED. However, further modification of silver layer deposition and annealing process enables us to obtain specific sized NPs, which might boost more light extraction efficiency [103]. In accordance with SEM image, the transmittance of TSP-Ag NPs on the glass was similar to that of a bare glass as a result of decreased light absorption of large sized metallic NPs (see Figure 4.2 (d)). It means the emitted light of OLEDs is barely absorbed by TSP-Ag NPs, which would not mitigate the EQE of devices. Here, we would like to stress that TSA-Ag NPs were generated by a self-assembly arose from strong de-wetting property of silver on glass, not using a complicated photolithography. Moreover, they were realized by a dry process based on vacuum deposition, which allows one to upscale the size of attainable NP incorporated substrate.

The empirically and theoretically analysis revealed that TSA-Ag NPs provide the plasmonic effect in broad range of visible light. Figure 4.5 (a) exhibits a dark field microscopy (BX51, Olympus) image of TSA-Ag NPs covered by the LIP on the Si/SiO₂ substrate. The microscopy exclusively detects scattered light from a specimen, while directly reflected and/or transmitted light misses the lens [104]. In the case of TSA-Ag NPs implemented substrate, scattered light nearby NPs were

apparently observed, which reveals that TSA-Ag NPs works as plasmonic sources. In contrast, no plasmonic effect was observed in the case without NPs (See the Figure 4.5 (b)), which specifies that they are only sources for changing the trajectory of photon in this structure. Before coating the LIP on the Si wafer, the substrate was cleaned by ultrasonic with acetone, isopropyl alcohol and DI water. Moreover, the substrate was also annealed 450 °C for 20 minute to analyze the plasmonic effect of this substrate under same condition of TSA-Ag NPs incorporated one. Then, the substrate was investigated by dark field microscopy. Here, the light source for evaluating plasmonic effect is xenon lamp. As shown in Figure 4.5 (b), only black image was observed in LIP deposited on SiO₂/Si wafer, reflecting that there was no plasmonic effect. Compared to the result with TSA-Ag NPs, this image reveals that TSA-Ag NPs only provided the plasmonic effect of light in the device. Intriguingly, the color of scattered light induced by them varied among visible light, from blue to red. It represents that randomly sized TSA-Ag NPs broadly scattered visible light and can contribute to the enhancement in the light extraction of entire visible light emitting devices. The further benefit of installing TSA-Ag NPs to OLEDs is to mitigate the strong wavelength dependence induced by micro-cavity structure.

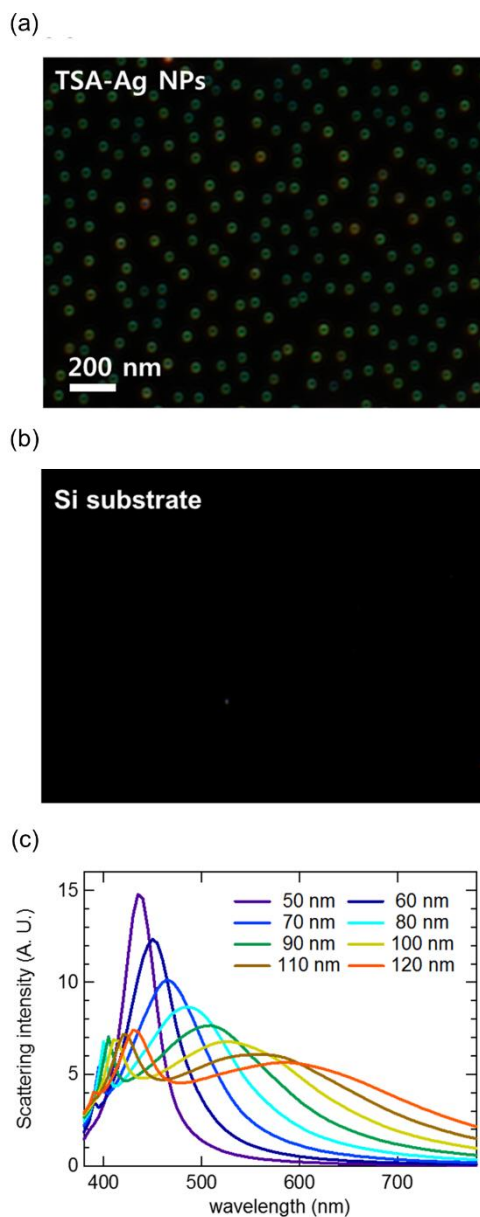


Figure 4.5 (a) Dark field microscopy image of TSA-Ag NPs incorporated LIP on the SiO₂/Si wafer. The variety of color in dark field microscopy image represented that stochastic TSA-Ag NPs provided plasmonic effect in broad range of visible light. (b) That of low index polymer (LIP) (200 nm) deposited on SiO₂ (100nm)/Si wafer. (c) Calculated plasmonic effect intensity of different sized Ag NPs (50-120 nm) in LIP based on FDTD simulation.

Moreover, the plasmonic effect of TSA-Ag NPs was quantitatively calculated using finite difference time domain (FDTD) simulation. Here, it is assumed that NPs were perfect spherical structures for the simplicity of calculation and their diameter varied from 50 to 120 nm, considering aforementioned SEM image. As the size of NPs is enlarged, the peak of spectrum is red-shifted (See Figure 4.5 (c)). In the case of small sized NPs (< 50 nm), NPs mainly scattered blue light (< 420 nm). In contrast, the peak of their plasmonic effect was shifted to the green (520 nm) and red (600nm), as their diameters were enlarged to 90 and 120 nm, respectively. Since TSA-Ag NPs were the combination of these various sized NPs, which have barely utilized by photolithography and/or mono-dispersed solution NPs, they could lead to improved performance of OLEDs independent on its peak color arose from their broad plasmonic effect.

4.4 Optical Simulation of OLED with TSA-Ag NPs

To analyze the optical effect of TSA-Ag NPs at the device structure, the electrical (E) field distribution was simulated by FDTD method. The detailed procedure is discussed in supplementary data. The theoretical calculation points out that only TSA-Ag NPs worked as plasmonic centers at this structure, as shown in Figure 4.6 (a). Nearby the NPs, significant enhancement in E-field was observed. Besides, TSA-Ag NPs promoted the E-field in broad range, both 500 and 550 nm light, in a good agreement with the device result. On the other hand, there was no plasmonic effect at the LIP and glass side in the case without TSA-Ag NPs (Figure 4.6). By incorporating the E-field distribution from 500 to 550 nm, the theoretical E-field enhancement ratio (17%) induced by insertion of TSA-AG NP can be successfully derived, which is close to the empirically achieved value (~11%) (Please see Figure 4.7). Consequently, the simulation analysis at the device structure indicates that TSA-Ag NPs provides plasmonic effect at the OLED in broad range, contributing to improvement in out-coupling efficiency of device.

For quantitative analysis of plasmonic effect of stochastic TSA-Ag NPs, the finite difference time domain (FDTD) simulation of them was conducted using a commercial software (FDTD solution, Lumerical Inc.). Here, the n, k values of each material except silver and aluminum were measured using ellipsometer, while the values of metal were obtained from previous work [105]. In the FDTD simulation for device, we set the emission of organic layer to total field scatter field (TFSF) light source, propagating in z -direction with TE polarization (or horizontal polarization). In the boundary, perfectly matched layer (PML) boundary conditions were applied to x -, y -axes and z -axis except Al electrode. In Al electrode side, metal boundary conditions were used. The plasmonic effect intensity was monitored by a total field

power monitor and a scattered field power monitor. Meanwhile, it was assumed that TSA-Ag NPs were perfect spheres and point contacted glass substrate. Moreover, the distance among dots was set from 200 to 500 nm, considering SEM result of them. Furthermore, the size of NPs was varied from 60 to 120 nm, regarding empirically derived average size and variation of them. Then dispersive refractive indices n,k value for LIP and each organic material were measured by an ellipsometer.

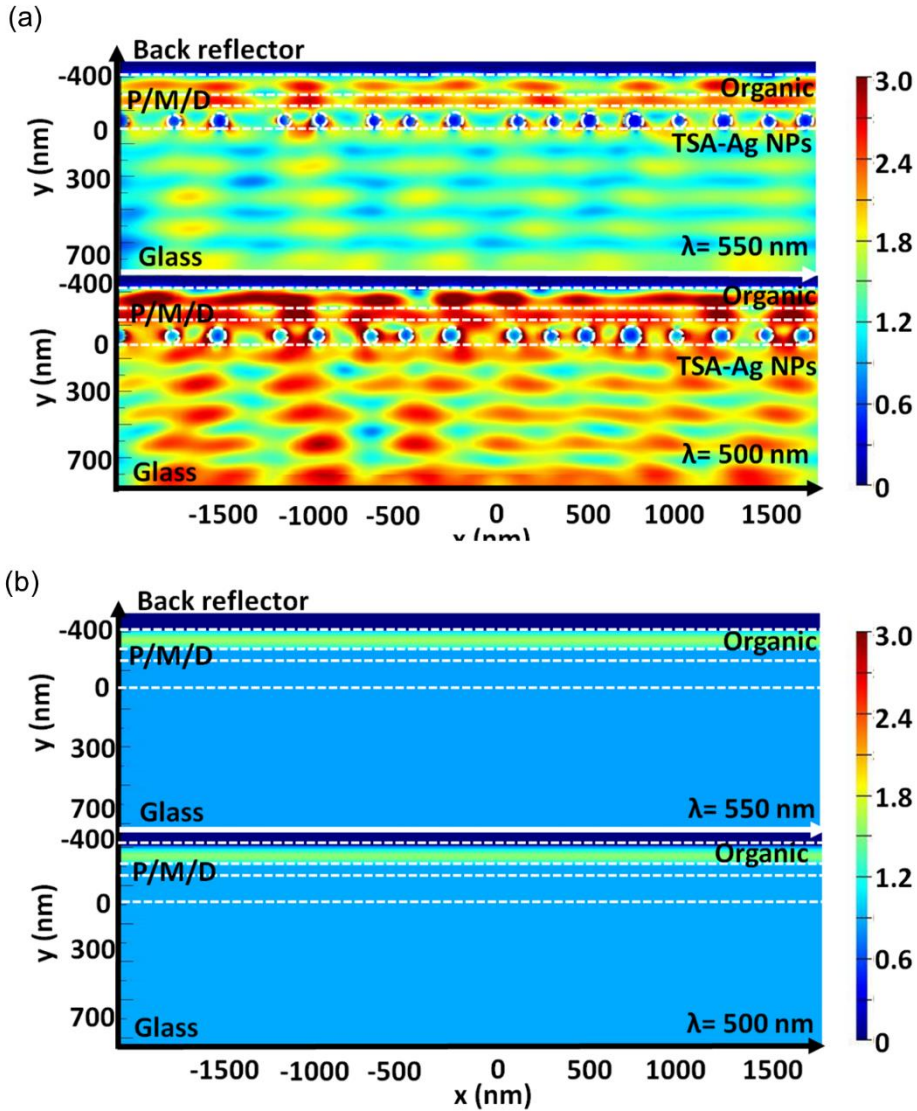


Figure 4.6 Calculated E-field distribution at the OLED employing D/M/D electrode (a) with and (b) without TSA-Ag NPs under 500 and 550 nm light, respectively. The plasmonic effect induced by NPs themselves as well as the interaction between thin Ag in D/M/D and TSA-Ag NPs were exhibited. In contrast, no light enhancement was observed in the case of without them. These figures clearly point out that the installment of TSA-Ag NPs to device enables to scatter light at the device structure.

To estimate theoretically derived E-field enhancement induced by installing TSA-Ag NPs to OLED, the E-field of device with and without TSA-Ag NPs was calculated at the emission spectrum of device. After then, the enhancement ratio of EL intensity was determined by dividing the result of OLED with TSA-Ag NPs by one without them. Moreover, the empirical enhancement ratio was obtained following the same procedure. Figure 4.7 is theoretical and enhancement ratio as a function wavelength, which is very close to each other. As presented in Figure 4.5 (c), small sized TSA-Ag NPs ($d < 100$ nm) mainly scatter the light around 500 nm, while large sized NPs ($d > 120$ nm) offer plasmonic effect at longer wavelength. Owing to the size distribution of TSA-Ag NPs (74 ± 19 nm), the calculated E-field enhancement ratio exhibits its maximum at 500 nm and decreased at longer wavelength. The small discrepancy between simulation and device result might be originated from the assumption of simulation for the simplicity of calculation; the size of NP is not randomly distributed, but a combination of four different sizes (diameter of 60, 75, 90, and 105 nm, considering the distribution of size obtained in Figure 4.3.) Regarding the emissive intensity of device without OLED, the theoretically expected enhancement in E-field is 17% at emission spectrum, which is consistent to the empirical data

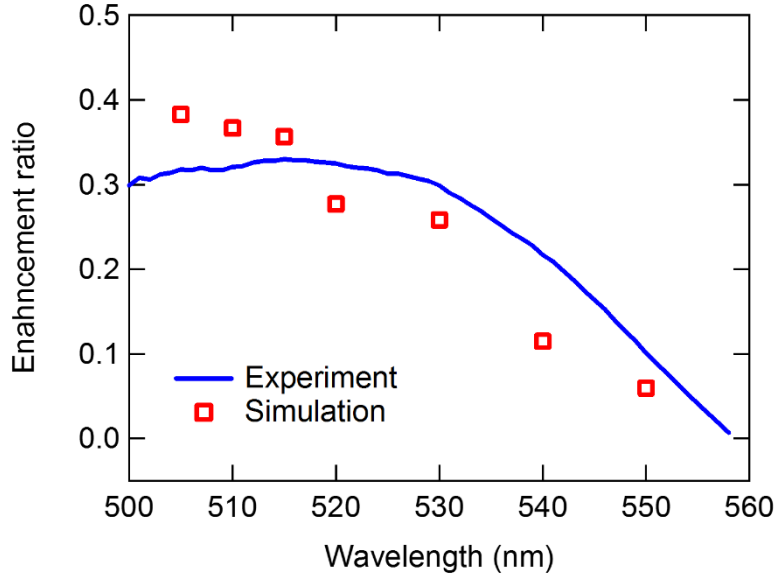


Figure 4.7 The empirical and simulated enhancement ratio of out-coupled light intensity of OLED with NPs, compared to the case without them. Here, the empirical and theoretical enhancement ratio was derived by dividing the result of OLED with TSA-Ag NPs by one without them at each wavelength.

4.5 Device Performance of OLEDs with TSA-Ag NPs

Regarding optical properties of TSA-Ag NPs, we explored their effect on the green phosphorescent OLEDs based on Ir(ppy)₃ doped with CBP. Figure 4.8 (a) shows current density (J)-voltage (V)-luminance (L) characteristics of OLEDs incorporating D/M/D electrode with and without TSA-Ag NPs. And these were compared to the OLED employing ITO electrode. The turn-on voltage of all samples was about 2.7 V, regardless the installation of D/M/D electrode and TSA-Ag NPs. Moreover, current density of all devices under low electric field (0 - 2 V) was in the same range, indicating that the leakage current arose from the metallic NPs (50-120 nm), fully covered by 200 nm of LIP, was negligible [96-98]. On the other hand, the luminance of D/M/D incorporated device (562 cd/m²) was almost twice higher than that of OLED with ITO electrode (306 cd/m²) at the current density of 1 mA/cm², caused by the optical micro-cavity effect between semi-transparent and Al electrode [91, 92]. Furthermore, the additional 10% enhanced luminance (632 cd/m²) was obtained in the device with TSA-Ag NPs employed D/M/D at the same current density. Consistent to J-V-L curve, the EQE of device with TSA-Ag NPs incorporated D/M/D also showed superior performance in comparison with other two cases (see Figure 4.8 (b)). For instance, the EQE of our proposed structure, regarding angular dependence of each device, was 25.1%, which is 11% higher than that of device with only D/M/D layer (22.7%), where the luminance was 500 cd/m² (Please see Figure 4.9, Table 4.1).

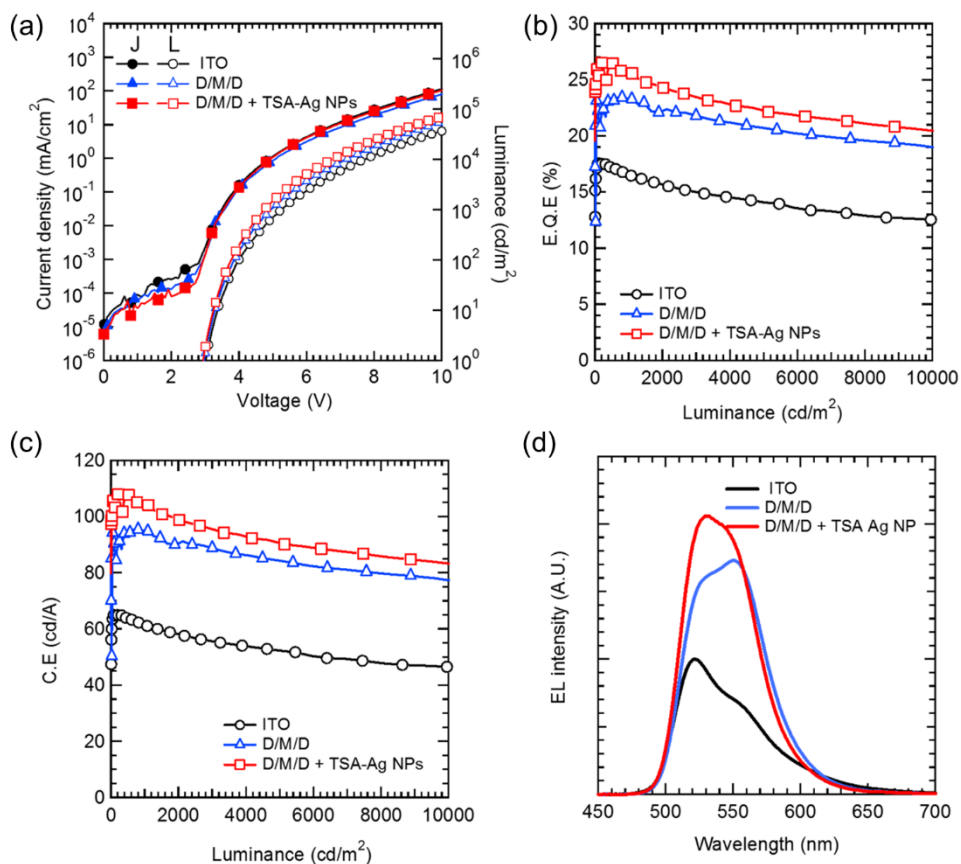


Figure 4.8 Performance of OLEDs employing D/M/D electrode with and without TSA-Ag NPs:(a) Current density-voltage-luminance (J-V-L), (b) External quantum efficiency (EQE)-luminance considering angular dependence and (c) luminance-current efficiency characteristics. For the comparison, optoelectronic properties of device with ITO electrode were also included each graph. The graphs directly show that the implementation of TSA-Ag NPs to micro-cavity based OLED leads to additional improvement in the efficiency of device. (d) EL spectra of the OLEDs, reflecting that TSA-Ag NPs provide the enhancement in out-coupling efficiency in broad range.

Table 4.1 Device performance of OLEDs with D/M/D including TSA-Ag NPs.

Electrode	NPs	Turn-on voltage [V]	Current density [mA/cm ²] @ 6 V	EQE [%] @ 500 cd/m ²	CE [cd/A] @ 500 cd/m ²
ITO	X	2.7	4.4	17.4	64.3
D/M/D	X	2.7	4.3	22.8	94.4
D/M/D	O	2.8	4.4	25.1	108.0

Although the EQE of devices slightly decreased at higher current density, the enhancement ratio OLEDs with TSA-Ag NPs to without case was maintained more than 10% up to 10,000 cd/m². Additionally, current efficiency (CE) versus luminance characteristics of devices, as illustrated in Figure 4.8 (c), elucidated that installation of TSA-Ag NPs boosted the CE (108.0 cd/A) by 14.8% compared to case without them (94.5 cd/A) at 500 cd/m². As aforementioned, the effect of TSA-Ag NPs, perfectly covered by 200 nm of LIP, on electrical properties of OLED was so small that the enhancement ratio of CE is thus analogous to that of EQE. Furthermore, the installation of TSA Ag NPs to OLED with different micro-cavity structure still contributes to the improved EL intensity, as displayed in Figure 4.10. For achieving more enhanced device performance employing TSA-Ag NPs, we tried to increase the density of NPs by generating them from the thick film (2 nm of Ag). Nevertheless, the performance of OLED with TSA-Ag NPs originated from by thick film was inferior to that of case transformed from 1 nm film because of decreased transparency of TSA-Ag NPs (Figure 4.10).

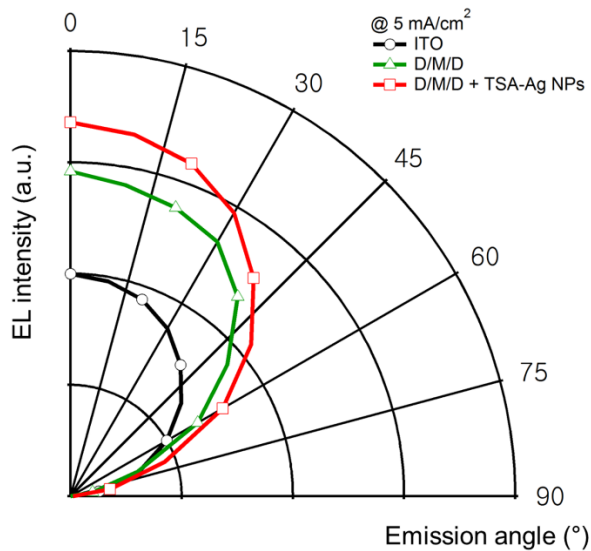


Figure 4.9 The angular dependence of EL intensity of OLEDs with various structures at 5 mA/cm^2 . Differ from results of periodic nano structure, the EL intensity of OLED with TSA-Ag NPs is broadly enhanced compared to the case without them. The EQE of device, shown in Fig 4(b), was calculated considering the angular dependence of device.

Here, TSA-Ag NPs of both cases were derived from 1 and 2 nm of silver films, respectively. The efficiency of devices installing TSA-Ag NPs from 2 nm of silver layer was lower than that of device incorporating metallic nano clusters formed by 1 nm Ag NPs. The C.E (98 cd/A) and EQE (23.8%) of device including TSA-Ag NPs from 2 nm Ag layer decreased in comparison with the optimized device (108 cd/A and 25.2%, respectively) at 500 cd/m^2 . We believe that the diminished performance was attributed to the strong absorption of EL by TSA-Ag NPs made from 2 nm of layer. As shown in Figure 4.10 (c), the transmittance of TSA-Ag NPs from 2 nm was lower than that of optimized NPs in the EL spectra of emitter. Particularly, in high energy light, its transmittance is below 60%. Since the amount of silver in this film is larger than that of optimized case, some of NPs might not aggregate each other and maintain its phase, where photons are vanished. The overlapped absorption spectrum between

these NPs and 1 nm of as-deposited film (Figure 4.2 (a)) is supportive evidence that un-aggregated, residual silver layer absorbed the light in this region. As a result of this low transmittance of TSA-Ag NPs from 2 nm silver layer, the out-coupling spectra of OLED with them eventually diminished, shown in Figure 4.10 (d). Interestingly, the decreased out-coupling spectra was in the same range of the absorption of these TSA-Ag NPs. Hence, the absorption of emitted light by TSA-Ag NPs from thick film mitigate the enhanced out-coupling efficiency of device with them arose from plasmonic effect. If fabrication method of TSA-Ag NPs is further modified, additional improvement in OLED performance will be achieved.

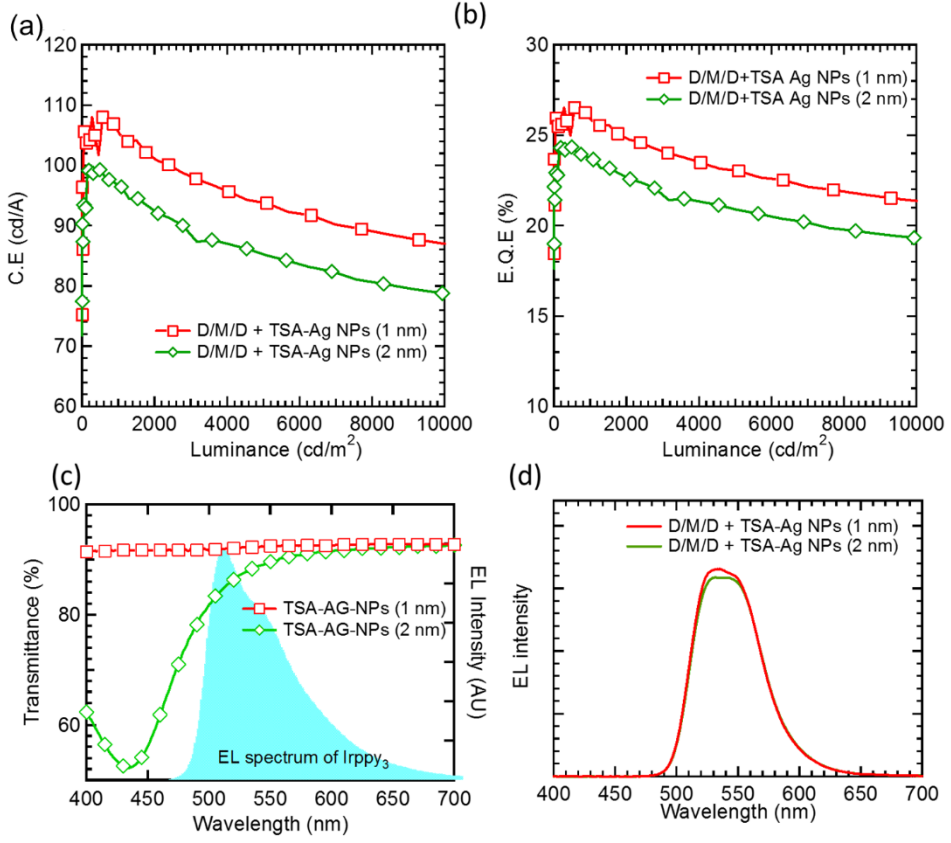


Figure 4.10 (a) Current efficiency (C.E)–luminance and (b) external quantum efficiency (EQE)–luminance characteristics, (c) the transmittance, and (d) EL intensity of OLEDs employing D/M/D electrode with TSA-Ag NPs.

4.6 Mitigation of Wavelength Dependence of OLED with D/M/D Structure by Using TSA-Ag NPs

Meanwhile, our proposed structure using D/M/D with TSA-Ag NPs brought a broadly enhanced electroluminescent (EL) spectrum of device (see Figure 4.8 (d)). In the case of OLED with only D/M/D, the EL peak (550 nm) was red-shifted compared to that of one with ITO (510 nm) as a result of strong wavelength dependence of micro-cavity structure. In contrast, the incorporation of TSA-Ag NPs did not only increase EL intensity at the peak of emission layer (510 nm), but also improved it at the resonance peak between semi-transparent and thick reflective electrode (550 nm). As equivalent to empirical and theoretical prediction (Figure 4.5 (c)), the plasmonic effect from randomly sized TSA-Ag NPs universally boosted the device performance of OLED. Thus, the possible advantage of TSA-Ag NPs to capitalize is to mitigate wavelength dependence of OLED with micro-cavity effect.

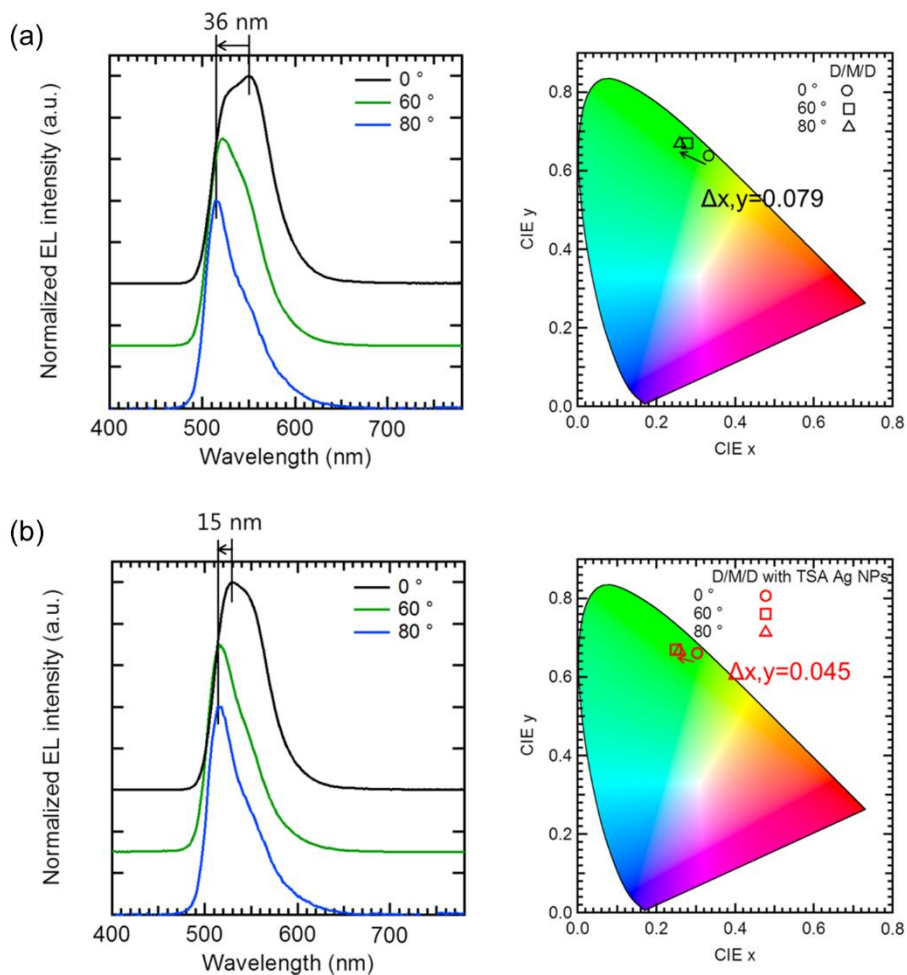


Figure 4.11 EL spectra of micro cavity OLED (a) without and (b) with TSA-Ag NPs and their corresponding CIE 1931 color space chromaticity diagram at different angles. Here, the $\Delta x, y$ is the change of color coordination of emissive light at normal and 80° degree.

Moreover, Angular dependence of EL spectra of each device clearly indicates that TSA-Ag NPs suppress strong angular dependence of OLED with D/M/D electrode (Please see Figure 4.11). Owing to the micro-cavity effect, the changes of EL spectra have usually shown in D/M/D structures as a function of observation angle. Nonetheless, the device incorporating TSA-Ag NPs in this work remarkably

alleviated the problem of the EL spectra shifts because of the universal plasmonic effect of randomly shaped or distributed nanostructures [106, 107]. This feature is very difficult to achieve in periodically patterned nano structure [49, 108]. As displayed in Figure 4.11 (b), a change of CIE coordinate of the device incorporating TSA-Ag NPs (red marker, $\Delta x, y = 0.045$) at different emission angles, which is not noticeable with the naked eye, is also less perceptible than that of the device using only D/M/D structure (black marker, $\Delta x, y = 0.079$). Therefore, it is obvious that embedding TSA-Ag NPs to the OLED with semi-transparent electrode leads to the pronounced improvement in the performance at broad range without changing angular emission characteristics.

4.7 Uniformity of OLED with D/M/D Structure by Using TSA-Ag NPs

To figure out uniformity of this structure, we carefully re-examined the J-V curves of OLEDs from 5 different batches, as shown in Figure 4.12 (a). Here, blue lines are for the devices without NPs, whereas red lines are for the OLEDs with them. Even in the same experimental condition, the J-V curves vary from batch to batch due to manually processed system in our facilities. In some cases, the current of device without NPs is higher than that of device with them. On the other hand, the reverse case is also observed. However, the average operating voltage of each case is very close to the each other at 5 mA/cm². (Please see Figure 4.12 (b) and (c)). Therefore, we believe that the insertion of TSA-Ag NPs does not provoke any serious change in electrical properties of devices.

Among these data, we carefully chose the bold lines (Figure 4.12 (a)) and closed circles (Figure 4.12 (b)) for Figure 4.8 (a), because the EQE enhancement ratio of this batch (11.0%) is close to the average value (12.3%) derived from 5 different batches (6.8 – 17.9 %). By using the representative batch, we might avoid the over and/or under estimation of the effect of TSA-Ag NPs.

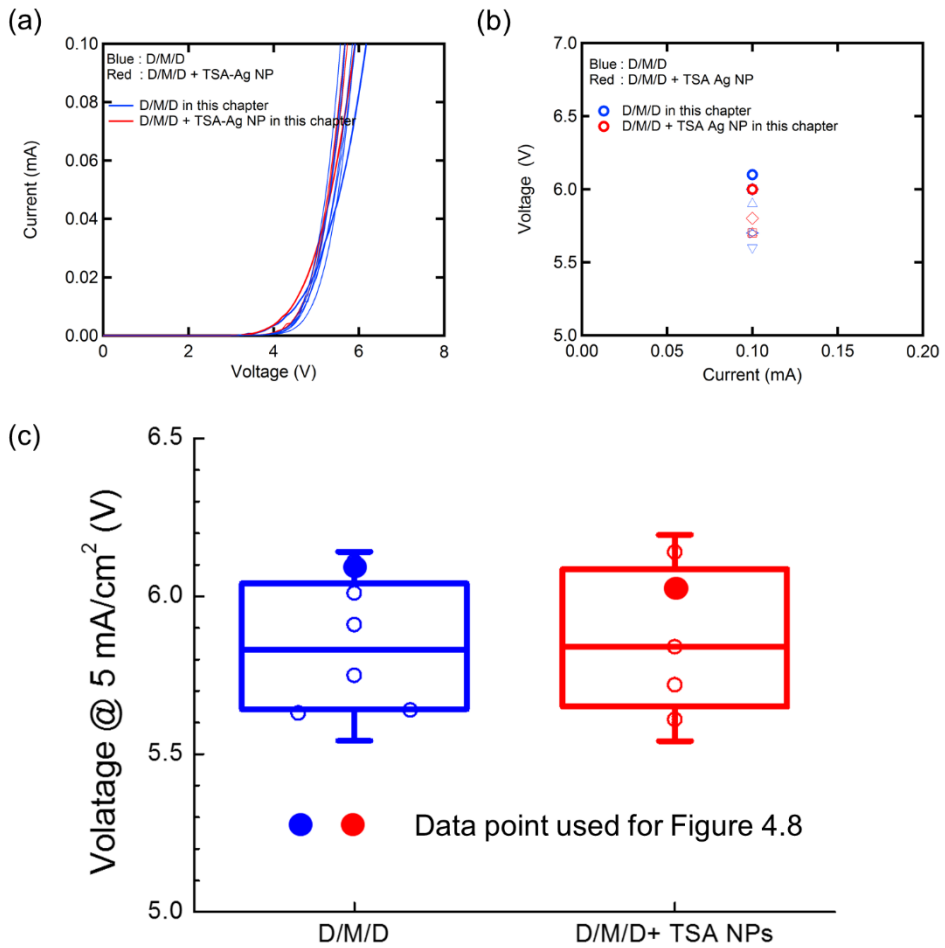


Figure 4.12 (a) J-V characteristics of OLED with (Red line) and without (Blue line) TSA-Ag NPs. (b), (c) Driving voltage of each device at 5mA/cm².

4.8 Summary

In summary, we demonstrated simple method to fabricate stochastic Ag NPs and the improvement in the device performance of micro-cavity based OLED by employing them. TSA-Ag NPs were generated by heating the thermally evaporated Ag film at 450 °C for 20 minutes without complicated process. The dark field microscopy and FDTD simulation denoted that randomly sized TSA-Ag NPs provided strong plasmonic effect in broad range. Moreover, these nano structures increased out-coupling efficiency by plasmonic waveguided light. As a result, the 11% enhancement in EQE of OLED was achieved by incorporating TSA-Ag NPs located in low index polymer, compared to the device without NPs. Moreover, the strong angular dependence of OLED with micro-cavity structure can be alleviated by these NPs. We thus believe that this study can open a new practical way to improve the performance of solid light sources.

Chapter 5

Conclusion

In this thesis, we demonstrate the OLED pixel design through single EML patterning step for low-cost fabrication. Moreover, for further improvement of the device performance, thermally-assisted, self-aggregated Ag NPs are adopted in OLED with D/M/D electrode.

First, we demonstrated the device design strategy for yellow/blue OLED with red and green CFs using a YCL. Employing the YCL removing yellow EML patterning instead of separate yellow and blue EML patterning, we could achieve simple fabrication process for full-color OLED display with single EML patterning compared to conventional red, green and blue FMM EML patterning method. With various commercialized HTL host materials such as TAPC, TCTA and CBP, we investigated factors to affect the device performance when we inserted the YCL. As a result, HTL host material, which has a high hole mobility, bipolar transport property

and little difference HOMO energy level between HTL and yellow dopant, should be used to maintain the device performance with insertion of the YCL. In addition, electron blocking layer, trap depth and trap density of yellow dopant is the one of the element to degrade the device performance such as color mixing, driving voltage and efficiency. To improve color gamut property of the yellow OLED with red and green CFs, we also adopted a red and green common layer with two separate red and green peak.

Second, by incorporating thermally-assisted, self-aggregated Ag NPs under the D/M/D electrode, we not only enhanced the out-coupling efficiency of the device but also mitigate the wavelength dependence of the device using D/M/D electrode. With thin Ag evaporation and annealing process, we fabricated the TSA-Ag NPs having random distribution and various size with high plasmonic effect efficiency. We confirmed plasmonic effect of the TSA-Ag NPs by using the dark field microscopy equipment. The generated TSA-Ag NPs were covered by low refractive index polymer for the planarization. We also simulated optical plasmonic effect of the device with D/M/D electrode using TSA-Ag NPs. By introducing this method, we achieved the EQE of 25.1% at 1000 cd/m² without any deterioration of electrical properties. In addition, owing to the random distribution and size of the TSA-Ag NPs, strong wavelength dependence of the device with D/M/D electrode was mitigated by inserting the TSA-Ag NPs.

In conclusion, this thesis proposes the practical and novel approaches to achieve simple and low-cost fabrication of full-color OLED display and improve the device performance. These methods can be easily adopted in the current display manufacturing process because fabrication process is compatible with current OLED fabrication process such as thermal evaporation and annealing process. These results

give a useful platform for further research toward low-cost and highly efficient OLED display fabrication in the display industry.

Bibliography

- [1] M. Pope, H. P. Kallmann, and P. Magnante, "Electroluminescence in Organic Crystals," *The Journal of Chemical Physics*, vol. 38, pp. 2042-2043, 1963.
- [2] N. Vityuk and V. Mikho, "ELECTROLUMINESCENCE OF ANTHRACENE EXCITED BY PI-SHAPED VOLTAGE PULSES," *SOVIET PHYSICS SEMICONDUCTORS-USSR*, vol. 6, pp. 1497-1499, 1973.
- [3] P. S. Vincett, W. A. Barlow, R. A. Hann, and G. G. Roberts, "Electrical conduction and low voltage blue electroluminescence in vacuum-deposited organic films," *Thin Solid Films*, vol. 94, pp. 171-183, 1982/08/13/ 1982.
- [4] R. H. Partridge, "Electroluminescence from polyvinylcarbazole films: 3. Electroluminescent devices," *Polymer*, vol. 24, pp. 748-754, 1983/06/01/ 1983.
- [5] C. W. Tang and S. A. VanSlyke, "Organic electroluminescent diodes," *Applied Physics Letters*, vol. 51, pp. 913-915, 1987.
- [6] C. W. Tang, S. A. VanSlyke, and C. H. Chen, "Electroluminescence of doped organic thin films," *Journal of Applied Physics*, vol. 65, pp. 3610-3616, 1989.
- [7] J. H. Burroughes, D. D. C. Bradley, A. R. Brown, R. N. Marks, K. Mackay, R. H. Friend, *et al.*, "Light-emitting diodes based on conjugated polymers," *Nature*, vol. 347, pp. 539-541, 10/11/print 1990.
- [8] J. Kido, K. Hongawa, K. Okuyama, and K. Nagai, "White light-emitting organic electroluminescent devices using the poly(N-vinylcarbazole) emitter layer doped with three fluorescent dyes," *Applied Physics Letters*, vol. 64, pp. 815-817, 1994.
- [9] M. A. Baldo, D. F. O'Brien, Y. You, A. Shoustikov, S. Sibley, M. E. Thompson, *et al.*, "Highly efficient phosphorescent emission from organic electroluminescent devices," *Nature*, vol. 395, pp. 151-154, 09/10/print 1998.
- [10] J. Kido, T. Matsumoto, T. Nakada, J. Endo, K. Mori, N. Kawamura, *et al.*, "27.1: Invited Paper: High Efficiency Organic EL Devices having Charge Generation Layers," *SID Symposium Digest of Technical Papers*, vol. 34, pp. 964-965, 2003.
- [11] K. Walzer, B. Maennig, M. Pfeiffer, and K. Leo, "Highly Efficient Organic Devices Based on Electrically Doped Transport Layers," *Chemical Reviews*, vol. 107, pp. 1233-1271, 2007/04/01 2007.
- [12] I. Kosan. (2011). Available: <http://www.idemitsu.com/products/electronic/el/performance.html>
- [13] U. Display. (2012). Available: <http://www.oled.com/default.asp?contentID=604>

- [14] M. H. Kim, M. W. Song, S. T. Lee, H. D. Kim, J. S. Oh, and H. K. Chung, "11.3: Control of Emission Zone in a Full Color AMOLED with a Blue Common Layer," *SID Symposium Digest of Technical Papers*, vol. 37, pp. 135-138, 2006.
- [15] M. Hashimoto, S. Igawa, M. Yashima, I. Kawata, M. Hoshino, and M. Osawa, "Highly Efficient Green Organic Light-Emitting Diodes Containing Luminescent Three-Coordinate Copper(I) Complexes," *Journal of the American Chemical Society*, vol. 133, pp. 10348-10351, 2011/07/13 2011.
- [16] C. H. Oh, H. J. Shin, W. J. Nam, B. C. Ahn, S. Y. Cha, and S. D. Yeo, "21.1: Invited Paper: Technological Progress and Commercialization of OLED TV," *SID Symposium Digest of Technical Papers*, vol. 44, pp. 239-242, 2013.
- [17] G. Hong-Yue, Y. Qiu-Xiang, L. Pan, Z. Zhi-Qiang, L. Ji-Cheng, Z. Hua-Dong, *et al.*, "Latest development of display technologies," *Chinese Physics B*, vol. 25, p. 094203, 2016.
- [18] K. Joo-Suc, K. Hyo-Jun, K. Se-Eun, S. Min-Ho, and K. Young-Joo, "P-207L: Late-News Poster: Enhancement of Optical Efficiency in White OLED Display by Applying an Air-Gap Structure on the Patterned Quantum Dot Film," *SID Symposium Digest of Technical Papers*, vol. 47, pp. 1799-1801, 2016.
- [19] S. Scholz, D. Kondakov, B. r. Lüsse, and K. Leo, "Degradation Mechanisms and Reactions in Organic Light-Emitting Devices," *Chemical reviews*, vol. 115, pp. 8449-8503, 2015.
- [20] C. Murawski, K. Leo, and M. C. Gather, "Efficiency Roll-Off in Organic Light-Emitting Diodes," *Advanced Materials*, vol. 25, pp. 6801-6827, 2013.
- [21] S. Möller and S. R. Forrest, "Improved light out-coupling in organic light emitting diodes employing ordered microlens arrays," *Journal of Applied Physics*, vol. 91, pp. 3324-3327, 2002.
- [22] B. W. D'Andrade and J. J. Brown, "Organic light-emitting device luminaire for illumination applications," *Applied Physics Letters*, vol. 88, p. 192908, 2006.
- [23] Y. Sun and S. R. Forrest, "Enhanced light out-coupling of organic light-emitting devices using embedded low-index grids," *Nat Photon*, vol. 2, pp. 483-487, 08/print 2008.
- [24] N. Nakamura, N. Fukumoto, F. Sinapi, N. Wada, Y. Aoki, and K. Maeda, "40.4: Glass Substrates for OLED Lighting with High Out-Coupling Efficiency," *SID Symposium Digest of Technical Papers*, vol. 40, pp. 603-606, 2009.
- [25] S. Reineke, F. Lindner, G. Schwartz, N. Seidler, K. Walzer, B. Lussem, *et al.*, "White organic light-emitting diodes with fluorescent tube efficiency," *Nature*, vol. 459, pp. 234-238, 05/14/print 2009.
- [26] T. Matsumoto, T. Yoshinaga, T. Higo, T. Imai, T. Hirano, and T. Sasaoka, "62.1: High-Performance Solution-Processed OLED Enhanced by Evaporated Common Layer," *SID Symposium Digest of Technical Papers*, vol. 42, pp. 924-927, 2011.
- [27] S. Chen and H.-S. Kwok, "Full color organic electroluminescent display with shared blue light-emitting layer for reducing one fine metal shadow mask," *Organic Electronics*, vol. 13, pp. 31-35, 2012/01/01/ 2012.
- [28] J. Hast, M. Tuomikoski, R. Suhonen, K. L. Väisänen, M. Välimäki, T. Maaninen, *et al.*, "18.1: Invited Paper: Roll-to-Roll Manufacturing of Printed OLEDs," *SID Symposium Digest of Technical Papers*, vol. 44, pp. 192-195, 2013.
- [29] H. Lee, J. Kwak, C.-M. Kang, Y.-Y. Lyu, K. Char, and C. Lee, "Trap-level-engineered common red layer for fabricating red, green, and blue subpixels of full-color organic light-emitting diode displays," *Optics express*, vol. 23, pp. 11424-11435, 2015.

- [30] W.-y. S. Michael S. Weaver, Micahel G. Hack and Julie J. Brown, "New Architectures for OLED displays: how to increase lifetime and resolution," *IMID 2016 DIGEST*, 2016.
- [31] K. Saxena, V. K. Jain, and D. S. Mehta, "A review on the light extraction techniques in organic electroluminescent devices," *Optical Materials*, vol. 32, pp. 221-233, 11// 2009.
- [32] Z. Wang, M. Helander, J. Qiu, D. Puzzo, M. Greiner, Z. Hudson, *et al.*, "Unlocking the full potential of organic light-emitting diodes on flexible plastic," *Nature Photonics*, vol. 5, pp. 753-757, 2011.
- [33] S. Kim, H. W. Cho, K. Hong, J. H. Son, K. Kim, B. Koo, *et al.*, "Design of red, green, blue transparent electrodes for flexible optical devices," *Optics Express*, vol. 22, pp. A1257-A1269, 2014/08/25 2014.
- [34] Y. Jin, J. Feng, X. L. Zhang, Y. G. Bi, Y. Bai, L. Chen, *et al.*, "Solving Efficiency–Stability Tradeoff in Top-Emitting Organic Light-Emitting Devices by Employing Periodically Corrugated Metallic Cathode," *Advanced Materials*, vol. 24, pp. 1187-1191, 2012/03/02 2012.
- [35] M. Thomschke, R. Nitsche, M. Furno, and K. Leo, "Optimized efficiency and angular emission characteristics of white top-emitting organic electroluminescent diodes," *Applied Physics Letters*, vol. 94, p. 083303, 2009.
- [36] M. Hwang, C. Kim, H. Choi, H. Chae, and S. M. Cho, "Light extraction from surface plasmon polaritons and substrate/waveguide modes in organic light-emitting devices with silver-nanomesh electrodes," *Optics Express*, vol. 24, pp. 29483-29495, 2016/12/26 2016.
- [37] L.-H. Xu, Q.-D. Ou, Y.-Q. Li, Y.-B. Zhang, X.-D. Zhao, H.-Y. Xiang, *et al.*, "Microcavity-Free Broadband Light Outcoupling Enhancement in Flexible Organic Light-Emitting Diodes with Nanostructured Transparent Metal–Dielectric Composite Electrodes," *ACS Nano*, vol. 10, pp. 1625-1632, 2016/01/26 2016.
- [38] M. Jung, D. M. Yoon, M. Kim, C. Kim, T. Lee, J. H. Kim, *et al.*, "Enhancement of hole injection and electroluminescence by ordered Ag nanodot array on indium tin oxide anode in organic light emitting diode," *Applied Physics Letters*, vol. 105, p. 013306, 2014.
- [39] X. Gu, T. Qiu, W. Zhang, and P. K. Chu, "Light-emitting diodes enhanced by localized surface plasmon resonance," *Nanoscale Research Letters*, vol. 6, p. 199, March 08 2011.
- [40] W.-Y. Park, Y. Kwon, H.-W. Cheong, C. Lee, and K.-W. Whang, "Increased light extraction efficiency from top-emitting organic light-emitting diodes employing a mask-free plasma-etched stochastic polymer surface," *Journal of Applied Physics*, vol. 119, p. 095502, 2016.
- [41] W.-Y. Park, Y. Kwon, C. Lee, and K.-W. Whang, "Light outcoupling enhancement from top-emitting organic light-emitting diodes made on a nano-sized stochastic texture surface," *Optics Express*, vol. 22, pp. A1687-A1694, 2014/12/15 2014.
- [42] W. Gaynor, S. Hofmann, M. G. Christoforo, C. Sachse, S. Mehra, A. Salleo, *et al.*, "Color in the Corners: ITO-Free White OLEDs with Angular Color Stability," *Advanced Materials*, vol. 25, pp. 4006-4013, 2013.
- [43] K. Hong and J.-L. Lee, "Review paper: Recent developments in light extraction technologies of organic light emitting diodes," *Electronic Materials Letters*, vol. 7, pp. 77-91, 2011.
- [44] T.-W. Koh, J.-M. Choi, S. Lee, and S. Yoo, "Optical Outcoupling Enhancement in Organic Light-Emitting Diodes: Highly Conductive Polymer as a Low-Index Layer on Microstructured ITO Electrodes," *Advanced Materials*, vol. 22, pp. 1849-1853, 2010.

- [45] K. Lee, J.-W. Shin, J.-H. Park, J. Lee, C. W. Joo, J.-I. Lee, *et al.*, "A Light Scattering Layer for Internal Light Extraction of Organic Light-Emitting Diodes Based on Silver Nanowires," *ACS Applied Materials & Interfaces*, vol. 8, pp. 17409-17415, 2016/07/13 2016.
- [46] X.-D. Zhao, Y.-Q. Li, H.-Y. Xiang, Y.-B. Zhang, J.-D. Chen, L.-H. Xu, *et al.*, "Efficient Color-Stable Inverted White Organic Light-Emitting Diodes with Outcoupling-Enhanced ZnO Layer," *ACS Applied Materials & Interfaces*, vol. 9, pp. 2767-2775, 2017/01/25 2017.
- [47] C. W. Joo, J.-W. Shin, J. Moon, J. W. Huh, D.-H. Cho, J. Lee, *et al.*, "Highly efficient white transparent organic light emitting diodes with nano-structured substrate," *Organic Electronics*, vol. 29, pp. 72-78, 2// 2016.
- [48] K. Meerholz and D. C. Müller, "Outsmarting Waveguide Losses in Thin-Film Light-Emitting Diodes," *Advanced Functional Materials*, vol. 11, pp. 251-253, 2001.
- [49] Y.-J. Lee, S.-H. Kim, J. Huh, G.-H. Kim, Y.-H. Lee, S.-H. Cho, *et al.*, "A high-extraction-efficiency nanopatterned organic light-emitting diode," *Applied Physics Letters*, vol. 82, pp. 3779-3781, 2003.
- [50] X.-B. Shi, M. Qian, D.-Y. Zhou, Z.-K. Wang, and L.-S. Liao, "Origin of light manipulation in nano-honeycomb structured organic light-emitting diodes," *Journal of Materials Chemistry C*, vol. 3, pp. 1666-1671, 2015.
- [51] Y. Qu, M. Sloatsky, and S. R. Forrest, "Enhanced light extraction from organic light-emitting devices using a sub-anode grid," *Nature Photonics*, 2015.
- [52] T. Qiu, F. Kong, X. Yu, W. Zhang, X. Lang, and P. K. Chu, "Tailoring light emission properties of organic emitter by coupling to resonance-tuned silver nanoantenna arrays," *Applied Physics Letters*, vol. 95, p. 213104, 2009.
- [53] M. Battulga, P. Hannes, D. Patrick, K. T. Arno, S. M. Clark, and H. Calin, "Performance Boost of Organic Light-Emitting Diodes with Plasmonic Nanostars," *Advanced Optical Materials*, vol. 4, pp. 772-781, 2016.
- [54] C. Cho, H. Kang, S.-W. Baek, T. Kim, C. Lee, B. J. Kim, *et al.*, "Improved Internal Quantum Efficiency and Light-Extraction Efficiency of Organic Light-Emitting Diodes via Synergistic Doping with Au and Ag Nanoparticles," *ACS Applied Materials & Interfaces*, vol. 8, pp. 27911-27919, 2016/10/19 2016.
- [55] S.-J. Ko, H. Choi, W. Lee, T. Kim, B. R. Lee, J.-W. Jung, *et al.*, "Highly efficient plasmonic organic optoelectronic devices based on a conducting polymer electrode incorporated with silver nanoparticles," *Energy & Environmental Science*, vol. 6, pp. 1949-1955, 2013.
- [56] H. Choi, S.-J. Ko, Y. Choi, P. Joo, T. Kim, B. R. Lee, *et al.*, "Versatile surface plasmon resonance of carbon-dot-supported silver nanoparticles in polymer optoelectronic devices," *Nature Photonics*, vol. 7, p. 732, 07/21/online 2013.
- [57] H. Cho, C. Yun, and S. Yoo, "Multilayer transparent electrode for organic light-emitting diodes: tuning its optical characteristics," *Optics express*, vol. 18, pp. 3404-3414, 2010.
- [58] L. Xiao, Z. Chen, B. Qu, J. Luo, S. Kong, Q. Gong, *et al.*, "Recent Progresses on Materials for Electrophosphorescent Organic Light-Emitting Devices," *Advanced Materials*, vol. 23, pp. 926-952, 2011.
- [59] H. Matsushima, S. Naka, H. Okada, and H. Onnagawa, "Organic electrophosphorescent devices with mixed hole transport material as emission layer," *Current Applied Physics*, vol. 5, pp. 305-308, 2005/05/01/ 2005.
- [60] P. M. Borsenberger, L. Pautmeier, R. Richert, and H. Bässler, "Hole transport in 1,1-bis(di-4-tolylaminophenyl)cyclohexane," *The Journal of Chemical Physics*, vol. 94, pp. 8276-8281, 1991.

- [61] S. J. Su, T. Chiba, T. Takeda, and J. Kido, "Pyridine-Containing Triphenylbenzene Derivatives with High Electron Mobility for Highly Efficient Phosphorescent OLEDs," *Advanced Materials*, vol. 20, pp. 2125-2130, 2008.
- [62] Y. H. Son, Y. J. Kim, M. J. Park, H.-Y. Oh, J. S. Park, J. H. Yang, *et al.*, "Small single-triplet energy gap bipolar host materials for phosphorescent blue and white organic light emitting diodes," *Journal of Materials Chemistry C*, vol. 1, pp. 5008-5014, 2013.
- [63] Z. Xiao-Wen, X. Ji-Wen, X. Hua-Rui, W. Hua, X. Chun-Lin, W. Bin, *et al.*, "Elucidation of carrier injection and recombination characteristics with impedance and capacitance in organic light-emitting diodes and the frequency effects," *Journal of Physics D: Applied Physics*, vol. 46, p. 055102, 2013.
- [64] X. Zhang, B. Mo, F. You, L. Liu, H. Wang, and B. Wei, "Highly-efficient low-voltage organic light-emitting diode by controlling hole transporting with doped dual hole-transport layer and the impedance spectroscopy analysis," *Synthetic Metals*, vol. 205, pp. 134-138, 2015/07/01/ 2015.
- [65] B. Mo, X. Zhang, L. Liu, H. Wang, J. Xu, H. Wang, *et al.*, "Bilayer-structure white organic light-emitting diode based on [Alq3:rubrene] and the electron transporting characteristics investigation using impedance spectroscopy," *Optics & Laser Technology*, vol. 68, pp. 202-205, 2015/05/01/ 2015.
- [66] P. N. Murgatroyd, "Theory of space-charge-limited current enhanced by Frenkel effect," *Journal of Physics D: Applied Physics*, vol. 3, p. 151, 1970.
- [67] P. W. M. Blom, M. J. M. de Jong, and M. G. van Munster, "Electric-field and temperature dependence of the hole mobility in poly(p-phenylene vinylene)," *Physical Review B*, vol. 55, pp. R656-R659, 01/01/ 1997.
- [68] P. Mark and W. Helfrich, "Space-Charge-Limited Currents in Organic Crystals," *Journal of Applied Physics*, vol. 33, pp. 205-215, 1962.
- [69] A. Rose, "Space-Charge-Limited Currents in Solids," *Physical Review*, vol. 97, pp. 1538-1544, 03/15/ 1955.
- [70] H. A. Atwater and A. Polman, "Plasmonics for improved photovoltaic devices," *Nature Materials*, vol. 9, p. 205, 02/19/online 2010.
- [71] M. Gustav, "Beiträge zur Optik trüber Medien, speziell kolloidaler Metallösungen," *Annalen der Physik*, vol. 330, pp. 377-445, 1908.
- [72] D. Duche, P. Torchio, L. Escoubas, F. Monestier, J.-J. Simon, F. Flory, *et al.*, "Improving light absorption in organic solar cells by plasmonic contribution," *Solar Energy Materials and Solar Cells*, vol. 93, pp. 1377-1382, 2009/08/01/ 2009.
- [73] G. M. Farinola and R. Ragni, "Electroluminescent materials for white organic light emitting diodes," *Chemical Society Reviews*, vol. 40, pp. 3467-3482, 2011.
- [74] C. W. Han, K. M. Kim, S. J. Bae, H. S. Choi, J. M. Lee, T. S. Kim, *et al.*, "21.2: 55-inch FHD OLED TV employing New Tandem WOLEDs," *SID Symposium Digest of Technical Papers*, vol. 43, pp. 279-281, 2012.
- [75] M. A. Baldo, C. Adachi, and S. R. Forrest, "Transient analysis of organic electrophosphorescence. II. Transient analysis of triplet-triplet annihilation," *Physical Review B*, vol. 62, pp. 10967-10977, 10/15/ 2000.
- [76] S. Reineke, K. Walzer, and K. Leo, "Triplet-exciton quenching in organic phosphorescent light-emitting diodes with Ir-based emitters," *Physical Review B*, vol. 75, p. 125328, 03/28/ 2007.
- [77] W. Song and J. Y. Lee, "Light emission mechanism of mixed host organic light-emitting diodes," *Applied Physics Letters*, vol. 106, p. 123306, 2015.
- [78] H. H. Fong, K. C. Lun, and S. K. So, "Hole transports in molecularly doped triphenylamine derivative," *Chemical Physics Letters*, vol. 353, pp. 407-413, 2002/02/26/ 2002.

- [79] F. Nüesch, D. Berner, E. Tutiš, M. Schaer, C. Ma, X. Wang, *et al.*, "Doping-Induced Charge Trapping in Organic Light-Emitting Devices," *Advanced Functional Materials*, vol. 15, pp. 323-330, 2005.
- [80] Y. Lv, P. Zhou, N. Wei, K. Peng, J. Yu, B. Wei, *et al.*, "Improved hole-transporting properties of Ir complex-doped organic layer for high-efficiency organic light-emitting diodes," *Organic Electronics*, vol. 14, pp. 124-130, 2013/01/01/ 2013.
- [81] J. Huang, Z. Xu, and Y. Yang, "Low-Work-Function Surface Formed by Solution-Processed and Thermally Deposited Nanoscale Layers of Cesium Carbonate," *Advanced Functional Materials*, vol. 17, pp. 1966-1973, 2007.
- [82] R. Mac Ciarnain, D. Michaelis, T. Wehler, A. F. Rausch, S. Wehrmeister, T. D. Schmidt, *et al.*, "Plasmonic Purcell effect reveals obliquely ordered phosphorescent emitters in Organic LEDs," *Scientific Reports*, vol. 7, p. 1826, 2017/05/12 2017.
- [83] H. Uoyama, K. Goushi, K. Shizu, H. Nomura, and C. Adachi, "Highly efficient organic light-emitting diodes from delayed fluorescence," *Nature*, vol. 492, p. 234, 12/12/online 2012.
- [84] M. Kühn, C. Pflumm, T. Glaser, P. Harbach, W. Jaegermann, and E. Mankel, "Band alignment in organic light emitting diodes - On the track of thickness dependent onset voltage shifts," *Organic Electronics*, vol. 41, pp. 79-90, 2017/02/01/ 2017.
- [85] M. Chang-Ki, S. Katsuki, S. Katsuyuki, A. Chihaya, K. Hironori, and K. Jang-Joo, "Combined Inter- and Intramolecular Charge-Transfer Processes for Highly Efficient Fluorescent Organic Light-Emitting Diodes with Reduced Triplet Exciton Quenching," *Advanced Materials*, vol. 29, p. 1606448, 2017.
- [86] M. Furno, R. Meerheim, S. Hofmann, B. Lüssem, and K. Leo, "Efficiency and rate of spontaneous emission in organic electroluminescent devices," *Physical Review B*, vol. 85, p. 115205, 03/21/ 2012.
- [87] J.-S. Kim, P. K. H. Ho, N. C. Greenham, and R. H. Friend, "Electroluminescence emission pattern of organic light-emitting diodes: Implications for device efficiency calculations," *Journal of Applied Physics*, vol. 88, pp. 1073-1081, 2000.
- [88] R. Meerheim, M. Furno, S. Hofmann, B. Lüssem, and K. Leo, "Quantification of energy loss mechanisms in organic light-emitting diodes," *Applied Physics Letters*, vol. 97, p. 253305, 2010.
- [89] G. Gu, D. Z. Garbuzov, P. E. Burrows, S. Venkatesh, S. R. Forrest, and M. E. Thompson, "High-external-quantum-efficiency organic light-emitting devices," *Optics Letters*, vol. 22, pp. 396-398, 1997/03/15 1997.
- [90] M. C. Gather and S. Reineke, "Recent advances in light outcoupling from white organic light-emitting diodes," 2015, p. 20.
- [91] Z. B. Wang, M. G. Helander, J. Qiu, D. P. Puzzo, M. T. Greiner, Z. M. Hudson, *et al.*, "Unlocking the full potential of organic light-emitting diodes on flexible plastic," *Nature Photonics*, vol. 5, p. 753, 10/30/online 2011.
- [92] S. Kim and J.-L. Lee, "Design of dielectric/metal/dielectric transparent electrodes for flexible electronics," 2012, p. 22.
- [93] A. Dodabalapur, L. J. Rothberg, R. H. Jordan, T. M. Miller, R. E. Slusher, and J. M. Phillips, "Physics and applications of organic microcavity light emitting diodes," *Journal of Applied Physics*, vol. 80, pp. 6954-6964, 1996.
- [94] S. H. Lee, K. Y. Shin, J. Y. Hwang, K. T. Kang, and H. S. Kang, "Silver inkjet printing with control of surface energy and substrate temperature," *Journal of Micromechanics and Microengineering*, vol. 18, p. 075014, 2008.
- [95] B. Medasani, Y. H. Park, and I. Vasiliev, "Theoretical study of the surface energy, stress, and lattice contraction of silver nanoparticles," *Physical Review B*, vol. 75, p. 235436, 06/22/ 2007.

- [96] F. Liu and J.-M. Nunzi, "Phosphorescent organic light emitting diode efficiency enhancement using functionalized silver nanoparticles," *Applied Physics Letters*, vol. 99, p. 123302, 2011.
- [97] H. Zhang, S. Chen, and D. Zhao, "Surface-plasmon-enhanced microcavity organic light-emitting diodes," *Optics Express*, vol. 22, pp. A1776-A1782, 2014/12/15 2014.
- [98] T. Fleetham, J.-Y. Choi, H. W. Choi, T. Alford, D. S. Jeong, T. S. Lee, *et al.*, "Photocurrent enhancements of organic solar cells by altering dewetting of plasmonic Ag nanoparticles," *Scientific Reports*, vol. 5, p. 14250, 09/21/online 2015.
- [99] W. C. Y. Ma, S. W. Yuan, T. C. Chan, and C. Y. Huang, "Threshold Voltage Reduction and Mobility Improvement of LTPS-TFTs With NH_3 Plasma Treatment," *IEEE Transactions on Plasma Science*, vol. 42, pp. 3722-3725, 2014.
- [100] C. P. Chang and Y. S. Wu, "Improved Electrical Performance and Uniformity of MILC Poly-Si TFTs Manufactured Using Drive-In Nickel-Induced Lateral Crystallization," *IEEE Electron Device Letters*, vol. 30, pp. 1176-1178, 2009.
- [101] J. T. Guske, J. Brown, A. Welsh, and S. Franzen, "Infrared surface plasmon resonance of AZO-Ag-AZO sandwich thin films," *Optics Express*, vol. 20, pp. 23215-23226, 2012/10/08 2012.
- [102] J. Gong, R. Dai, Z. Wang, and Z. Zhang, "Thickness Dispersion of Surface Plasmon of Ag Nano-thin Films: Determination by Ellipsometry Iterated with Transmittance Method," *Scientific Reports*, vol. 5, p. 9279, 03/23/online 2015.
- [103] K. Y. Yang, K. C. Choi, and C. W. Ahn, "Surface plasmon-enhanced spontaneous emission rate in an organic light-emitting device structure: Cathode structure for plasmonic application," *Applied Physics Letters*, vol. 94, p. 173301, 2009.
- [104] M. Hu, C. Novo, A. Funston, H. Wang, H. Staleva, S. Zou, *et al.*, "Dark-field microscopy studies of single metal nanoparticles: understanding the factors that influence the linewidth of the localized surface plasmon resonance," *Journal of Materials Chemistry*, vol. 18, pp. 1949-1960, 2008.
- [105] E. D. G. Palik, Gorachand, "Handbook of optical constants of solids," *Academic Press*, 1985.
- [106] H. S. Kim, C. W. Joo, B. Pyo, J. Lee, and M. C. Suh, "Improvement of viewing angle dependence of the white organic light emitting diodes with tandem structure by introduction of nanoporous polymer films," *Organic Electronics*, vol. 40, pp. 88-96, 2017/01/01/ 2017.
- [107] M. C. Suh, B. Pyo, and H. S. Kim, "Suppression of the viewing angle dependence by introduction of nanoporous diffuser film on blue OLEDs with strong microcavity effect," *Organic Electronics*, vol. 28, pp. 31-38, 2016/01/01/ 2016.
- [108] M. Sliotsky and S. R. Forrest, "Full-wave simulation of enhanced outcoupling of organic light-emitting devices with an embedded low-index grid," *Applied Physics Letters*, vol. 94, p. 163302, 2009.

Publication

[1] SCI Journal Papers

1. Gyujeong Lee, In-Ho Lee, Hea-Lim Park, Sin-Hyung Lee, **Jongseok Han**, Changhee Lee, and Sin-Doo Lee, “Vertical Organic Light-Emitting Transistor Showing a High Current On/Off Ratio through Dielectric Encapsulation for the Effective Charge Pathway”, *Journal of Applied Physics* **121**, 024502 (2017).
2. Chi Hyun Ryoo, Illhun Cho, **Jongseok Han**, Jung-hoon Yang, Ji Eon Kwon, Sehun Kim, Hyein Jeong, Changhee Lee, and Soo Young Park, “Structure-Property Correlation in Luminescent Indolo[3,2-b]indole (IDID) Derivatives: Unraveling the Mechanism of High Efficiency Thermally Activated Delayed Fluorescence (TADF)”, *ACS Applied Materials & Interfaces* **9**, 41413 (2017).
3. Hyung-Jung Song*, **Jongseok Han***, Gunhee Lee, Jiho Sohn, Yongwon Kwon, Masso Choi, and Changhee Lee, “Enhanced light out-coupling in OLED employing thermal-assisted, self-aggregated silver nano particles”, *Organic Electronics* **52**, 230 (2018) (*:co-first).
4. Yeonkung Lee, Byeong Guk Jeong, Heebum Roh, Jeongkyun Roh, **Jongseok Han**, Doh Chang Lee, Wan Ki Bae, Jae-Yup Kim, and Changhee Lee,

“Enhanced lifetime and efficiency of red quantum dot light-emitting diodes with Y-doped ZnO sol-gel electron-transport layers by reducing excess electron injection”, *Advanced Quantum Technologies* (2018)
DOI: 10.1002/qute.201700006.

[2] SCIE Journal Papers

1. **Jongseok Han**, Donghyun Ko, Myeongjin Park, Jeongkyun Roh, Heeyoung Jung, Yeonkyung Lee, Yongwon Kwon, Jiho Sohn, Wan Ki Bae, Byung Doo Chin, and Changhee Lee, “Toward high-resolution, inkjet-printed, quantum dot light-emitting diodes for next-generation displays”, *Journal of the Society for Information Display* **24**, 545 (2016) **Front Cover Paper**.

[3] International Conferences

1. **Jongseok Han**, Yongwon Kwon, and Changhee Lee, “Tandem White Organic Light-Emitting Diode Using Enhanced Charge Generation Layer with Liq Dipole Layer”, *The 14th International Meeting on Information Display*, August 2014.
2. **Jongseok Han**, Yongwon Kwon, and Changhee Lee, “The Study on Enhanced Charge Generation Unit for Low Driving Voltage and High Efficiency”, *2014 Materials Research Society Fall Meeting & Exhibit*, Dec 2014.
3. **Jongseok Han**, Yongwon Kwon, Jiho Sohn, and Changhee Lee, “Highly Enhanced Green Phosphorescent Organic Light-Emitting Diodes with Cesium Fluoride Doped Electron Injection Layer”, *The International Society for Optics and Photonics (SPIE Optics + Photonics)*, August 2015.

4. **Jongseok Han**, Hyung-Jun Song, Yongwon Kwon, Jiho Sohn, and Changhee Lee, “Highly Efficient Organic Light-Emitting Diodes with Transparent Electrode Adopting Low Refractive Index Material”, *The 15th International Meeting on Information Display*, August 2015.
5. **Jongseok Han**, Donghyun Ko, Myeongjin Park, Jeongkyun Roh, Heeyoung Jung, Yeonkyung Lee, Yongwon Kwon, Jiho Sohn, Wan Ki Bae, Byung Doo Chin, and Changhee Lee, “Toward high-resolution, inkjet-printed, quantum dot light-emitting diodes for next-generation displays”, *The 54th SID International Symposium, Seminar & Exhibition, Front Cover of JSID*, Jun 2016.
6. **Jongseok Han**, Hyung-Jun Song, Yongwon Kwon, Jiho Sohn, and Changhee Lee, “Low-Cost and Simple Fabrication of Thermally Aggregated Silver Nanoparticles for Light Extraction in Organic Light-Emitting Diodes”, *The 16th International Meeting on Information Display*, August 2016.
7. **Jongseok Han**, Donghyun Ko, Yeosul Park, and Changhee Lee, “Inkjet-Printed Quantum Dots Light-Emitting Diodes Employing Various Ink Systems for High Resolution Display”, *The 10th International Symposium on Flexible Organic Electronics (ISFOE)*, Jul 2017.
8. **Jongseok Han**, and Changhee Lee, “Advanced Pixel Architecture for OLED displays with Yellow Common Layer”, *The 17th International Meeting on Information Display*, August 2017.
9. Yeonkyung Lee, Beong Guk Jeong, Heebum Roh, Jeongkyun Roh, **Jongseok Han**, Doh Chang Lee, Wan Ki Bae, Jae-Yup Kim, and Changhee Lee, “Enhanced Device Performance by Improving Charge Balance with Y-Doped ZnO in Quantum Dot Light-Emitting Diodes”, *The 10th International Conference on Quantum Dots*

10. **Jongseok Han**, Wan Ki Bae, and Changhee Lee, “Improving Charge Balance Using LiF Thin Layer: Toward Highly Efficient and Stable Inverted Quantum-Dot Light-Emitting Diodes”, *The 18th International Meeting on Information Display*, August 2018.

한글 초록

유기발광다이오드는 디스플레이와 조명 산업의 발달을 가능케하면서 수 십년간 많은 발전을 이룩해왔다. 하지만 유기발광다이오드 디스플레이 시장의 확장을 위해서는 유기발광다이오드의 가격을 낮출 수 있는 공정을 개발하거나 유기발광다이오드의 성능을 높일 수 있는 연구가 선행되어야 한다. 이러한 문제점을 해결하기 위해 다양한 유기발광다이오드의 픽셀과 소자 구조에 대한 연구가 진행되어 왔다. 예를 들어, 펜타일 픽셀 구조와 백색 유기발광다이오드와 칼라필터를 사용한 구조 등을 통한 저가 공정 구현이 되어 왔고, 또한 전면발광 구조와 나노구조물 삽입등의 소자 구조 변화를 통해 유기발광다이오드의 성능을 향상시켜왔다. 하지만 유기발광다이오드 패널은 여전히 높은 가격과 낮은 성능으로 인해 시장 확장에 어려움을 겪고 있다.

따라서 본 논문에서는 유기발광다이오드 공정 가격을 줄일 수 있는 새로운 픽셀 설계와 유기발광다이오드 성능을 높일 수 있는 새로운 소자 구조 설계를 제안하고자 한다. 황색공통층을 통하여 발광층을 단일 패터닝을 통해 풀컬러 유기발광다이오드를 구현하였고, 또한 열활성-자기응집 방법을 통해 은 나노 입자를 삽입하여 광추출 효율을 향상시키는 연구를 진행하였다.

첫째로, 풀컬러 유기발광다이오드를 위한 단순하면서 효과적인 픽셀 구조를 연구하였다. 발광층의 단일 패터닝을 위해 황색공통층을 이용하였고, 이를 통해 황색 패터닝 과정을 생략할 수 있게 하였다.

황색공통층을 사용하였을 경우 황색 도펀트가 정공의 트랩으로 작용할 수 있기 때문에, 트랩의 깊이와 농도를 조절하여 소자 성능에 영향을 주지 않도록 조절하는 것이 중요하다. 따라서 여러가지 정공수송층을 호스트 물질로 적용하여, 기존 유기발광다이오드 대비 황색공통층을 적용한 유기발광다이오드의 성능에 영향을 미치는 요인을 연구하였다. 결과적으로, 기존 유기발광다이오드의 장수명, 고해상도등의 이점을 그대로 이용하면서, 저가 공정을 이룰 수 있는 단일 패터닝 풀컬러 유기발광다이오드를 설계할 수 있었다.

두번째로, 열활성-자기응집 은 나노 입자를 이용하여 광추출 효율을 향상시킬 수 있는 산업에서 즉시 제작가능한 방법을 제시하였다. 기존의 복잡한 과정과 높은 가격을 통한 나노 입자의 제작이 아닌, 단순 진공증착과 열처리 과정을 통해 대면적에 제작가능한 은 나노 입자 형성 기술을 개발하였다. 시뮬레이션과 암시야 현미경을 통해 광산란 효과를 확인할 수 있었다. 결과적으로, 은 나노 입자를 이용하여, 외부광자효율을 11% 향상시킬 수 있었으며, 각도에 따른 스펙트럼 변화를 완화시킬 수 있었다.

본 논문에서는 유기발광다이오드의 높은 가격을 낮추기 위하여 제작 공정을 단순화하는 픽셀 구조에 대한 연구를 시도하였다. 추가적으로 고성능 유기발광다이오드를 위한 은 나노 입자 삽입을 통하여 광추출 효율을 향상시킬 수 있는 소자 구조를 제안하였다. 본 논문에서 연구된 유기발광다이오드의 황색공통층을 이용한 픽셀 구조에 대한 제시와 광추출 향상을 위한 소자 구조의 제시는 산업에 즉시 활용될 수 있으며, 패널 제작 가격을 낮추고 높아진 성능을 통해 유기발광다이오드 시장의 확대를 가져올 수 있는 플랫폼으로서 활용되길 기대해본다.

주요어: 유기발광다이오드, 황색공통층, 발광층 패터닝, 열활성-자기응집 은
나노입자, 광추출 효율

학번: 2013-20905

감사의 글

2013 년 첫 대학원 입학 후 어느덧 2018 년 박사과정 졸업을 앞두고 있습니다. 이렇게 무사히 박사 학위를 받을 수 있었던 점과 지금의 제가 있기까지는 정말 많은 분들의 도움이 있었기 때문이라고 생각합니다. 이 자리를 빌어 감사의 글을 올리하고자 합니다.

우선 부족한 저를 아낌없이 지도해주신 이창희 교수님께 진심으로 감사드립니다. 교수님의 올바른 충고와 조언으로 정말 많은 것을 배우고 깨달아 크게 성장할 수 있었습니다. 앞으로도 교수님께 부끄럽지 않은 제자가 되기 위해 계속해서 노력하겠습니다. 그리고 부족했던 제 박사학위논문을 지도해주신 이신두 교수님, 홍용택 교수님, 강경태 박사님, 형준이 형님께 감사 드립니다. 교수님들과 박사님들의 가르침 명심하고 앞으로 사회에 나가서도 더욱 발전할 수 있도록 하겠으며, 제가 받았던 도움을 잊지않고 베풀 수 있는 사람이 되도록 노력하겠습니다.

5 년반이라는 시간 동안 연구실에서 제게 많은 도움을 준 선후배들에게도 감사 드립니다. 힘든일, 기쁜일을 함께 겪으면서 보낸 20 대의 절반을 절대 잊지 못할 것 같습니다. 먼저, 연구실 생활도 재밌게 이끌어주셨고, 제가 무사히 박사 졸업 할 수 있게 정말 큰 도움을 주신 형준이 형님께 다시 한번 감사의 말씀 드립니다. 그리고 아무것도 모르던 저를 이것저것 많이 가르쳐주셨던 명진이형, 정균이형, 희영이형, 용원이형 감사드립니다. 그리고 같은 시기에 들어와 함께 연구실 생활을 하면서 의지가 됐던 지호형, 현호, 재훈이 고맙습니다. 같이 영어 공부를 하며 친해졌던 승현이, 건식이, 부족한 팀장 만나 밤늦게까지 잉크젯하느라 함께 고생한 희범이형, 동현이, 예술이 모두에게 감사

드립니다. 축구로 더 친해진 근우, 앞으로 연구실 핵심이 될 캐보 재열이, 경환이, 태수, 광모 그리고 석사 졸업 후 더 기대되는 지원이까지... 모두에게 남은 기간 무사히 잘 끝마치길 바라며 언제나 도움이 필요하면 연락하길 바랍니다. 부족한 저를 이끌어주고 힘든 일에도 웃으며 잘 따라와줘서 정말 고맙습니다.

학위 기간 동안 가장 많은 도움을 주었고, 앞으로는 인생의 동반자로 언제나 함께할 연경. 이제는 같은 연구실을 떠나 다른 곳에서 일하게 됐지만 항상 곁을 지켜주고 힘이 되어 주어서 고맙고 사랑해. 앞으로도 끝까지 함께 행복하자.

마지막으로 아버지, 어머니 늘 뒤에서 묵묵히 지켜봐주시고 끝없는 믿음으로 응원해주셔서 지금의 제가 있습니다. 받은 만큼 드릴 수는 없겠지만 모든 맘 다해 효도하겠습니다. 앞으로도 자랑스러운 아들이 되도록 노력하겠습니다. 항상 응원해준 종민이까지 우리 가족 정말 감사하고 사랑합니다.

박사학위를 끝이라 생각하지 않고 학위과정동안 부족했던 연구를 계속하여 세상을 변화시킬 수 있는 연구자가 되도록 하겠습니다. 도와주신 모든 분들께 감사의 말씀 드립니다.

2018년 8월

한중석